
Electronic Thesis and Dissertation Repository

10-11-2019 10:00 AM

Validation of rhoCentralFoam for Engineering Applications of Under-Expanded Impinging Free Jets

Peter Nielsen
The University of Western Ontario

Supervisor
DeGroot, Chris.
The University of Western Ontario Co-Supervisor
Straatman, Anthony.
The University of Western Ontario

Graduate Program in Mechanical and Materials Engineering
A thesis submitted in partial fulfillment of the requirements for the degree in Master of Engineering Science
© Peter Nielsen 2019

Follow this and additional works at: <https://ir.lib.uwo.ca/etd>



Part of the [Heat Transfer, Combustion Commons](#), and the [Propulsion and Power Commons](#)

Recommended Citation

Nielsen, Peter, "Validation of rhoCentralFoam for Engineering Applications of Under-Expanded Impinging Free Jets" (2019). *Electronic Thesis and Dissertation Repository*. 6789.
<https://ir.lib.uwo.ca/etd/6789>

This Dissertation/Thesis is brought to you for free and open access by Scholarship@Western. It has been accepted for inclusion in Electronic Thesis and Dissertation Repository by an authorized administrator of Scholarship@Western. For more information, please contact wlsadmin@uwo.ca.

Abstract

A numerical validation study of under-expanded impinging jet is conducted using OpenFOAM, an open-source computational fluid dynamics (CFD) library. RhoCentralFoam, a density based, compressible flow solver with a two-equation $k - \omega$ shear stress transport (SST) turbulence model is used on an axisymmetric model to reduce the computation cost. Major features of the flow were compared to an experimental study by Henderson et al., with a nozzle pressure ratio (NPR) of 4.0 and nozzle to plate spacing between 1.65-4.16. Of the features measured, the Mach diamond spacing, super-sonic core, and shear layer are all accurately predicted, while the recirculation bubble in the impingement region and acoustic phenomenon are suppressed. The model is then applied pneumatic nebulizer medical device, which generates a low-pressure vortex by confining the impingement region. Several geometric features are varied to determine their influence on the rotating vortex, of which the nozzle to plate spacing was most influential.

Keywords

Compressible, Under-Expanded Jet Impingement, OpenFOAM, Parametric Study

Summary for Lay Audience

Many engineering problems require an understanding of how their project interacts with air, water, or any other fluid involved. In recent decades, new computer techniques have been developed that enable the behaviour of fluids to be better predicted, providing valuable insight into many problems. This work will check the accuracy of a computer simulation software called OpenFOAM, as it models a super-sonic jet of air impacting a wall. The settings in the program were selected to be compatible with super-sonic flows, with separate settings to check the impact of turbulence on the flow. To make the simulation faster, only a small slice of the flow region was simulated, reducing the number of calculations required by the computer. The results of the computer simulation were compared to a well-documented experiment to ensure they were correct. Many aspects of the computer simulation match the experimental results well, although there were some errors found where the flow impacted the wall. Some parts of the jet will move around as time passes, these features of the jet were also suppressed in the computer simulation. Once the accuracy of the computer simulation was known, it was applied to a medical device that operates under similar conditions, to predict the flow for that specific application. In that device, after the air flow hit the wall it would begin to rotate rapidly in a vortex, creating a suction between the vortex and the jet flow. The amount of suction in the device was experimentally measured and compared to the computer simulations, finding good agreement between the two results. Finally, the impact that changing some of the dimensions in the device had on the suction pressure was explored. The most important geometric feature was the distance between the start of the jet flow, and the wall it impacted on.

Acknowledgments

I would like to thank my supervisors, Dr. Anthony Straatman and Dr. Chris DeGroot, for their support and guidance through this process, and their encouragement for me to learn outside the scope of my research.

I would like to thank the members of my lab for their many hours helping me problem solve the issues I had. I would not have achieved the work I did without your help.

I would like to thank NSERC for funding my research, and my industry partner for both funding and guiding my project.

Nomenclature

T	Temperature	[K]
T_0	Stagnation temperature	[K]
U	Fluid velocity	[m/s]
C_p	Heat capacity at constant pressure	[$J \cdot kg/K$]
C_v	Heat capacity at constant volume	[$J kg/K$]
R	Universal gas constant (8.314)	[$J/mol K$]
M	Molar mass	[kg/mol]
γ	Ratio of specific heats	–
h	Enthalpy	[kJ/kg]
h_0	Stagnation Enthalpy	[kJ/kg]
P	Pressure	[Pa]
P_0	Stagnation Pressure	[Pa]
Ma	Mach number	–
M_y	Mach number downstream of a normal shock	–
M_x	Mach number upstream of a normal shock	–
P_{0y}	Stagnation pressure downstream of a normal shock	[Pa]
P_{0x}	Stagnation pressure upstream of a normal shock	[Pa]

P_{atm}	Atmospheric Pressure	[Pa]
η_0	Ratio of pressure in supply reservoir to ambient pressure	—
Δ_1	Length of the first Mach diamond	[m]
Δ_s	Length of subsequent Mach diamonds	[m]
d	Diameter of a nozzle exit	[m]
η_e	Ratio of pressure at nozzle exit to ambient pressure	—
Re_j	Jet Reynolds number	—
L_c	Length of the supersonic core	[m]
ρ	Density	[kg/m ³]
t	Time	[s]
E	Total energy density	[kJ/kg]
ψ	One (1) divided by the product of the universal gas constant (R) and Temperature (T)	[1/J · kg]
μ_t	Turbulent viscosity	[N s/m ²]
α_t	Turbulent diffusion	[m ² /s]
I	Turbulent Intensity	—
U_{ref}	Inlet boundary reference velocity	[m/s]
k	Turbulent kinetic energy	[J/kg]
ω	Specific dissipation rate	[1/s]

T_p	Temperature at an inlet boundary	[K]
P_p	Pressure at an inlet boundary	[Pa]
L	Length from nozzle exit to impingement plate	[m]
\dot{m}	Mass flow rate	[kg/s]
\dot{V}	Volumetric flow rate	[L/s]
f	Conversion from \dot{V} to \dot{m} for a 5° wedge use for an axisymmetric OpenFOAM simulation	[kg/L]
C_d	Nozzle coefficient of performance	–
A_e	Area of the nozzle exit	[m ²]

Table of Contents

Abstract.....	ii
Summary for Lay Audience.....	iii
Acknowledgments.....	iv
Nomenclature.....	v
Table of Contents.....	viii
List of Tables.....	xi
List of Figures.....	xii
List of Appendices.....	xvi
Chapter 1.....	1
1 General Review.....	1
1.1 Introduction and Background.....	1
1.2 Literature Review.....	6
1.2.1 Under-Expanded Free Jet.....	6
1.2.2 Under-Expanded Impinging Jet.....	11
1.2.3 Numerical Methods.....	14
1.3 Problem Statement and Scope of Work.....	17
Chapter 2.....	18
2 Impinging Jet Validation.....	18
2.1 Methods.....	19
2.1.1 Free Jet Domain.....	19
2.1.2 Impinging Jet Domain.....	20
2.1.3 Numerical Model.....	22
2.1.4 Boundary Conditions.....	24
2.1.5 Domain Initialization.....	26

2.2	Results.....	27
2.2.1	WaveTransmissive Boundary Condition	27
2.2.2	Grid Convergence.....	28
2.2.3	First Mach Diamond	32
2.2.4	Super-Sonic Core	34
2.2.5	Shear Layer Growth.....	35
2.2.6	Recirculation Bubble	35
2.2.7	Impingement Shock	36
2.2.8	Theoretically Predicted Shock	40
2.3	Summary.....	42
	Chapter 3.....	44
3	Single-Phase Nebulizer Modelling	44
3.1	Methods.....	44
3.1.1	Nebulizer Domain.....	44
3.1.2	Boundary Conditions	47
3.1.3	Mesh Generation.....	49
3.1.4	Experimental Validation	54
3.1.5	Parametric Study.....	56
3.2	Results.....	58
3.2.1	Grid Refinement.....	58
3.2.2	Experimental Validation	61
3.2.3	Parametric Study.....	66
3.3	Summary.....	75
	Chapter 4.....	77
4	Conclusions and Recommendations	77
4.1	Conclusions.....	77

4.2 Recommendations.....	78
References.....	80
Appendices.....	85
Curriculum Vitae	89

List of Tables

Table 2.1: Boundary Conditions used for Under-Expanded Free Jet.....	24
Table 2.2: Boundary Conditions used for Under-Expanded Impinging Jet.....	26
Table 2.3: Mesh Characteristics for Under-Expanded Free Jet Grid Convergence Study	29
Table 2.4: Mesh Characteristics for Under-Expanded Free Jet Grid Convergence Study	32
Table 2.5: Shear Layer Growth Angle for Experimental, LES, and RANS Studies	35
Table 2.6: Dimensionless Impingement Shock Position Downstream from Nozzle.....	39
Table 2.7: Dimensionless Impingement Shock Position Downstream from Nozzle, Corrected for Contact Surface	40
Table 2.8: Numerical and Theoretical Mach Number Across the Impingement Shock.....	40
Table 2.9: Numerical and Theoretical Stagnation Pressure Across the Impingement Shock	41
Table 3.1: Boundary Conditions used for Nebulizer Model.....	48
Table 3.2: Mesh Regions used to make the Nebulizer Fluid Domain	54
Table 3.3: Parametric Study Parameters and Magnitude of Low and High State	57
Table 3.4: Mesh Characteristics for Nebulizer Grid Convergence Study	58
Table 3.5: Nozzle Coefficient of Performance for Numerical and Experimental Devices	65
Table 3.6: Parametric Study Cases	75

List of Figures

Figure 1.1: Diagram of how a Typical Nebulizer Supplies Aerosolized Drug to a Patient.....	2
Figure 1.2: Expansion Fan of a Supersonic Flow Over a Convex Plate.....	5
Figure 1.3: Structure of a Moderately Under-Expanded Free Jet, $2.0 < NPR < 4.0$	7
Figure 1.4: Structure of a Highly Under-Expanded Free Jet, $4.0 < NPR < 7.0$	8
Figure 1.5: Moderately Under-Expanded Impinging Jet	11
Figure 1.6: Confined Moderately Under-Expanded Impinging Jet	14
Figure 2.1: Nozzle Geometry from Henderson et al. [10]	20
Figure 2.2: Fluid Geometry and Boundaries for the Free Jet Domain.....	20
Figure 2.3: Impingement Geometry from Henderson et al. [10]	21
Figure 2.4: Fluid Geometry and Boundaries for the Impingement Jet Domain	21
Figure 2.5: Mass Flow into the Nozzle when Started from Non-Initialized Condition.....	27
Figure 2.6: Mach Number vs. Dimensionless Downstream Distance from Nozzle	30
Figure 2.7: Mesh Used for the Impingement Jet Domain.....	31
Figure 2.8: Mesh Used in the Refined Impingement Jet Region.....	31
Figure 2.9: Length of the First Mach Diamond Predicted by the Numerical Model (m).....	33
Figure 2.10: Flow Velocity Along the Central Jet Axis for the Numerical and Experimental Studies [10]	34
Figure 2.11: Streamlines for Impinging Jet Case $L/d=3.65$, with Pressure Contour Background.....	36

Figure 2.12: Velocity Profile Along Jet Axis for an Impinging Jet at Various Distances from the Impingement Plate, Dashed Lines – Experimental [10], Solid Lines – Present Numerical Study	37
Figure 2.13: Mach Contour of $L/d=1.65$	38
Figure 2.14: Mach Contour of $L/d=2.08$	38
Figure 2.15: Mach Contour of $L/d=2.66$	38
Figure 2.16: Mach Contour of $L/d=2.80$	39
Figure 2.17: Mach Contour of $L/d=3.65$	39
Figure 2.18: Mach Contour of $L/d=4.16$	39
Figure 2.19: Mach Number Along Central Axis For each Nozzle to Plate Spacing	41
Figure 2.20: Pressure Along Central Axis For each Nozzle to Plate Spacing.....	42
Figure 3.1: Nebulizer Geometry with the Geometric Features Explored in the Parametric Study Labeled	46
Figure 3.2: Flow Structure Inside the Nebulizer, Showing the Under-Expanded Impinging Jet, Followed by the Low Pressure Toroidal Vortex Downstream.....	46
Figure 3.3: Fluid Geometry and Boundaries for Nebulizer Model.....	48
Figure 3.4: Meshing Regions used to Model the Nebulizer (Left) and Final Mesh Created by the Meshing Macro (Right).....	50
Figure 3.5: Region 1 Meshed using the Automated Pointwise Macro	51
Figure 3.6: All Regions Meshed using the Automated Pointwise Macro.....	52
Figure 3.7: Densely Refined Portion of Region 1, used to Capture the Under-Expanded Impinging Jet, Toroidal Vortex, and Liquid Channel Features	53

Figure 3.8: Mesh Aspect Ratio (Left) and Mesh Skewness (Right), in the Region of Interest for Case LLLH.....	53
Figure 3.9: Schematic of the Experimental Setup used to Measure the Vacuum Pressure Generated inside the Liquid Channel.....	55
Figure 3.10: Image of the Experimental Setup, Device used is Hidden in the Figure.....	55
Figure 3.11: Pressure Signal in the Liquid Channel from the Level 4 Grid Density.....	59
Figure 3.12: Pressure Signal in the Liquid Channel from the Level 4 and Level 5 Grid Density	60
Figure 3.13: KH Style Instabilities found in the Mach Contour Plot (Left) and High Frequency Oscillations Shown in Pressure Contour Plot (Right) for the Level 6 Mesh, Pressure Scaled from 96kPa to 102kPa	60
Figure 3.14: Time-Averaged Vacuum Pressure in the Liquid Channel vs. Number of Grid Elements.....	61
Figure 3.15: Transient Pressure in the Liquid Channel for each Nozzle Diameter Supplied by Wall and Compressor Air	62
Figure 3.16: Flow Streamlines as the Air Navigates the Sharp Corner Entering the Nozzle, Showing the Vena Contracta Phenomenon.....	63
Figure 3.17: Flow Rate vs. Nozzle Diameter for the Compressor Supplier Air, Both Numerical and Experimental Results.....	64
Figure 3.18: Supply Pressure vs. Nozzle Diameter for Wall Supplied Air, Both Numerical and Experimental Results	65
Figure 3.19: Vacuum Pressure Measured in the Liquid Channel for Wall and Compressor Air, Both the Numerical and Experimental Results.....	66
Figure 3.20: Vacuum Pressure Observed in the Liquid Channel for Each Geometry, When Supplied by Wall Air	67

Figure 3.21: Influence and Interaction of Various Parameters on the Liquid Channel Vacuum Pressure.....	67
Figure 3.22: Time-Averaged Velocity Contour Plots, Draft Angle in Low State (LLLL - Left) and High State (LLLH - Right).....	69
Figure 3.23: Time-Averaged Absolute Pressure Contour Plots, Draft Angle in Low State (LLLL - Left) and High State (LLLH - Right).....	69
Figure 3.24: Time-Averaged Velocity Contour Plots, Nozzle Diameter in Low State (LLLL - Left) and High State (LLHL - Right).....	71
Figure 3.25: Time-Averaged Absolute Pressure Contour Plots, Nozzle Area in Low State (LLLL - Left) and High State (LLHL - Right).....	71
Figure 3.26: Time-Averaged Velocity Contour Plots, Distance to Baffle in Low State (LLLL - Left) and High State (LHLL - Right).....	72
Figure 3.27: Time-Averaged Absolute Pressure Contour Plots, Distance to Baffle in Low State (LLLL - Left) and High State (LHLL - Right).....	73
Figure 3.28: Time-Averaged Velocity Contour Plots, Proudness in Low State (LLLL - Left) and High State (HLLL - Right).....	74
Figure 3.29: Time-Averaged Pressure Contour Plots, Proudness in Low State (LLLL - Left) and High State (HLLL - Right).....	74
Figure D.1: Velocity Contour Plot with Streamlines, Showing the Recirculation Bubble being Resolved by a Three-Dimensional Model	88

List of Appendices

Appendix A: OF Case Setup for the Nebulizer Model.....	85
Appendix B: Code used for Nebulizer Mesh Generating Macro.....	86
Appendix C: Tabulated Results from the Experimental Validation Study.....	87
Appendix D: Three-Dimensional Under-Expanded Impinging Jet Study.....	88

Chapter 1

1 General Review

1.1 Introduction and Background

Under-expanded free jets are an important flow phenomenon found in many engineering and natural processes such as propulsion, medical devices, and fuel injectors. In an under-expanded free jet, a compressible fluid is accelerated beyond the speed of sound while flowing from a high-pressure reservoir into a low-pressure environment. In many applications, the jet will impinge on a solid surface before the super-sonic region has decayed and the jet is shocked back to a sub-sonic velocity at the impingement point. These jets produce a number of physical features such as compressible shock waves, turbulent mixing, or acoustic features that may be important for a given engineering application. Properly understanding the features and impact they have on their surroundings can help improve decision making and meet engineering design criteria.

Pneumatically driven nebulizers are an example of a medical device that uses an under-expanded free jet to convert a liquid drug into an aerosolized drug for respiratory drug delivery. In the nebulizer, the under-expanded free jet impinges on a plate, which redirects the flow radially before forming a low-pressure rotating toroidal flow downstream of the impingement point. The low-pressure of the toroid is used to entrain liquid drug that is then broken up into small droplets by the extreme conditions of the impinging jet. The key parameter of the device which can be used to improve the quality of care given to a patient is the respirable rate, which is the volume of droplets produced within the required size range to be used for treatment. Increasing the respirable rate improves patient care by reducing the treatment time required to receive the prescribed drug (Figure 1.1).

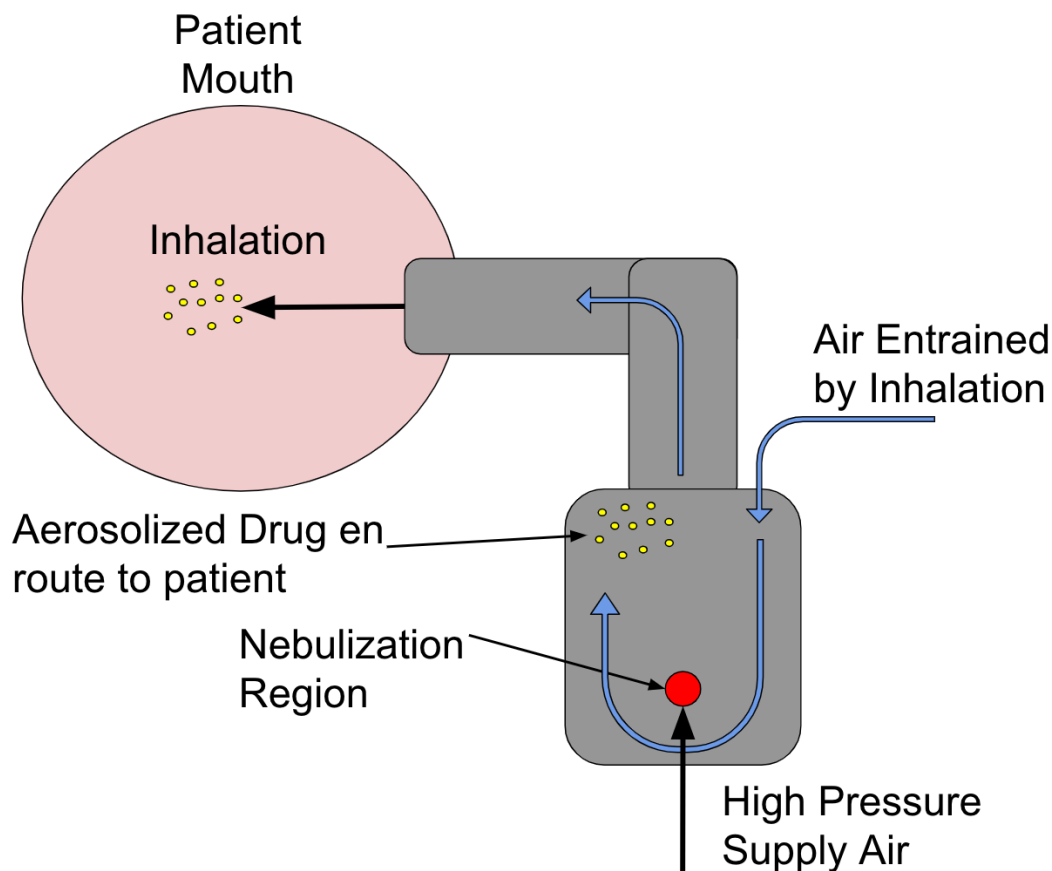


Figure 1.1: Diagram of how a Typical Nebulizer Supplies Aerosolized Drug to a Patient

To date, the design of nebulizer devices has been done mainly by using an experimental trial and error approach, which can be expensive and tedious. While the devices developed under this approach are functional, without intensive experimentation, it cannot be known whether the device is functioning at its optimum. To gain this insight into the performance of the device at a lower cost, *Computational Fluid Dynamics* (CFD) can be used as a tool when studying the internal flow of the devices. CFD packages for modelling compressible and incompressible flows are available as commercial, custom, and open-source programs. However, given the flow velocity and complex flow features that form in compressible jets, the level of expertise and computational cost associated with studying these cases computationally can be intimidating to many engineering design groups. To this point, and in terms of fluid mechanics and CFD expertise, a

sophisticated problem can often be simplified by understanding that many of the complex features that are captured by a comprehensive numerical model may not be required to capture the features of interest to a specific design group. Thus, characterizing what features are important for a specific group is the first step, then determining whether those flow features can be accurately captured using simplified numerical model can enable engineering design teams with fewer computational resources to gain valuable insight into their applications of under-expanded impinging free jets.

Compressible flow is considered to be any flow where the changes in density are significant to the overall behaviour of the fluid [1]. This can occur either through significant changes in temperature or through flow velocities that are considerable compared to the speed of sound. The later variant of compressible flow will be explored in detail in this thesis. A key concept when considering compressible flow systems is the speed of sound in a given fluid, described as Eq 1.1.

$$c = \sqrt{\gamma RT / M} \quad 1.1$$

Where, the speed of sound in an ideal gas (c) is a function of its temperature (T), the ideal gas constant (R), the molecular mass of the gas (M), and its ratio of heat capacities (γ). The ratio of heat capacities is another important property that helps describe the behaviour of compressible fluids (Eq. 1.2).

$$\gamma = \frac{c_p}{c_v} = 1.4 \text{ for air} \quad 1.2$$

Under the isentropic assumption, the first law of thermodynamics dictates that the total enthalpy of a compressible, isentropic flow is constant.

$$h_0 = h + \frac{U^2}{2} = \text{const} \quad 1.3$$

Where h_0 is the stagnation enthalpy, h is the flow enthalpy, defined as $h = u + Pv$, where U is the flow velocity, u is the internal energy, P is the absolute pressure, and v is the specific volume. This equation shows that while the energy in the flow is

constant, it can be transferred between internal energy and kinetic energy as it changes velocity. Using the flow enthalpy, the conditions of the fluid can be determined by knowing the stagnation condition and fluid velocity, where the stagnation properties are the properties of the fluid at rest [1].

$$T_0 = T + \frac{U^2}{2c_p} \quad 1.4$$

$$\frac{P_0}{P} \Big|_s = \left(\frac{T_0}{T} \right)^{\gamma/(\gamma-1)} \quad 1.5$$

When the fluid is brought to rest adiabatically the above equations will hold true, however when there are losses, the stagnation pressure is reduced as a result.

The speed of a compressible flow can be described in non-dimensional terms using the Mach number. This property describes the dimensionless velocity of a fluid by taking the ratio of the local velocity and the local speed of sound, shown as Eq. 1.6 [1].

$$Ma = \frac{U}{c} = \frac{U}{\sqrt{\gamma RT}} \quad 1.6$$

Depending on the Mach number, the flow is referred to differently. When a flow is well below the speed of sound ($U \ll c$) the flow is considered subsonic; at this point the fluid can be considered incompressible. As it approaches the speed of sound ($U < 0.3c$) the flow is transonic; in this regime compressibility effects begin to impact the flow. When the fluid reaches the speed of sound ($U = c$) it is considered sonic, and above this point ($U > c$) the flow is supersonic.

Discontinuities in the flow properties commonly occur in supersonic flows when the flow direction or velocity suddenly changes, known as a *shock*. These discontinuities can either be one dimensional, a normal shock, or two-dimensional, an oblique shock. A normal shock is characterized by a sudden deceleration of the flow, accompanied by recovery of stagnation pressure and temperature, and is effectively a one-dimensional phenomenon. A normal shock is not an isentropic process and is highly irreversible, so

the stagnation pressure is not fully recovered. Therefore, the pressure recovered downstream of a normal shock is lower than the stagnation pressure of the flow upstream. This results in an increase in entropy that is a function of the strength of the shock, which is proportional to the upstream Mach number. The pressure recovered downstream of a shock is provided by Eq. 1.8, where x is upstream of the normal shock, and y is downstream [1].

$$M_y = \sqrt{\frac{2+(\gamma-1)M_x^2}{2\gamma M_x^2-(\gamma-1)}} \quad 1.7$$

$$\frac{P_{0y}}{P_{0x}} = \left[\frac{2\gamma M_x^2-(\gamma-1)}{\gamma+1} \right]^{1/(\gamma-1)} \left[\frac{(\gamma+1)M_x^2}{2+(\gamma-1)M_x^2} \right]^{\gamma/(\gamma-1)} \quad 1.8$$

All normal and oblique shocks must be compression shocks since an expansion shock would result in a decrease in entropy, violating the second law of thermodynamics. However, when a supersonic flow passes over a convex surface or a sudden increase in area, the pressure decreases and velocity increases. This process occurs over a series of expansions that never coalesce into an expansion shock, instead forming an *expansion fan* known as a Prandtl-Mayer expansion fan (Figure 1.2). Since the waves never coalesce and the process is gradual, it can be treated as an isentropic phenomenon. Similarly, flow over a concave wall will produce a compression fan, which tends to coalesce into an oblique shock [1].

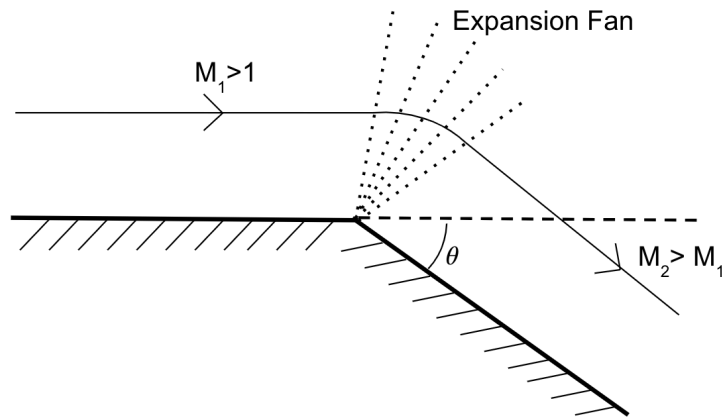


Figure 1.2: Expansion Fan of a Supersonic Flow Over a Convex Plate

An overview of the relevant background into the flow in relation to the nebulizer will be describe in the remainder of this chapter. It will be broken down into two main sections, the physics present in the under-expanded impinging jet and the numerical methods most commonly used for this application.

1.2 Literature Review

1.2.1 Under-Expanded Free Jet

An under-expanded free jet occurs when a fluid is ejected from a high-pressure reservoir into a lower-pressure environment. The criteria for a jet to be under-expanded in a converging nozzle is the ratio of the supply pressure and the ambient pressure must exceed the critical value required for the flow to reach the speed of sound at the nozzle exit:

$$\frac{P_0}{P} = \left(\frac{\gamma+1}{2}\right)^{\gamma/\gamma-1} [1] \quad 1.9$$

Here, P_0 is the stagnation or reservoir pressure, and P is the pressure of the fluid at the nozzle exit. For air, $\gamma = 1.4$, which yields a pressure ratio of 1.89. Thus, once the supply pressure of the gas exceeds 1.89 times the ambient pressure, the flow at the end of a converging nozzle will remain at speed of sound (Mach 1). With a constant supply pressure, further decreases in the ambient pressure will not impact the mass flow rate through the nozzle, a phenomenon commonly known as *choked flow*. The mass flow through a choked flow nozzle is only dependent on the stagnation pressure and the nozzle area. When the stagnation pressure is increased, Eq. 1.9 can be used to predict the pressure of the fluid at the nozzle exit, since the flow velocity is fixed at Mach 1. This increases the fluid density at the nozzle exit while maintaining a fixed velocity, therefore increasing the mass flow through the nozzle. The ratio between the supply pressure and the ambient pressure is a key characteristic when defining an under-expanded free jet and is known as the *Nozzle Pressure Ratio* (NPR) (Eq. 1.10).

$$NPR = \eta_0 = P_0/P_{atm} [1] \quad 1.10$$

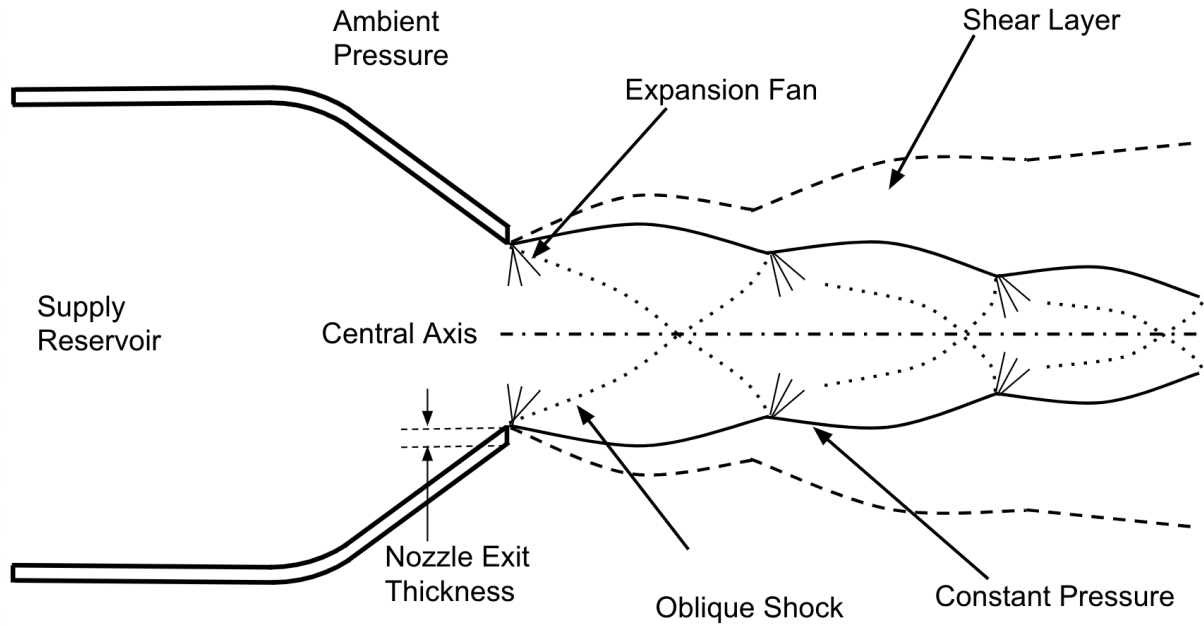


Figure 1.3: Structure of a Moderately Under-Expanded Free Jet, $2.0 < NPR < 4.0$

For NPR in air that slightly exceeds the critical pressure ratio ($2 < \eta_0 \lesssim 4$), the flow is considered moderately under-expanded [2]. These jets contain a repeating standing wave pattern where the diameter of the supersonic jet core expands and contracts, known as *Mach Diamonds*. Early descriptions of Mach diamonds were provided by Prandtl in 1904 [3] and are formed by the high-pressure jet at the exit plane expanding through Prandtl-Mayer expansion fan as it enters a lower pressure environment (Figure 1.3). Flow passing through the expansion fan is accelerated above Mach 1. As the expansion fan reaches the constant pressure line, where the jet pressure matches the ambient pressure, they are reflected back into the supersonic jet as a compression fan (Figure 1.3). These reflected pressure waves converge as a single conical oblique shock wave that meets in the axis of the free jet, increasing the entropy in the jet flow [2], [4] (Figure 1.3).

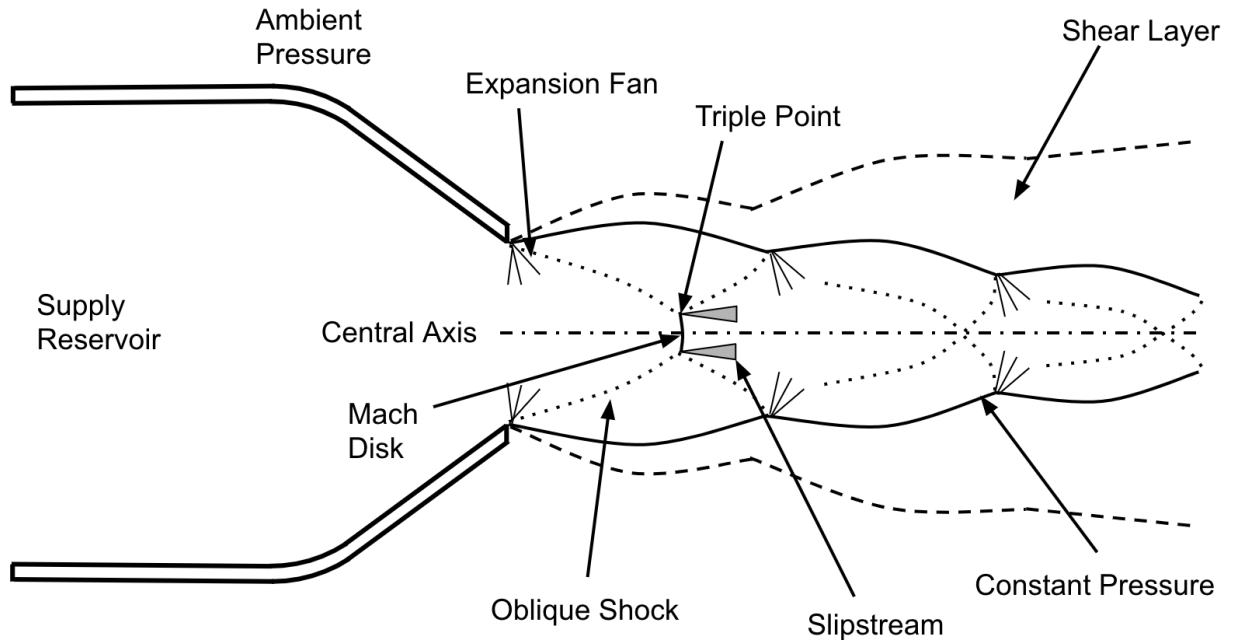


Figure 1.4: Structure of a Highly Under-Expanded Free Jet, $4.0 < \text{NPR} < 7.0$

Near $\text{NPR}=3.8$, the conical oblique shock wave will form a circular normal shock wave along the jet axis, known as the *Mach disk* [4]. A small subsonic zone is present downstream of the Mach disk, which generates high levels of turbulence in the slipstreams, before accelerating the flow above Mach 1 (Figure 1.4). While the NPR is the main factor influencing the size and position of the Mach disk, for converging-diverging nozzles the position is increased by a higher exit Mach number while the diameter is decreased. Nozzle geometry seems to play no role in the Mach disk position downstream, but the size decreases with increasing nozzle angle [2]. The thickness of the nozzle exit also seems to have some impact on the presence of a Mach disk at a moderate NPR. Weightman [5] observed a Mach disk in a free jet with a NPR as low as 3.4 when using a nozzle with a large nozzle edge thickness, and no Mach disk with a small nozzle edge thickness (Figure 1.3). Since the Mach disk is a highly irreversible process, the entropy increase in a highly under-expanded free jet is greater than in the moderately under-expanded cases.

While no exact method of estimating the length of the first Mach diamond has been developed, there are several analytical and empirical methods have been proposed. The earliest method was the Prandtl equation (Eq. 1.11) [3].

$$\Delta_1 = 1.2\sqrt{\eta_0 - 1.9} \quad 1.11$$

$$\text{Where: } \Delta_1 = \frac{L_1}{D_e}$$

Where Δ_1 is the dimensionless length and L_1 is the dimensioned length of the first Mach diamond, and D_e is the diameter of the nozzle exit. Powell's experiments [4] showed that this equation over-predicted the length, and a constant of 1.16 instead of 1.2 had closer agreement. Prandtl's work is only applicable to the first Mach diamond where losses due to the turbulent shear layer are minimal. Downstream of that point, the length of subsequent Mach diamonds can be predicted using a method developed by Tam et al. [6] (Eq. 1.12).

$$\Delta_s = \pi \frac{\sqrt{(Ma_j^2 - 1)}}{2.405} \quad 1.12$$

$$\text{Where: } Ma_j = \sqrt{\frac{2}{\gamma - 1} \left[\eta_0^{\frac{\gamma - 1}{\gamma}} - 1 \right]} \quad 1.13$$

Experimentally, some variability in the length of the first Mach diamond is found, but it can be approximated using the following empirical equation [2] (Eq. 1.14).

$$\Delta_1 = 1.52\eta_e^{0.437} + 1.55(\sqrt{2M_e^2 - 1} - 1) - 0.55\sqrt{M_e^2 - 1} + 0.5 \left(\frac{1}{1.55} \sqrt{(\eta_e \sqrt{M_e^2 - 1} - 1)} \right) \quad 1.14$$

Each method clearly shows that the length of the first Mach diamond is dependent on:

1. The Mach number at the exit plane of the nozzle
2. The pressure ratio found at the exit plane of the nozzle

This empirical equation was found considering converging-diverging nozzles. For converging only nozzles, the Mach number at the exit plane will reach unity and the pressure ratio at the nozzle exit will be known from the overall NPR using Eq. 1.9. When dealing with a converging only nozzle the length of the first Mach diamond seems to only depend on the NPR, which is consistent with Prandtl's and Tam's equations (Eq. 1.11, Eq. 1.12).

Surrounding the supersonic potential core is the shear layer. This region is characterised by subsonic and highly turbulent flows when the jet Reynolds number is sufficiently high, $Re_j > 10,000$, which is typical for most under-expanded free jet cases [2]. The Reynolds number for these jets is found using the jet velocity at the nozzle exit and the distance to the first Mach disks [2]. The characteristics for identifying the shear region taken from Dauptain et al. [7], which is defined as the region where flow velocity is between 50 and 300m/s for air [7]. The shear layer typically grows linearly as it flows downstream [2], [8]. While the spacing of the shock structures of an under-expanded free jet appear to be only dependent on the NPR, the decay of supersonic core is largely caused by the turbulence in the shear layer. Increased turbulent stresses in the shear layer will increase the decay rate of super-sonic core of the jet, as it increases momentum transfer from the jet core to the surrounding fluid [6]. The total length of the supersonic core can be estimated using $\frac{L_c}{a} = [1.81\eta_0] + 2.9$, which is based on the NPR and nozzle diameter [9], however their work was conducted on nozzle diameters less than 1mm, which have a lower Reynolds numbers than larger nozzles found in many engineering applications. Interestingly, Phalnikar et al. [9] found that their equation under-predicts the length of the sonic core for larger diameter nozzles, contradicting other sources.

An important characteristic of under-expanded free jet flow for many engineering applications is the acoustic frequencies emitted. These systems emit high intensity, high frequency tones which can be damaging to engineering hardware located around them and unpleasant to nearby humans. Primary mechanisms for high frequency noise emissions are caused by instabilities in the shear layer interacting with oblique shock waves [2]. While these acoustic frequencies are important to many engineering applications, they fall outside the scope of this work and will not be considered further.

1.2.2 Under-Expanded Impinging Jet

Quite commonly in engineering applications, the under-expanded free jets are found to impinge on solid surfaces. In these cases, the flow is rapidly decelerated and redirected to flow radially outward. An impingement shock is formed preceding the impingement plate, and a recirculation zone forms between the impingement shock and the impingement plate [7], [10]–[12]. This results in four distinct features found in an under-expanded impinging jets:

1. Super Sonic Core
2. Shear region
3. Impingement shock
4. Recirculation Bubble

Along with the changes introduced by the shock, the method of sound production changes from an edge-based instability phenomenon, to an acoustic feed-back loop [13] (Figure 1.5).

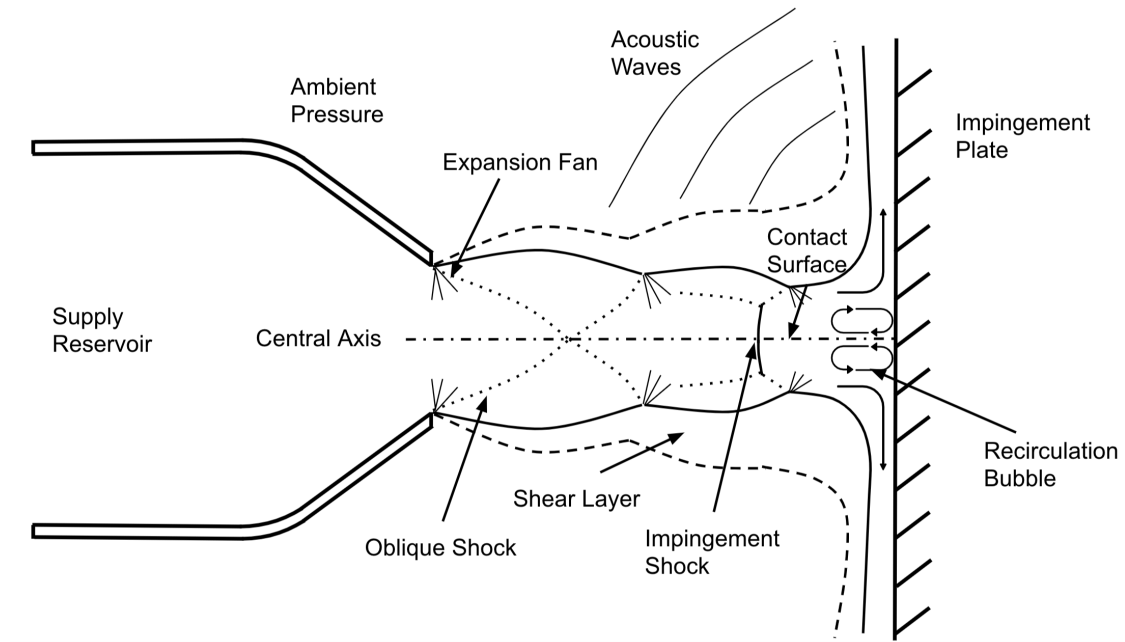


Figure 1.5: Moderately Under-Expanded Impinging Jet

The feed-back loop occurs when small disturbances at the lip of the nozzle generate instabilities. These instabilities travel along the free jet in the shear layer region, and will come in contact with the impingement plate. When the instabilities impact the impingement plate, they generate strong acoustic waves which are free to propagate back to the lip of the nozzle. These acoustic waves then become the small disturbances which generate the instabilities in the jet flow, completing the feedback loop [13].

Several different kinds of instabilities can be found in this type of flow. The three main kinds are Kelvin-Helmholtz (KH) [2], vortical instabilities (Taylor-Goertler (TG)) [4], [14], and flapping [11]. Flapping instabilities seem to be highly geometry dependant [11]. These instabilities are found to perturb shockwaves in the free jet and at the impingement shock [2], [4]. TG style instabilities form in the shear layer of the free jet, generating a spiraling flow which has an axis of rotation parallel to the flow of the jet. In practise, these flow structures are formed by small imperfections in the nozzle edge, that grow as they move downstream [14]. In numerical simulations, they are artificially locked onto perturbations found in the computational grid of the nozzle edge [7]. Since these flows are three dimensional in nature, they cannot be captured using an axisymmetric CFD simulation. Thus, any studies of these flows using an axisymmetric model should not be influenced by the presence of TG instabilities.

Behind the normal shock exists a zone referred to as the recirculation bubble (Figure 1.5). This recirculation pattern results in a reverse flow along the central axis in the impingement region. First described by Donaldson et al. [11], this flow feature was experimentally demonstrated using a highly viscous ink placed in the impingement zone. After several seconds under the impinging jet, the ink demonstrated a flow pattern which indicated the presences of the recirculation zone [11]. These ink streaks showed a series of node and saddle points from which the flow converged to or diverged from, producing a three-dimensional effect within the recirculation bubble [7], [11]. The recirculation bubble has been verified by both experimental and numerical studies since its initial discovery by Donaldson [5], [7], [10], [15]. Kim et al. has suggested the recirculation bubble is dependent on the nozzle-to-plate spacing [15]. Their studies showed the cooling rate of an under-expanded free jet on a plate to be dependent on where in the Mach

diamond structure the plate was placed. It is believed the changes to cooling rate is due to a disappearance of the recirculation bubble at certain nozzle to plate spacing, although no direct observations are available in their study [12]. Even though the flow seems to have three-dimensional features, it has been successfully captured using an axisymmetric numerical model, indicating that the recirculation zone is an axisymmetric phenomenon [15].

When a subsonic impinging jet is confined by an large nozzle exit (Figure 1.3), a *toroidal recirculation zone* will form downstream of the impingement point (Figure 1.6). The toroidal vortex is accompanied by a region of sub-atmospheric pressure, that is not present when the jet is unconfined [16]. The position of the toroidal vortex moves radially outward and pressure within the low-pressure region decreases for increasing nozzle to plate spacing and increasing Reynolds numbers [16]–[18]. A secondary counter rotating vortex has been mentioned in the literature [19], where the experimental results of Herrada et al. [20] suggest the counter rotating vortex is positioned radially further from the jet axis than the main vortex is. This phenomenon has been studied primarily for heat transfer applications and at the time of writing this document no literature on confined under-expanded impinging jets is available.

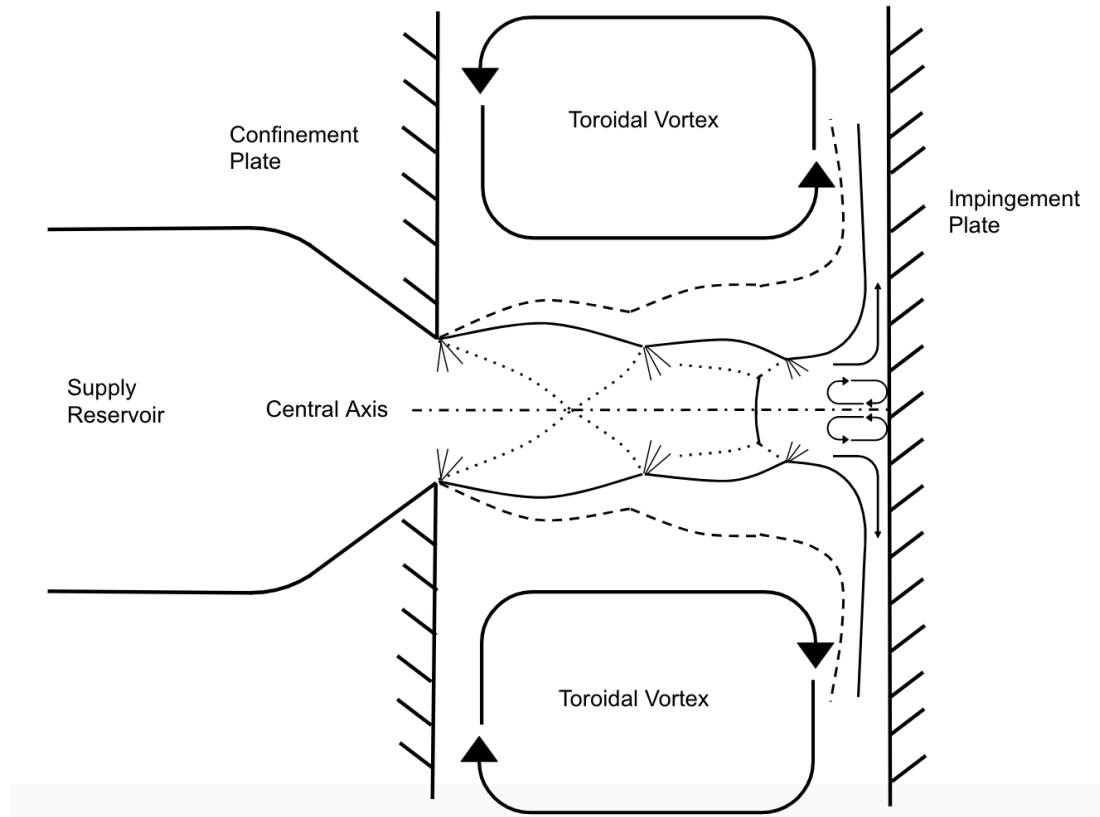


Figure 1.6: Confined Moderately Under-Expanded Impinging Jet

1.2.3 Numerical Methods

The flow features of interest in a given under-expanded impinging jet problem should be considered when selecting the solver and turbulence model used. Primary characteristics of importance are the presence of shocks in the super-sonic core, and the turbulent shear region. Many past studies have looked at modelling under-expanded impinging flows and have found that numerical models can accurately predict the flow structures present, those methods will be described in this section.

Under-expanded free and impinging jets have been numerically modelled in the past using commercial software such as Ansys Fluent [8], [21], CFX [22], Star CCM [23], custom in house software [7], [24]–[27], and open source programs such as *OpenFOAM* (OF) [8], [28], [29]. When modelling this style of flow with compressible shocks, most past research has used density based solvers, rather than pressure based solvers. While pressure based solvers can in theory be used for all flow speeds [30],

density based solvers are preferred since they provide greater accuracy near shock structures [26], [31], [32]. *RhoCentralFoam* (rCF) offered by OF, is a density based solver that is capable of simulating compressible jets.

RCF is a transient, density based, segregated, compressible flow solver. The basic algorithm used is based on the central difference scheme developed by Kurganov and Tadmor [33]. The solver works in four main steps for each time step, as shown [34]:

1. Solve for density using the continuity equation
2. Solve for velocity using the momentum equation
3. Solve for temperature using the energy equation
4. Solve for pressure using the equation of state

Several researchers have compared rCF to commercial CFD programs for a variety of supersonic flow conditions. Chen et al. [31] compared rCF to Fastran in an inviscid simulation of flow over a flat plate and uniform flow impinging on a cylinder. The results showed good agreement with each other and experimental data, however rCF captured more severe pressure oscillations at the leading edge of the flat plate than Fastran did. Chen et al. [31] also looked at the impact that 1st and 2nd order convective discretization schemes had, and found that the 2nd order schemes provided excessive correction at the impingement point of the cylinder problem, resulting in some error. rCF in its unmodified form has been used for modelling under-expanded free jets with a NPR of 4.00 by Zang et al. [8], [28]. Their work compared the results obtained from rCF to a commercial solver (Ansys Fluent v18.2) and found close agreement between the two programs results once steady state conditions were reached. The commercial solver predicted a slightly greater the maximum velocity by approximately 30 m/s, however the exact difference was not stated [8].

Since the turbulent shear layer both transfers energy from the jet to the surroundings, and is the primary source of acoustic phenomena, it is important to select a turbulence model that is capable of resolving the turbulent features of interest. Many past studies have used *Large Eddy Simulation* (LES) turbulence models [7], [23], [25], [26], [29], [35], which shows good agreement with experiments for many flow features.

Dauplain et al. [7] looked at the Mach disk, recirculation zone, shear layer growth, and acoustic feedback in his work. The Mach disk after the first Mach diamond was over-predicted in the numerical work, which is consistent with Hamzehloo et al. [29]. The error found when predicting the Mach disk may be the result of measurement error in the experimental digital particle imaging velocimetry (DPIV) technique used. The sudden deceleration in flow velocity across the shock is difficult to capture since the oil droplets used in DPIV carry inertia with them as they cross the shock. Acoustic phenomena were well predicted by LES, indicating that the large coherent structures in the shear layer were being resolved. However, the growth of the shear layer was over-predicted when compared to experiment [7].

While LES shows strong agreement with experimental results, the computational cost associated with this technique is prohibitive for applications such as engineering design. The primary alternative is a two-equation model, which determines a turbulent viscosity that is applied to the mean flow [36]. Several two-equation options are available and have been explored for the case of interest that include the $k - \epsilon$ [22], [37], $k - \omega$ [22], [24], and $k - \omega$ SST [8], [21], [28], [22], [29]. The $k - \omega$ SST model was the most extensively explored of the options available and showed good agreement with experimental results. Dhavarath et al. [22] conducted a comparison study between each of the three two-equation models mentioned and the LES technique on an under-expanded free jet impinging on an inclined plate. Their findings showed comparable jet structures were obtained by the two-equation and LES models [22], [29]. Hamzehloo et al. [29] also conducted a comparison between LES and $k - \omega$ SST, finding some differences in the shear layer behaviour. Primarily, the coherent KH instabilities were not able to be resolved using a two-equation model, while LES was able to adequately capture these features [8], [29]. Once steady state was obtained, no transient behaviours in the shear layer were present when using the $k - \omega$ SST model. Within the shock structures of highly under-expanded jets ($NPR > 3.8$), the strength of the Mach disk is under predicted by the $k - \omega$ SST model [29]. This yields similar results for both LES and $k - \omega$ SST through the first Mach diamond, and an over-prediction in the flow velocity in subsequent Mach diamonds [29].

From the literature available, rCF with a $k - \omega$ SST turbulence model should provide a good estimation of the flow structure found in an under-expanded free jet. However, large coherent structures in the shear layer cannot be resolved by the $k - \omega$ SST model, and the flow velocity downstream of the first Mach diamond will be over-predicted for cases where the NPR is 3.8 or greater.

1.3 Problem Statement and Scope of Work

The majority of past research has been conducted to better understand the underlying physics within under-expanded impinging free jets. As a result, the geometries studied on the past were greatly simplified and numerical models have used massively complex 3D simulations with LES turbulence models. Further, the nebulizer device in its present geometry has not been studied in this fashion before, along with the toroidal vortex flow features downstream of the impingement point that are utilized by the device. The present work aims to reduce the computational cost by using an axisymmetric assumption with a two-equation $k - \omega$ SST turbulence model. OF will be used in its downloaded state, without any user modifications made to the code. The reduced cost model will be validated against past experimental studies in a simplified geometry. Once the reduced cost model is validated, the nebulizer will be modelled using the same technique, where its results will be validated against experimental data gathered at Western University. The model will explore only a single-phase jet, characterising only the compressible air flow and not including the liquid phase of the device. To determine the performance of the device, the vacuum pressure determined in the single-phase model will be used as a proxy for the respirable rate. Modelling the device as a two-phase system with both the compressible air and liquid drug will fall outside the scope of this work. The final study of this thesis is a parametric study, where four important geometric features will be explored to determine their influence on the behaviour of the device.

Chapter 2

2 Impinging Jet Validation

Given the complexity of the physics involved in simulating flow in a nebulizer, the validation process was completed in phases, each validating a simpler physical model to build confidence in the capabilities of rCF. Initial simulations modelled an under-expanded free jet, then an under-expanded impinging jet, to determine the prediction accuracy of the methods for the features of interest.

RCF was validated by recreating the setup of a well-documented under-expanded free jet, with a similar NPR to the one found in the nebulizer. The case used was from a study conducted by Henderson et al. [10], which explored an under-expanded impinging jet with a NPR of 4.03. Henderson's study was selected since they provide data for both the free jet and impinging jet cases, enabling both to be validated from a single study. The downside to the study chosen is its primary focus on the impinging jet case, leaving out some information about the free jet that would have been useful to compare against. A similar numerical and experimental study was conducted by Dauplain et al. [7], so the geometry was taken from Henderson while methods of comparing numerical and experimental results were taken from Dauplain.

Within an under-expanded free jet there are three key regions, i) the inviscid core ii) the shear layer, and iii) the far field zone. These regions will be compared to the experimental data provided by Henderson, to determine the degree of accuracy provided by the chosen solver. Henderson used a simple converging nozzle geometry, which limits the number of factors that influenced the developed jet. Flow velocity measurements by Henderson were captured using particle imaging velocimetry (PIV), while shadowgraph techniques were used to capture the flow structure.

2.1 Methods

2.1.1 Free Jet Domain

For the free jet case, the impingement plate was excluded from the model leaving only the nozzle. The free jet was modelled well beyond the super-sonic core by placing the “Outlet” at $20d$ downstream of the nozzle exit, which provides more than the $10d$ distance typically required for the super-sonic core to become sub-sonic. Parallel to the free jet was “Inlet Freestream 2”, which was located at $5d$ away from the axis of symmetry. Finally, “Inlet Freestream 1” was located upstream of the nozzle at the same location where the nozzle inlet begins (Figure 2.2). “Inlet Freestream 1” and “Inlet Freestream 2” are both used to allow air entrained by the free jet to enter the domain. Since the case was run as an axisymmetric model, the domain was generated as a small 5° wedge, rotated about the axis of symmetry. In OF, any small wedge angle can be used, however 5° is the standard value used for many cases.

The nozzle is modelled on the left hand side of the domain as shown in Figure 2.2, and is shown as a very thin wall ($t=1.27\text{mm}$) that converges toward the axis of symmetry. The inlet is placed at the beginning of the nozzle geometry, where the pipe diameter is $d=152\text{mm}$. A rounded inlet redirects the flow from entering parallel to the domain to converging at 30° . A small rounded edge was applied to the nozzle exit to ensure the flow left the nozzle parallel to the jet axis. Since the exact radius of the nozzle exit was not specified, a dimensionless radius of $0.12d$ was used to approximate the experimental study.

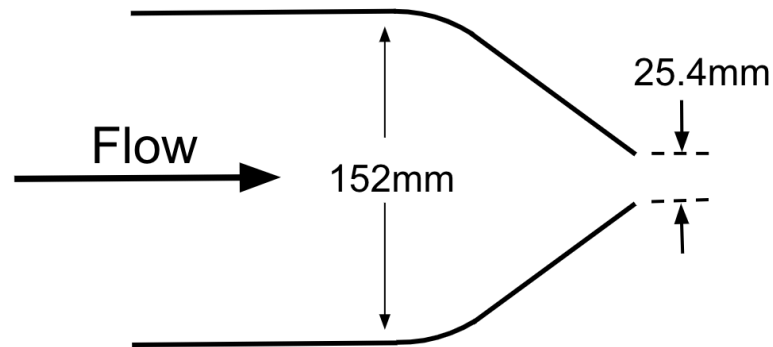


Figure 2.1: Nozzle Geometry from Henderson et al. [10]

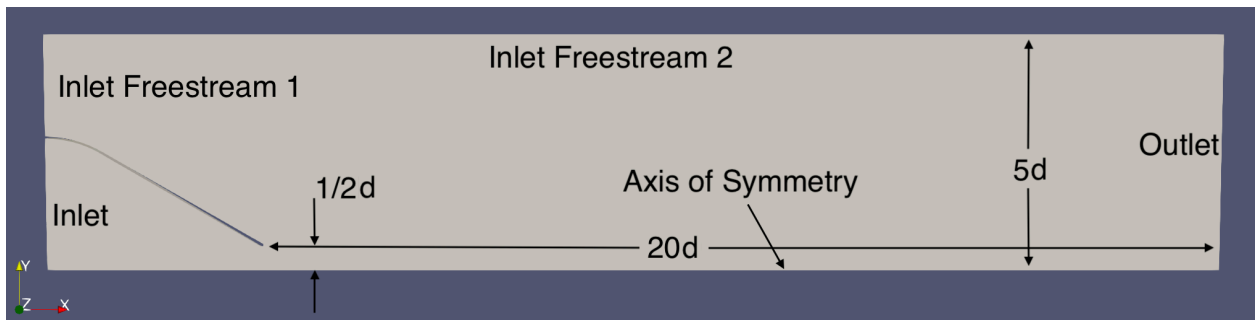


Figure 2.2: Fluid Geometry and Boundaries for the Free Jet Domain

2.1.2 Impinging Jet Domain

In addition to the under-expanded free jet, the model was expanded to include the impingement plate used by Henderson et al. [10]. In Henderson's experiment, the free jet impinges on a very large rectangular plate that is 533mm \times 610mm, which is 21 times and 24 times the nozzle diameter respectively (Figure 2.3). Given the long distance, it is assumed that the edge of the plate has a minimal impact on the behaviour of the impinging jet.

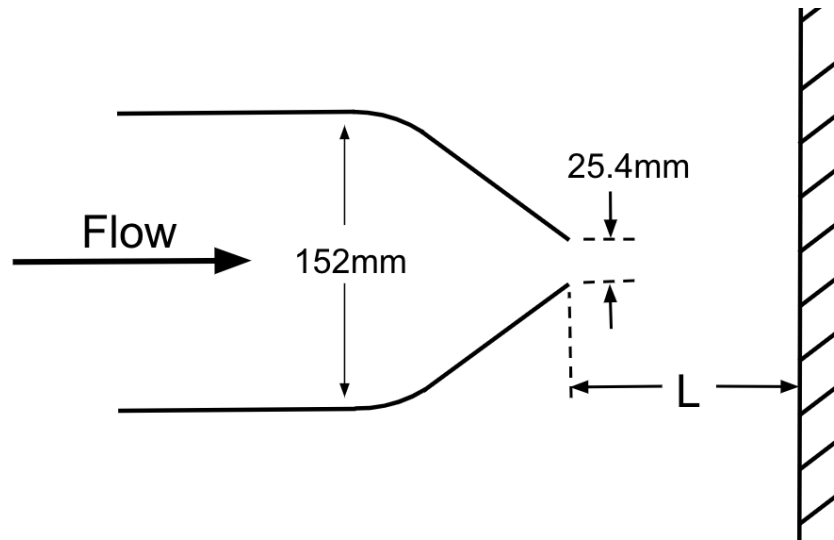


Figure 2.3: Impingement Geometry from Henderson et al. [10]

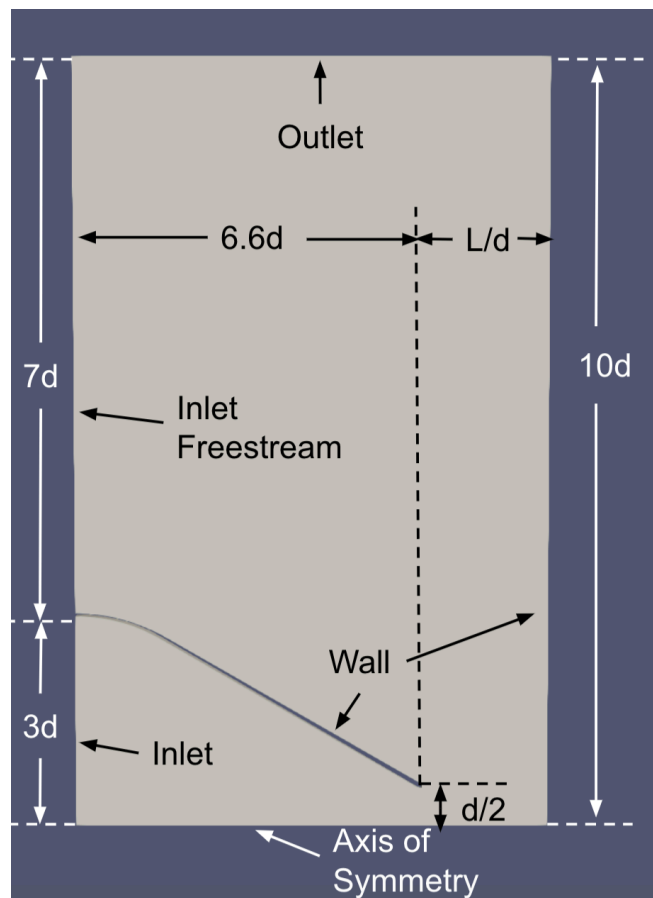


Figure 2.4: Fluid Geometry and Boundaries for the Impingement Jet Domain

The impinging jet case placed the impingement plate at various distances downstream of the nozzle exit, as tested experimentally, with $L/d=[1.65, 2.08, 2.66, 2.80, 3.65, 4.16]$. Each nozzle to plate spacing was in a different location in the Mach diamond structure. Along the wall, the domain extends $10d$ radially downstream from the axis of symmetry, therefore it represents a circular impingement plate with a total diameter of $20d$.

2.1.3 Numerical Model

As discussed earlier, rCF uses a density based approach to solving the continuity, momentum, and energy transport equations, while the pressure in the domain is determined using the equation of state. The transport equations are given as follows [38].

$$\frac{\partial \rho}{\partial t} + \nabla \cdot (\rho \mathbf{U}) = 0 \quad 2.1$$

$$\frac{\partial(\rho U)}{\partial t} - \nabla \cdot [U(\rho U)] + \nabla P + \nabla \cdot \mathbf{T} = 0 \quad 2.2$$

$$\frac{\partial(\rho E)}{\partial t} - \nabla \cdot [U(\rho E)] + \nabla \cdot [UP] + \nabla \cdot (\mathbf{T} \cdot \mathbf{U}) + \nabla \cdot \mathbf{j} = 0 \quad 2.3$$

$$P = \frac{\rho}{\psi} \quad 2.4$$

$$\psi = (RT)^{-1} \quad 2.5$$

Where \mathbf{T} is the viscous tensor, \mathbf{j} is the diffusive heat flux, and E is the total energy density.

Turbulence is modelled with the $k-\omega$ SST model, which is a two equation model that blends the $k-\epsilon$ and $k-\omega$ models. Near the walls and boundary layer, the $k-\omega$ model is dominant, while the $k-\epsilon$ is primarily used in the free stream regions. Since the model is being applied to a compressible solver where temperature is included in the flow, a turbulent viscosity (μ_t) and thermal diffusion (α_t) term are generated by the model and applied to the flow. These terms are determined using the following transport equations

for the turbulence specific dissipation rate Eq. 2.6, the turbulent kinetic energy Eq. 2.7, and the turbulent viscosity Eq. 2.8 [39].

$$\begin{aligned} \frac{D}{Dt}(\rho\omega) = \nabla \cdot (\rho D_\omega \nabla \omega) + \frac{\rho\gamma G}{\nu} - \frac{2}{3}\rho\gamma\omega(\nabla \cdot u) \\ - \rho\beta\omega^2\rho(F_1 - 1)CD_{k\omega} + S_\omega \end{aligned} \quad 2.6$$

$$\frac{D}{Dt}(\rho k) = \nabla \cdot (\rho D_k \nabla k) + \rho G - \frac{2}{3}\rho k(\nabla \cdot u) - \rho\beta^*\omega k + S_k \quad 2.7$$

$$\mu_t = a_1 \frac{k}{\max(a_1\omega, b_1 F_{23} S)} \quad 2.8$$

Where:

β^*	a_1	b_1	c_1
0.09	0.31	1.0	10.0

In the transport equations shown above, F_1 and F_{23} are blending factors used to merge the $k - \epsilon$ and $k - \omega$ models into a single model.

While a transient time scheme was used, transient flow features were not a primary focus of the work. To reach a steady state solution in time, a first order, implicit time scheme was applied, called the *Euler* scheme in OF, although higher order schemes are available [38]. In rCF, a flux limiter is required to resolve the sharp gradients that are present in the shock structures. The vanLeer flux limiting scheme is applied in the present work since it is *total variation diminishing* (TVD), preventing non-physical oscillations from appearing downstream of shocks. Other flux limiters are valid, such as the *minmod* limiter, provided they meet the TVD criteria [38]. The Courant number was set to 0.5 to maintain stability.

2.1.4 Boundary Conditions

2.1.4.1 Free Jet

To generate the under-expanded nozzle flow at a specific NPR, the pressures must be specified at the inlet and outlets of the domain, with no mass flow conditions being applied. In OF, the total pressure boundary condition applies a dynamic pressure value that includes the velocity at the boundary (Eq. 2.9).

$$P_p = P_0 - \frac{1}{2} |u^2| \quad 2.9$$

$$T_p = \frac{T_0}{1 + \frac{\gamma-1}{2\gamma} \psi |u^2|} \quad 2.10$$

Where P_p and T_p are the pressure and temperature at a boundary patch. A complete list of the boundary conditions applied is shown in Table 2.1:

Table 2.1: Boundary Conditions used for Under-Expanded Free Jet

Boundary	P	U	T
Inlet	totalPressure	zeroGradient	totalTemperature
Inlet Freestream 1	totalPressure	zeroGradient	totalTemperature
Inlet Freestream 2	totalPressure	zeroGradient	totalTemperature
Outlet	totalPressure	zeroGradient	zeroGradient
Wall	zeroGradient	noSlip	zeroGradient

Total temperature is applied in the same way as total pressure, where the actual temperature applied is dependant on the flow velocity at the boundary (Eq. 2.10). While all inlet and outlet boundaries must have a pressure boundary applied, the total temperature is only applied to patches where the air enters the domain. Without the application of total temperature on the domains where inflow occurs, the solver is unable to apply a temperature to fluid entering from these boundaries.

Pressure oscillations that appear in the domain must be damped out as they approach the boundary in order to prevent waves from reflecting back into the domain to interact with the under-expanded jet at the nozzle exit. The mesh spacing near the boundaries was increased in size enough that they were equal or larger than the wavelength of any oscillations present. By using an element size that is equal to or larger

than the wavelength of the oscillation, the pressure waves are unable to be resolved, causing them to dissipate before reaching the boundary [40]. Since the exact wavelength of any acoustic waves that might appear is unknown, a very large element size of 0.2d was applied. This method allows the total pressure boundary conditions to be applied at the outlets.

Using the k - ω SST turbulence model requires values for the turbulent kinetic energy (k), specific turbulent dissipation rate (ω), turbulent viscosity (μ_t), and turbulent thermal diffusivity (α_t) to be applied at the boundaries. The turbulent kinetic energy at the inlet can be set using the equation below (Eq. 2.11).

$$k = \frac{3}{2}(I|U_{ref}|)^2 \quad 2.11$$

U_{ref} is the average velocity at the inlet, and I is the turbulent intensity, specified as a percentage of U_{ref} . Typically the turbulent intensity is specified between 1% and 5%, depending on the degree of turbulence in the flow. For the nozzle being modelled, a Reynolds number of 33,100 was experienced inside the pipe leading to the nozzle, which is greatly in excess of $Re=4,000$ needed for turbulent flow. The turbulent intensity was specified at 3.8% at the nozzle inlet. For the turbulent dissipation, OF specifies the inlet condition using the following equation (Eq. 2.12).

$$\omega = \frac{k^{0.5}}{C_\mu L} \quad 2.12$$

Where in OF: $C_\mu = 0.09$ & $L = 0.07d_h$

2.1.4.2 Impinging Jet

Similar to the under-expanded free jet case, the boundaries specified in the impinging case use total pressure and total temperature to specify the conditions through the domain. The “Outlet” and “Inlet Freestream” use the larger grid spacing to damp out any acoustic waves that appeared in the domain. Only one outlet and one entrained flow inlet was present in the impingement case setup (Table 2.2).

Table 2.2: Boundary Conditions used for Under-Expanded Impinging Jet

Boundary	P	U	T
Inlet	totalPressure	zeroGradient	totalTemperature
Inlet Freestream	totalPressure	zeroGradient	totalTemperature
Outlet	totalPressure	zeroGradient	zeroGradient
Wall	zeroGradient	noSlip	zeroGradient

The turbulence model was the same one used in the under-expanded free jet case, and all boundary conditions applied remained the same.

2.1.5 Domain Initialization

Pointwise, a commercially available mesh generation software was used to generate the mesh of the fluid domain for each of the cases run. The domain shown in Figure 2.8 was generated using quadrilateral grid elements. Local grid refinement was applied in the nozzle throat, the shear layer, and boundary layer to provide better resolution in those regions, with mesh coarsening near the boundaries. Further, the boundary conditions specified created large pressure oscillations within the nozzle when the case started up from a non-initialized condition. These pressure oscillations reflected back and forth within the interior of the nozzle, causing oscillations in the mass flow through the inlet. These slowly decayed over time, and eventually a constant pressure and mass flow at the inlet were approached. The simulation was considered converged with time when no more than a 1% oscillation in mass flow from the mean value was observed (Figure 2.5).

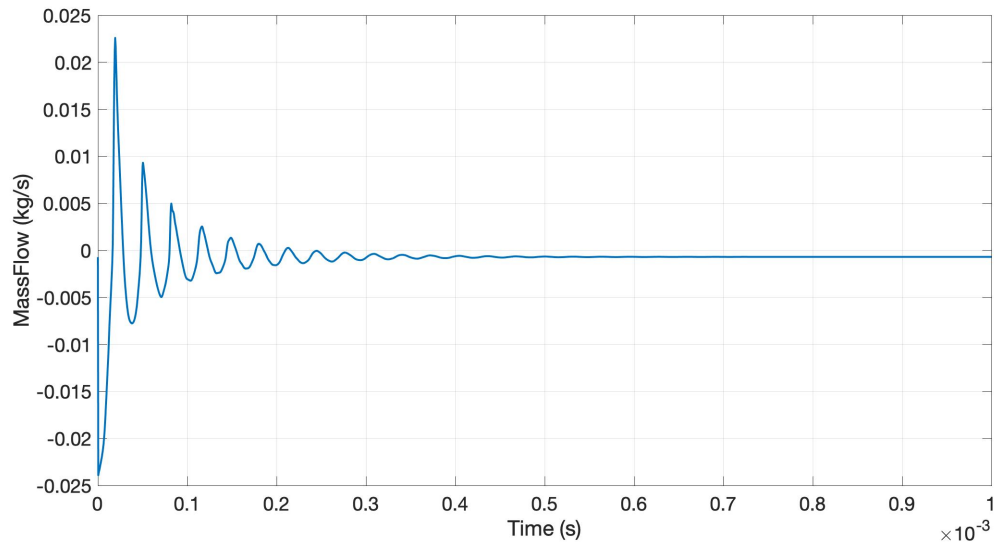


Figure 2.5: Mass Flow into the Nozzle when Started from Non-Initialized Condition

2.2 Results

Several steps were taken to ensure the quality of the results in the analysis of the free and impinging jets. First, a grid independence study was conducted to ensure the mesh was not impacting the results. Next, several key features of the under-expanded free jet are compared to results provided in Henderson et al. [10]. Features that are not fully described by Henderson, such as the growth of the shear layer and total length of the supersonic core are compared to other studies to determine whether they are within the expected range. Next, the impingement case was explored, where the recirculation bubble and position of the impingement shock were the primary features of interest. The presence of acoustic waves were expected to be suppressed by the turbulence model and therefore not explored. Further, the method of damping out pressure oscillations near the boundaries boundary will be reviewed, since a boundary condition for allowing pressure oscillations is available in the program.

2.2.1 WaveTransmissive Boundary Condition

The “waveTransmissive” boundary condition in OF, is meant to enable pressure oscillations to exit the domain, without any consideration of grid spacing.

“WaveTransmissive” uses a value called “farField”, and “lInf” where farField indicates

the pressure far from the boundary of the domain and “lInf” is the distance from a given patch to the “farField”. If a value of 0.0 was provided for lInf, the pressure provided for “farField” is directly applied to the boundary resulting in the boundary behaving like a fixed pressure boundary. When “waveTransmissive” was applied to multiple boundary faces (such as “Inlet Freestream 1” and “Inlet Freestream 2”) in the domain, with a non-zero “lInf” value, the pressure on different patches would drift away from the “farField” values specified. This resulted in a non-physically realistic pressure gradient being formed between boundaries, and an induced flow across these boundaries. The flow was commonly in the reverse direction to the free jet, and was large enough to cause the jet to reverse in direction. While Zang et al. [8], [28] reported on a working case setup for a similar flow with the waveTransmissive boundary condition, those results were unable to be recreated in this study.

2.2.2 Grid Convergence

2.2.2.1 Free Jet

The mesh independence study ensured the refinement of the mesh did not have a significant influence on the results. An initial coarse mesh was generated with 12,064 grid elements, and each subsequently refined mesh used 42.8% more grid elements than the previous (corresponding to $1/0.7$). A total of five meshes were generated with increasing grid density (Table 2.3) for the independence study. The first wall element thickness was reduced for each case by 19.5% as the number of grid elements increased (corresponding to $1/\sqrt{0.7}$). To reduce the computational cost associated with running each mesh from an uninitialized state, Level 1 was run first and the converged results were mapped to Level 2, and so on. This enabled a nearly steady-state condition to be the starting point for the subsequent test, reducing the wall-clock time needed to be simulated for each case.

Table 2.3: Mesh Characteristics for Under-Expanded Free Jet Grid Convergence Study

Refinement Level	Grid Elements	n/d	Wall Element Thickness	Sonic Core Length	Percent Change
Level 1	12,064	24	68.6 μm	11.30	-
Level 2	17,388	28	57.4 μm	11.56	2.3%
Level 3	24,841	30	48.0 μm	11.62	0.5%
Level 4	35,487	40	40.2 μm	11.83	1.8%
Level 5	50,695	43	33.7 μm	11.84	0.1%

To determine grid independence, the length of the super-sonic core was used as the variable of interest. This feature was characterised as the dimensionless distance downstream from the nozzle exit that was required for the velocity of the jet along the centre axis to decelerate below Mach 1. It was chosen as the variable of interest since it is largely dependant on the diffusion of momentum from the jet core into the shear layer, requiring the shear region to be properly resolved. Features upstream in the jet core, such as the first Mach diamond length are far less impacted by momentum transfer, since the thin shear layer in this region is very thin. Therefore, when the total length of the super-sonic core is independent of the grid refinement, all other features of interest are assumed to also be converged. Once the percent change in this variable fell below 1%, the grid was considered fully converged (Table 2.3). Convergence appeared to occur when the grid reached 24,841 elements, however further inspection revealed a large change when the grid was increased again to 35,487 elements (Figure 2.6). The sonic core length was independent of the grid refinement when the number of elements met or exceeded 35,487.

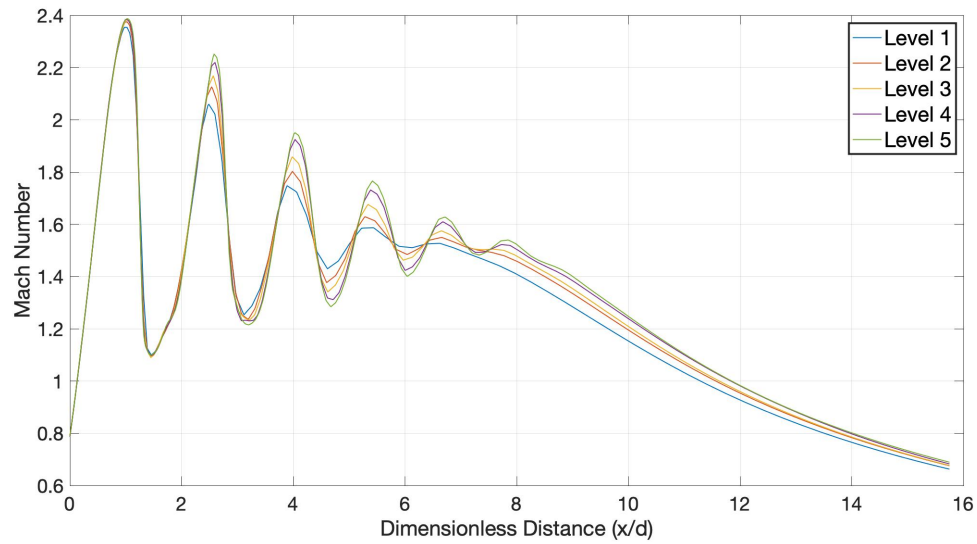


Figure 2.6: Mach Number vs. Dimensionless Downstream Distance from Nozzle

2.2.2.2 Impinging Jet

Grid convergence was conducted again for the impinging case to ensure the new flow features introduced were also independent of the grid. A highly refined quadrilateral grid was generated in the nozzle and impingement zone (Figure 2.8), while a coarser mesh was generated around this region. The refined quadrilateral mesh extended from the nozzle outlet to the impingement plate, and extended $5d$ radially outward (Figure 2.7). Surrounding this zone was the coarse hybrid mesh containing a mixture of quadrilateral and hexahedral elements. Hybrid meshes were generated using the advancing front orthogonal algorithm available in Pointwise, that creates high quality mesh elements resembling structured meshes by limiting the number of tetrahedral elements and maintaining low aspect ratios of all hexahedral elements.

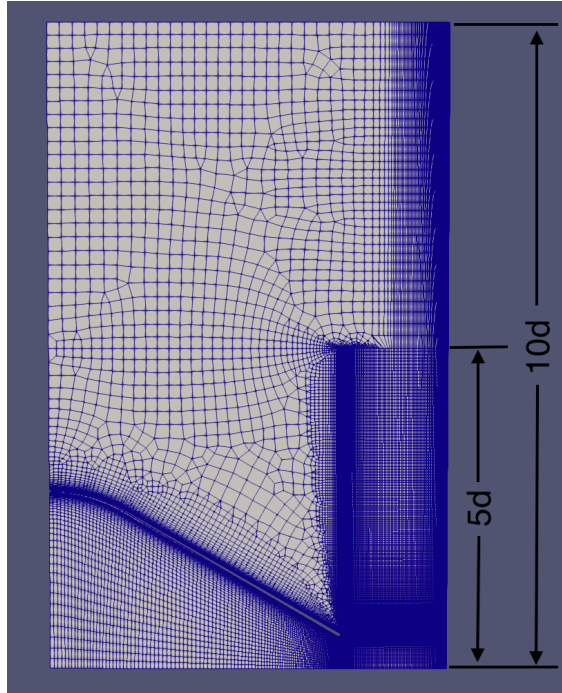


Figure 2.7: Mesh Used for the Impingement Jet Domain

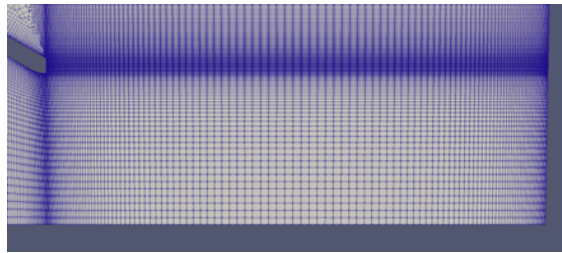


Figure 2.8: Mesh Used in the Refined Impingement Jet Region

Since the impingement shock and recirculation bubble present impinging jet cases are both very important features, the mesh is most refined at the nozzle exit and along the impingement plate (Figure 2.8). The main features intended to be resolved include the shock structure, shear region, impingement shock, and recirculation bubble. An initial grid convergence study used the same refinement strategy as the free jet, where each subsequent test increased the number of mesh elements by 42.8%. The recirculation bubble was unable to be resolved after several iterations of refinement. To ensure that the suppression of the recirculation bubble was not a result of poor mesh quality, a second study was run where number of grid elements in each subsequent study was doubled. This enabled very refined meshes to be obtained in fewer iterations, and is the mesh

independence study reported on. When looking at Table 2.4, it may be noticed that the total number of grid elements does not double between each level of refinement. This is due to the coarse mesh near the boundaries not being refined between each case, since refining these cells would result in pressure waves being resolved and reflected back into the domain. Therefore, in each refinement iteration, the number of elements in the quadrilateral region was doubled while the hybrid region remains constant. The recirculation bubble was unable to be resolved at any refinement level, so the grid density required for the free jet case was used in the impinging jet cases. Thus, the level 4 grid refinement was selected as the grid independent mesh.

Table 2.4: Mesh Characteristics for Under-Expanded Free Jet Grid Convergence Study

Refinement Level	Grid Elements	n/d	Wall Element Thickness	Recirculation Bubble
Level 1	11,168	14	114.0 μm	No
Level 2	17,795	20	100.0 μm	No
Level 3	30,326	24	71.0 μm	No
Level 4	57,974	34	50.0 μm	No
Level 5	113240	54	35.0 μm	No

2.2.3 First Mach Diamond

The velocity profile along the centre axis of the free jet model can be directly compared with the experimental results obtained by Henderson et al. [10] through the first three Mach diamonds. The first Mach diamond length, shown for the numerical case in Figure 2.9, is defined by the length from the nozzle exit to the first narrow section of the super-sonic core. Henderson found this value to be 1.6d (40.6mm), while the numerical results obtained 1.65d (42.0mm), thus over-predicting the length by 3.1%. Zang et al. [8] similarly found a 4.0% over-prediction of the first Mach diamond length while using rCF with the $k - \omega$ SST turbulence model.

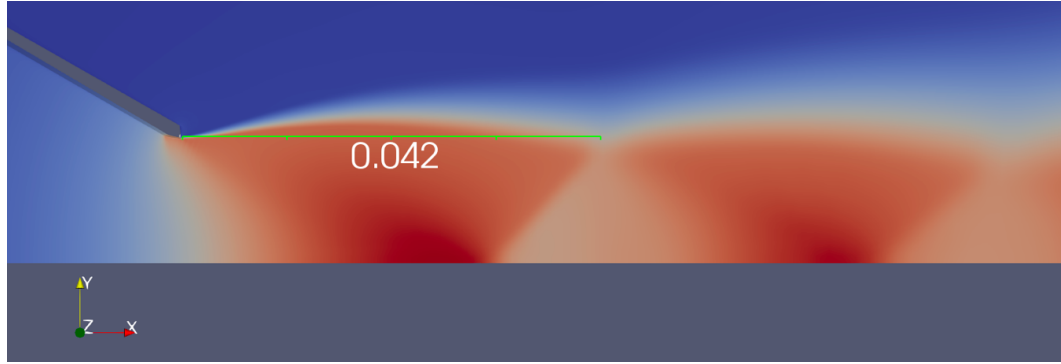


Figure 2.9: Length of the First Mach Diamond Predicted by the Numerical Model (m)

From Figure 2.10, it can be seen that the velocity profile along the centre core in the numerical results consistently over-predicted the experimental profile. Over-prediction of the velocity is more substantial after the first Mach diamond, and is likely the result of some losses not being accounted for in the numerical model. The most likely source is the presence of a small Mach disk in the experimental case that is not captured numerically. Since stream lines that pass through the Mach disk experience a greater increase in entropy than the stream lines that pass through the exterior oblique shocks, failure to capture this feature would reduce the losses in the jet. With only one Mach disk occurring in the first Mach diamond, this loss provides an explanation for sudden drop in flow velocity found in subsequent Mach diamonds. Dauplain et al. [7] resolved a Mach disk in the first Mach diamond using an LES turbulence model, and subsequently showed very close agreement with the velocity profile in the second Mach diamond. Further, Hamzehloo et al. [29] found the same phenomenon when comparing LES and $k - \omega$ SST models. In that study, the Mach diamond was captured when using LES, and suppressed by $k - \omega$ SST, resulting in a similar over-prediction in the flow velocity when using the $k - \omega$ SST model. This provides a strong case that the Mach disk is the source of the discrepancy between the experimental and numerical results obtained, and the $k - \omega$ SST model is unable to properly resolve this flow feature at the NPR tested. The DPIV technique used by Henderson et al. [10] to experimentally capture the velocity profile does not indicate the presence of a small sub-sonic region that is characteristic of Mach

disks. However, the inertia of the oil drops used for this technique may mask the phenomenon [10].

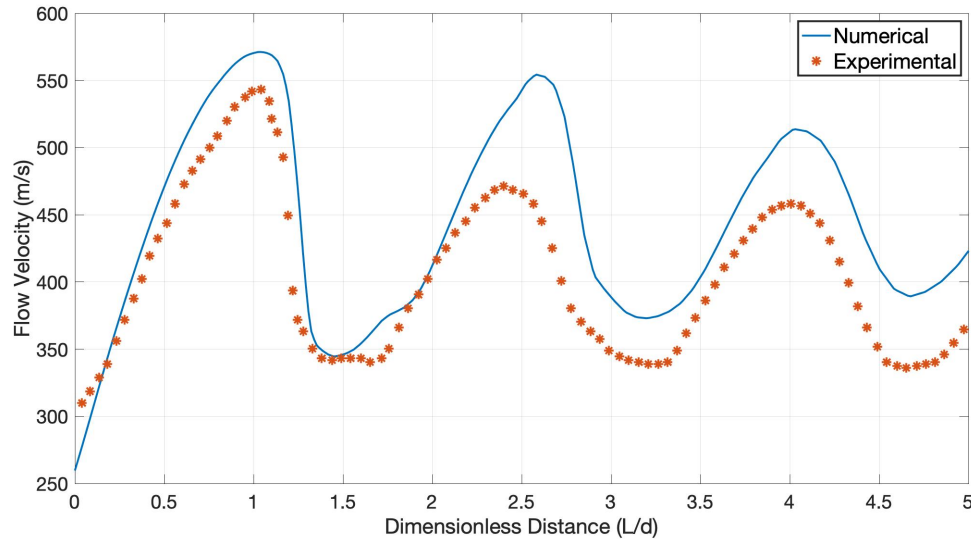


Figure 2.10: Flow Velocity Along the Central Jet Axis for the Numerical and Experimental Studies [10]

2.2.4 Super-Sonic Core

Although the length of the super-sonic core was not directly measured from Henderson's experiment, other sources can be used to approximate the length of this region. Using the equation determined by Phalnikar et al. [9] an estimate for the length of this feature can be found using the NPR. At a NPR of 4.00, the estimated length of the super-sonic core is approximately $10.10d$, which is less than the numerical result of $11.83d$ (Table 2.3). However, the model equation was developed for a nozzle diameter in the $400\mu\text{m}$ range and tends to underpredict the length of the core of large nozzle diameters. Phalnikar's conclusion that the core of the jet extends further when experimenting with larger diameter nozzles disagrees with most of the research currently available [9]. As the Reynolds number decreases with the nozzle diameter the transfer of momentum to the shear layer is reduced, which should result in a longer super-sonic core for smaller diameter nozzles.

2.2.5 Shear Layer Growth

The final characteristic of interest is the linear growth angle of the shear layer. This region was quantified using Dauptain's characteristic, which is defined as the region where the flow velocity is between 50-300m/s. An angle was obtained based of the growth rate of the 50m/s stream line. This region was both experimentally and numerically determined by Dauptain et al. [7] and since the results were generated by a similar nozzle to the one used by Henderson et al. [10] they were a good basis for comparison. Dauptain et al. provide the velocity data for the under-expanded impinging jet case where the impingement plate was located 4.16d downstream of the nozzle exit.

Table 2.5: Shear Layer Growth Angle for Experimental, LES, and RANS Studies

Study	NPR	Growth Angle	Difference
Dauptain Experimental	4.03	5.0°	-
Dauptain LES	4.03	6.6°	32%
Current Study $k - \omega$ SST	4.00	6.2°	24%

The experimental and numerical results provided in Table 2.5 are time averaged values, and show that the $k-\omega$ SST model actually provides closer agreement with the experimental results than LES. Since Dauptain's study was observing the shear layer growth of an impinging jet, while the present study looked at a free jet, it must be confirmed that the growth of the shear layer is not dependant on the presence of the impingement plate. The shear layer growth of both the impinging and free jet case in the present study were compared, and it was found that they have identical growth rates of 6.2°, at a downstream distance between 0.5d and 3.5d.

2.2.6 Recirculation Bubble

The most notable result from the numerical study is the lack of a recirculation bubble in the impingement region. After the flow passes through the impingement shock, it is gradually decelerated further and redirected to flow radially outward (Figure 1.5). It is not certain which assumption in the model used is responsible for supressing this flow feature, although it is likely to either be the axisymmetric assumption, $k-\omega$ SST turbulence model, or the convection scheme used. As shown by Donaldson et al., the

recirculation bubble contains some 3-dimensional flow features that are not included in the axisymmetric model, yet Kim et al. [27] was able to capture the bubble using an axisymmetric model. Chun et al. [41] showed that some convection schemes can overcorrect in impingement regions, which may suppress the recirculation bubble from forming. The axisymmetric assumption is the most likely candidate for why this feature was suppressed,

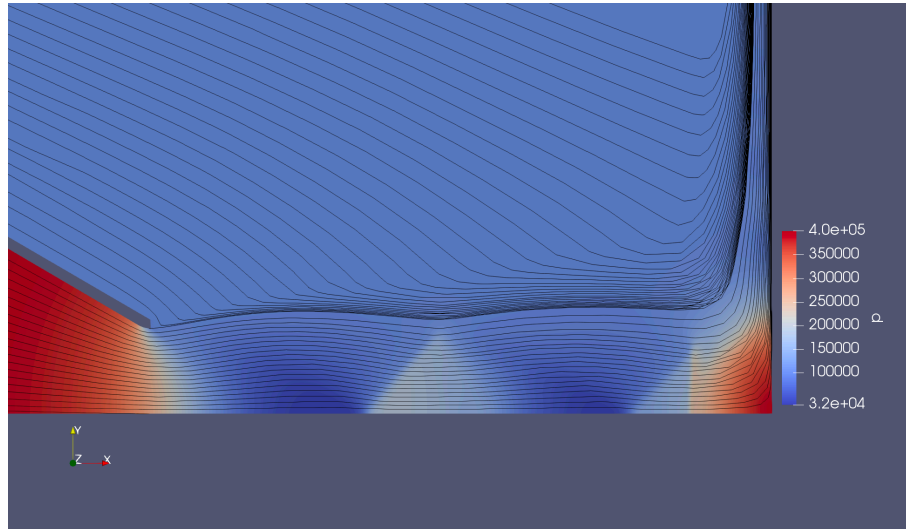


Figure 2.11: Streamlines for Impinging Jet Case $L/d=3.65$, with Pressure Contour Background

2.2.7 Impingement Shock

The next feature of interest is the impingement shock preceding the impingement plate. This feature is caused by the sudden deceleration of the flow as it impacts the stationary plate. The position of the impingement shock for each case is compared to the experimental case found by Henderson et al. [10]. A secondary validation of the shock behaviour is then performed by measuring the change in flow properties across each shock and comparing them with the expected theoretical changes. This is conducted by looking at the upstream and downstream Mach number, and the downstream stagnation pressure as predicted by Eq. 1.7 and Eq. 1.8.

Since the turbulence model used suppresses any instabilities or coherent structures in the shear layer, the acoustic phenomena associated with them will also be suppressed.

This resulted in no transient features being present once steady state is reached, and thus a fixed location for the impingement shock. The impingement shock position from Henderson et al. [10] is taken from the time-averaged velocity profile, and therefore the time-averaged impingement shock position. The numerical and experimental results along the central axis are compared in Figure 2.12, where each colour represents a specific nozzle to plate spacing, the dashed lines are experimental results, and the solid lines are numerical results.

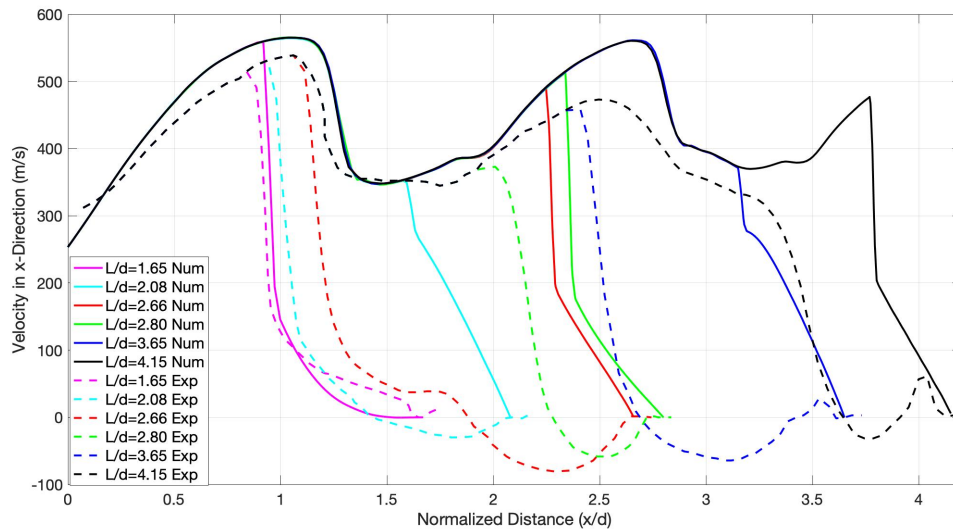


Figure 2.12: Velocity Profile Along Jet Axis for an Impinging Jet at Various Distances from the Impingement Plate, Dashed Lines – Experimental [10], Solid Lines – Present Numerical Study

It is clear from Figure 2.12 that the numerical location of the impingement shock is predicted closer to the impingement plate for every case except $L/d=1.65$. For all other cases, the numerical impingement shock is located between $0.34d$ and $1.09d$ downstream of the experimental impingement shock (Table 2.6). Part of this discrepancy can be accounted for by the presence of the recirculation bubble. If the contact surface produced by the recirculation bubble is considered to behave like the impingement plate, then the location of zero-velocity will be moved upstream from the impingement plate (Figure 1.5). When the position of the contact surface was accounted for, the subsequent error in the impingement shock position was greatly reduced (Table 2.7). It is worth noting that

the recirculation bubble was not present experimentally when $L/d = 1.65$, and the impingement shock location was most accurately predicted. While Table 2.7 indicates that the recirculation bubble accounted for a substantial portion of the error found in impingement shock location, other sources of error are still present. For the case where $L/d = 2.60$, the impingement shock error is at its maximum of $-0.38d$. Since heat transfer at the impingement point has been shown to be a function of the recirculation bubble [12], this model would not likely be suitable for some heat transfer estimations.

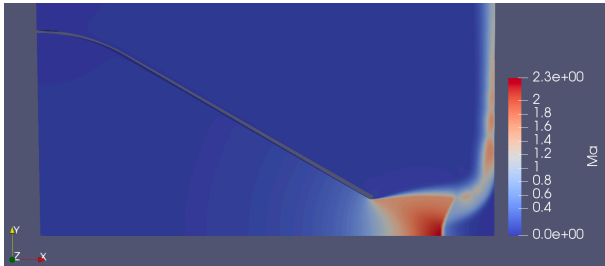


Figure 2.13: Mach Contour of $L/d=1.65$

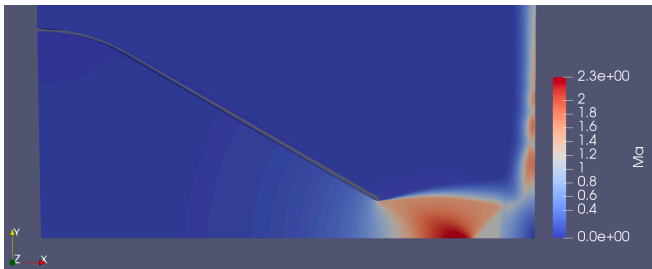


Figure 2.14: Mach Contour of $L/d=2.08$

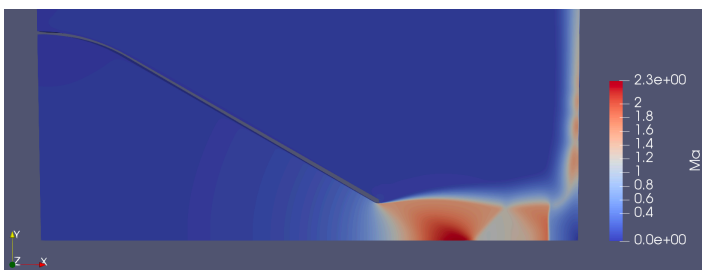


Figure 2.15: Mach Contour of $L/d=2.66$

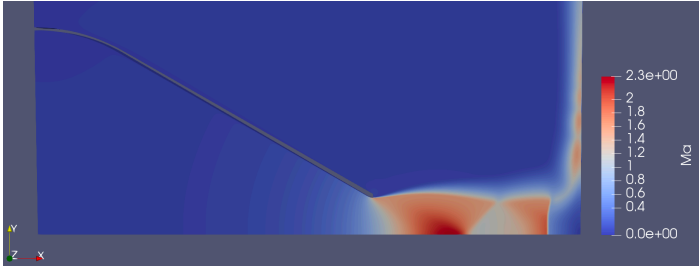


Figure 2.16: Mach Contour of L/d=2.80

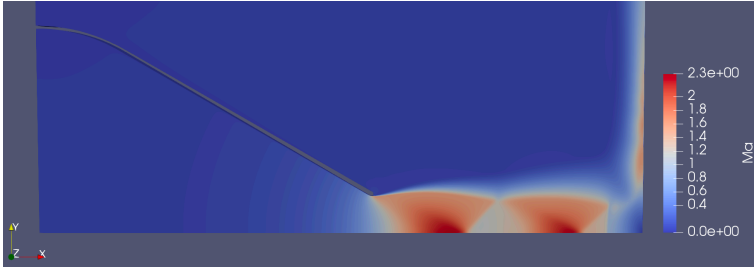


Figure 2.17: Mach Contour of L/d=3.65

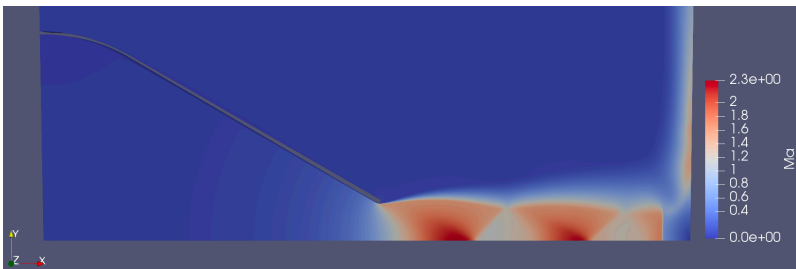


Figure 2.18: Mach Contour of L/d=4.16

Table 2.6: Dimensionless Impingement Shock Position Downstream from Nozzle

Case	Experimental Shock Position (x/d)	Numerical Shock Position (x/d)	Difference
L/d = 1.65	0.85	0.91	0.06
L/d = 2.08	0.95	1.59	0.64
L/d = 2.66	1.15	2.24	1.09
L/d = 2.88	2.00	2.34	0.34
L/d = 3.65	2.40	3.15	0.75
L/d = 4.16	3.25	2.77	0.52

Table 2.7: Dimensionless Impingement Shock Position Downstream from Nozzle, Corrected for Contact Surface

Case	Experimental Shock Position (x/d)	Numerical Shock Position (x/d)	Contact Surface Position (x/d)	Difference - Corrected for Contact Surface
L/d = 1.65	0.85	0.91	1.65	-0.06
L/d = 2.08	0.95	1.59	1.41	0.03
L/d = 2.66	1.15	2.24	1.89	-0.38
L/d = 2.88	2.00	2.34	2.28	0.26
L/d = 3.65	2.40	3.15	2.67	0.23
L/d = 4.16	3.25	2.77	3.62	0.02

2.2.8 Theoretically Predicted Shock

The behaviour of a compressible fluid as it crosses the normal shock is well documented, and can be calculated using Eq. 1.7 and Eq. 1.8. The decrease in Mach number can be numerically determined by measuring the Mach number before and after normal shock (Table 2.8) For all cases except L/d = 3.65, the error in the numerically determined Mach number is within 10% of the theoretical results. The change in Mach number across the shock is difficult to accurately resolve numerically given how thin the normal shock is relative to the grid element size. The stagnation pressure downstream of the mach number is more accurately resolved, with the greatest error found at 3.3% (Table 2.9). Interestingly, the numerical stagnation pressure always underpredicted the theoretical values, indicating some additional losses in the numerical results. The error of each property of interest was computed as, $error = \frac{abs(\phi_{theo} - \phi_{numerical})}{\phi_{theo}}$, where ϕ represents any property of interest.

Table 2.8: Numerical and Theoretical Mach Number Across the Impingement Shock

Case	Upstream Mach Number	Downstream Mach Number	Theoretical Downstream Mach Number	Error
L/d = 1.65	2.29	0.57	0.54	5.7%
L/d = 2.08	1.13	0.84	0.89	5.3%
L/d = 2.60	1.79	0.57	0.62	8.7%
L/d = 2.88	1.95	0.51	0.59	12.5%
L/d = 3.65	1.21	0.85	0.84	1.2%
L/d = 4.16	1.72	0.59	0.63	6.6%

Table 2.9: Numerical and Theoretical Stagnation Pressure Across the Impingement Shock

Case	Upstream Mach Number	Upstream P_0 (kPa)	Downstream P_0 (kPa)	Theoretical Downstream P_0 (kPa)	Error
L/d = 1.65	2.29	400	235.4	236.0	0.2%
L/d = 2.08	1.13	400	396.4	399.1	0.7%
L/d = 2.60	1.79	400	316.6	327.5	3.3%
L/d = 2.88	1.95	400	290.0	298.1	2.7%
L/d = 3.65	1.21	400	395.4	296.7	0.3%
L/d = 4.16	1.72	400	333.8	338.6	1.4%

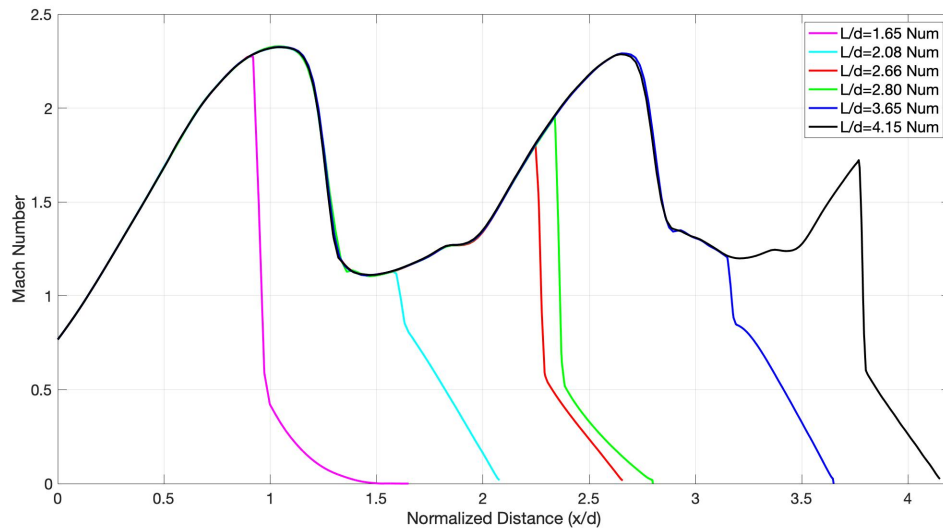


Figure 2.19: Mach Number Along Central Axis For each Nozzle to Plate Spacing

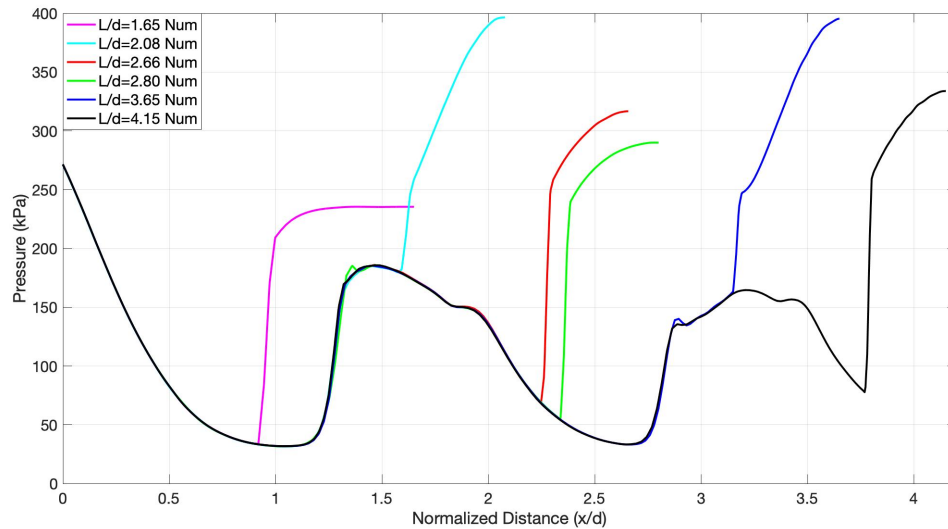


Figure 2.20: Pressure Along Central Axis For each Nozzle to Plate Spacing

2.3 Summary

The work in this chapter was specifically completed with the intent to validate an axisymmetric numerical model using rCF and the $k-\omega$ SST turbulence model for use on under-expanded free and impinging jets with a NPR of 4.0. The numerical results obtained were compared against a well documented previous experimental study conducted by Henderson et al. [10]. For the free jet, the length of the first Mach diamond along with the length of the super-sonic core was accurately predicted. The growth rate of the shear layer was slightly overpredicted by the $k-\omega$ SST model, but was more accurate than LES model as reported by Dauplain et al. [7]. All of the coherent structures that form within the shear layer were suppressed, either by the axisymmetric assumption, or the $k-\omega$ SST model. For the impingement cases, the recirculation bubble was found to be suppressed. Although the mechanism for this is still unknown, it is thought to be either the axisymmetric assumption, the turbulence model, or the convection scheme used. With the recirculation bubble being suppressed, the location of the impingement shock was found to exist closer to the impingement plate than observed experimentally. Further, heat transfer at the plate may have some error introduced by the removal of the recirculation bubble. Since the $k-\omega$ SST model suppresses any coherent structures in the shear layer, the feedback mechanism required for the characteristic acoustic phenomenon

is suppressed. Therefore, while running a transient simulation, the impinging jet will reach a steady state condition that is not found experimentally. Thus, for applications where the acoustic features, heat transfer, or coherent turbulent structures are not required, the model developed in this chapter is deemed sufficient. With the capabilities and limitations of the low cost numerical model evaluated, it will now be applied to the geometry of interest to gain value insight into the fluid behaviour within the device.

Chapter 3

3 Single-Phase Nebulizer Modelling

With an understanding of how rCF functions for an idealized under-expanded impinging jet, it can be applied to the application of interest. The nebulizer has a similar geometry to the one used by Henderson et al. [10] (Table 3.6), with a NPR in the moderately under-expanded region and a similar dimensionless nozzle to plate spacing. New to the nebulizer geometry is the presence of a confining wall parallel to the impingement plate near the nozzle exit. This feature generates an additional toroidal vortex that produces a low-pressure region used by the device, and will be explored in this chapter.

3.1 Methods

3.1.1 Nebulizer Domain

Shown in Figure 3.1, the nozzle inlet is a constant diameter pipe followed by a sudden contraction to a smaller diameter hole. As air passes through the sudden contraction it becomes choked flow before reaching the nozzle exit. Between the contraction and nozzle exit, the nozzle has a slightly diverging draft angle, which enables the flow to expand further, accelerating it to super-sonic velocities. Downstream from the nozzle exit is a baffle where the flow impinges and is redirected radially outward. The device is designed to have a nominal nozzle diameter of $d=0.56\text{mm}$ and a nozzle to plate spacing of 1.39mm , which yields a dimensionless nozzle to plate spacing of $2.48d$. While the diameter of the designed nozzle is approximately 45 times smaller than the one used by Henderson et al. [10], the dimensionless nozzle to plate spacing is within the range tested. The baffle used on the nebulizer is 1.76mm in diameter or $3.14d$, resulting in a much smaller dimensionless baffle size when compared to the one studied by Henderson et al. [10]. At that nozzle diameter, the jet Reynolds number is approximately 13,000, which exceeds the Reynolds number of 10,000 required for fully-turbulent jet flow [2]. As is characteristic of confined impinging jets, the flow downstream of the baffle is drawn into a rapidly spinning low pressure toroidal vortex that surrounds the jet, bounded

by the baffle and liquid channel proudness (Figure 3.2). A smaller secondary vortex was found to appear between the under-expanded jet and the main toroidal vortex, and rotates counter, to the main toroid. The low-pressure toroidal vortex generates a small vacuum pressure between the under-expanded jet and the toroidal vortex. The vacuum propagates into the liquid channel, drawing liquid drug into the free jet where it breaks up into small droplets within the respirable range ($1-5\mu\text{m}$) (Figure 3.2). Four key geometric parameters have been outlined in Figure 3.1, and their impact on the strength of the vacuum pressure inside the liquid channel will be explored. These parameters are: the draft angle (A), the nozzle diameter (B), the nozzle to baffle distance (C), and the proudness of the liquid channel (D) (Figure 3.1). The draft angle represents the diverging angle of the nozzle between the sudden contraction and the nozzle outlet, and is a required feature for injection molding. The distance to the baffle is the length between the nozzle exit plane and the impingement baffle. The proudness is the distance above the nozzle exit plane in the axial direction, that the radially distant wall of liquid channel is elevated. A parametric study was conducted to determine the influence each of these parameters on the vacuum pressure, and their interactions with each other. This study is broken down into three key steps to ensure the final parametric study results are reliable:

1. Grid independence study
2. Vacuum pressure validation study
3. Parametric study

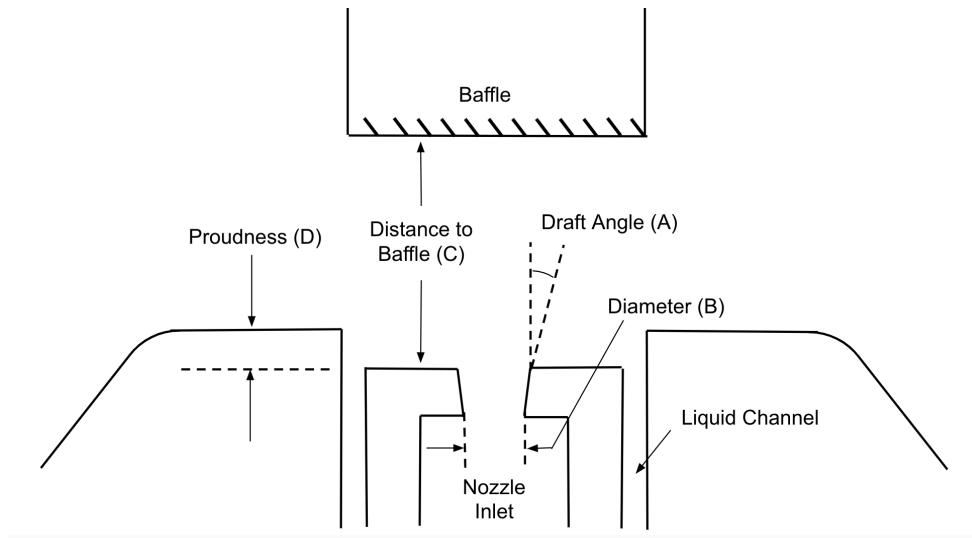


Figure 3.1: Nebulizer Geometry with the Geometric Features Explored in the Parametric Study Labeled

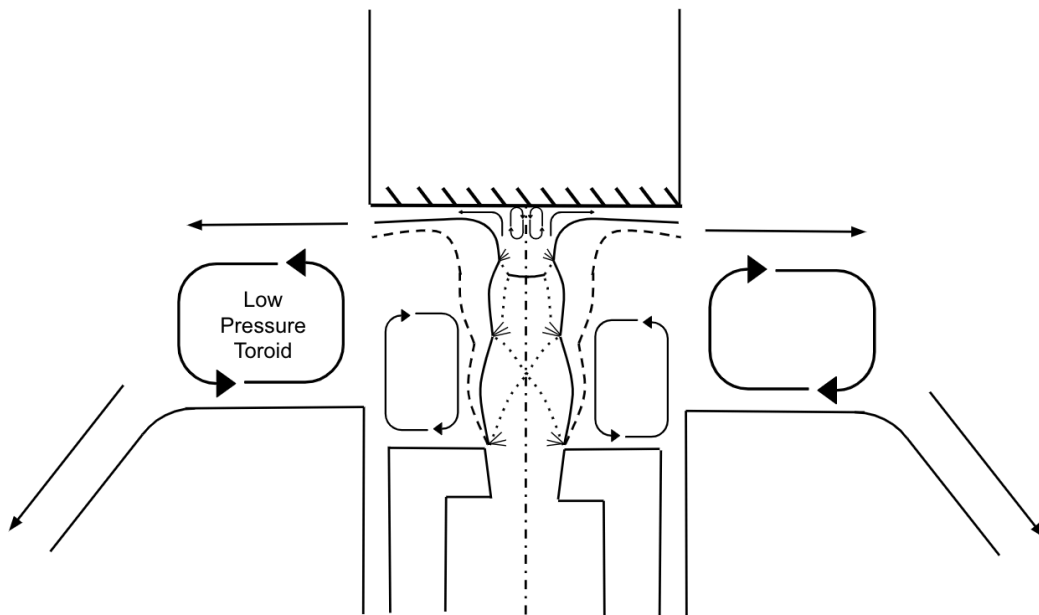


Figure 3.2: Flow Structure Inside the Nebulizer, Showing the Under-Expanded Impinging Jet, Followed by the Low Pressure Toroidal Vortex Downstream

3.1.2 Boundary Conditions

The boundary conditions used to supply the inlet of the nozzle were different than the conditions used for the earlier rCF validation case. In practice, the device is set to a manufacturer recommended volumetric flow rate by a medical professional or supplied by a portable compressor. These different air supply methods will be referred to as *wall air* and *compressor air* respectively. To keep the model consistent with the actual use conditions, a mass flow rate boundary condition was applied at the inlet in place of the total pressure boundary condition used in the previous chapter. The conditions applied to each of the boundaries is shown in Table 3.1. Wall air is supplied to the nozzle with a volumetric flow rate of 8.0 standard l/min. The OF mass flow boundary condition is called “flowRateVelocityInlet” and requires the mass flow to be specified in kilograms per second. The conversion between liters per minute to kg/s through a 5° wedge can be calculated as: $\dot{m} = fV$, where \dot{m} is the mass flow rate in kg/s, V is the volumetric flow rate in litres per minute, the conversion factor f is $2.8 * 10^{-7}$, calculated as:

$$\dot{m} = \dot{V} \left[\frac{L}{min} \right] * \frac{1}{1000} \left[\frac{m^3}{L} \right] * \frac{1}{60} \left[\frac{min}{s} \right] * \rho_{air} \left[\frac{kg}{m^3} \right] * \frac{5^\circ}{360^\circ}$$

$$f = \frac{1}{1000} \left[\frac{m^3}{L} \right] * \frac{1}{60} \left[\frac{min}{s} \right] * \rho_{air} \left[\frac{kg}{m^3} \right] * \frac{5^\circ}{360^\circ} = 2.8 * 10^{-7}$$

$$\text{where: } \rho_{air} = 1.225 \text{ kg/m}^3$$

Compressor air is given by a data sheet provided by the manufacturer, that shows the expected volumetric flow rate from the compressor for a given nozzle diameter. An average patient is expected to inhale air at a peak rate of approximately 15 l/min, which is drawn out of the “Outlet” boundary (Figure 3.3). The air inhaled by the patient is composed of air delivered from the nozzle and air vents positioned on the device upstream of the nozzle. Flow through the “Inlet_Inhale” boundary is used to make up the difference between what the nozzle supplies and the “Outlet” requires, averaging 7.0 l/min into the domain. Further, “Inlet_Inhale” uses a total pressure boundary condition to ensure the ambient pressure in the device is held at atmospheric pressure and temperature. On the radially distant face between the “Inlet_Inhale” and “Outlet”

boundaries, a wall boundary is applied since that is a wall in the nebulizer device (Figure 3.3). Pressure in the nozzle “Inlet” is extrapolated using the “zeroGradient” pressure condition, and will increase until the NPR required for the mass flow specified is achieved. The “Inlet_Liquid” is where the liquid drug is supplied from during patient use. However, in the single-phase model it does not have any air or liquid flow through it, and is used for measuring the pressure in the liquid channel. Since no flow is intended to cross this boundary face, the conditions applied are the same as a wall boundary.

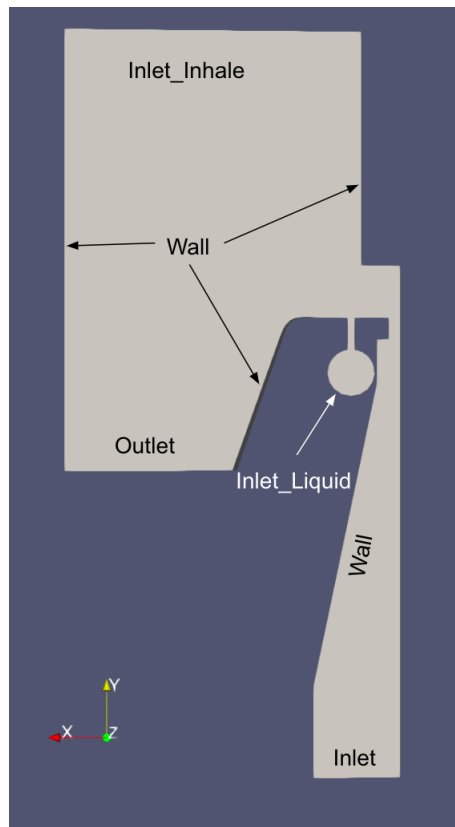


Figure 3.3: Fluid Geometry and Boundaries for Nebulizer Model

Table 3.1: Boundary Conditions used for Nebulizer Model

Boundary	P	U	T
Inlet	zeroGradient	massFlow	totalTemperature
Inlet Inhale	totalPressure	zeroGradient	totalTemperature
Inlet Liquid	zeroGradient	noSlip	zeroGradient
Outlet	zeroGradient	massFlow	zeroGradient
Wall	zeroGradient	noSlip	zeroGradient

The $k - \omega$ SST turbulence model from the previous chapter was carried over for this work. However, since the size of the domain was far smaller, the turbulent boundary conditions applied at the inlet needed to be tuned to ensure their validity. Air flowing into the nozzle enters from a 4mm diameter at approximately 5 m/s. Under these conditions the Reynolds number is around 1400, which is low enough for the flow to be laminar on its way into the nozzle. However, since upstream flow control apparatus are present, a small turbulent intensity of 1% was selected.

3.1.3 Mesh Generation

When manufacturing defects are taken out of consideration, the design of the nebulizer is axisymmetric, enabling the axisymmetric assumption to be applied. Since a parametric study with four factors was the intent of the present work, a total of 32 geometries/meshes were required (4^2 different geometries, each with a course and refined mesh). Each geometry/mesh required approximately three hours to generate, making the process time-consuming, tedious, and open to the possibility of error. Thus, to avoid this, a macro was written using the glyph scripting language provided in Pointwise to automate the process of creating high quality meshes. This not only reduced the time required to generate the geometries/ meshes for the cases under consideration, but also provided a tool to quickly explore other geometries within the parameter space.

By breaking down the domain of the nebulizer into several segments, each region could be meshed independently to ensure the desired local mesh properties could be obtained (Figure 3.4). Region 1 is the region of interest for this study, containing the under-expanded impinging jet and the toroidal vortex that forms. This region is meshed with quadrilateral mesh elements and has a very high degree of refinement (Table 3.2). Region 2 used the hybrid advancing front orthogonal algorithm to enable a refined mesh as the inlet approaches the sudden contraction in the nozzle. Region 3 surrounds the toroidal vortex and meshed using advancing front orthogonal. The mesh here is highly refined along the edges that border region 1, and grows as it moves toward the edges that border region 4. Region 4 is far coarser than the other regions and is used to damp out acoustic waves as they propagate toward the boundary of the domain. Finally, region 5 is also a coarse mesh at the end of the liquid channel, and is used to damp out acoustic

waves at the base of the liquid channel to prevent them from propagating back into region 1.

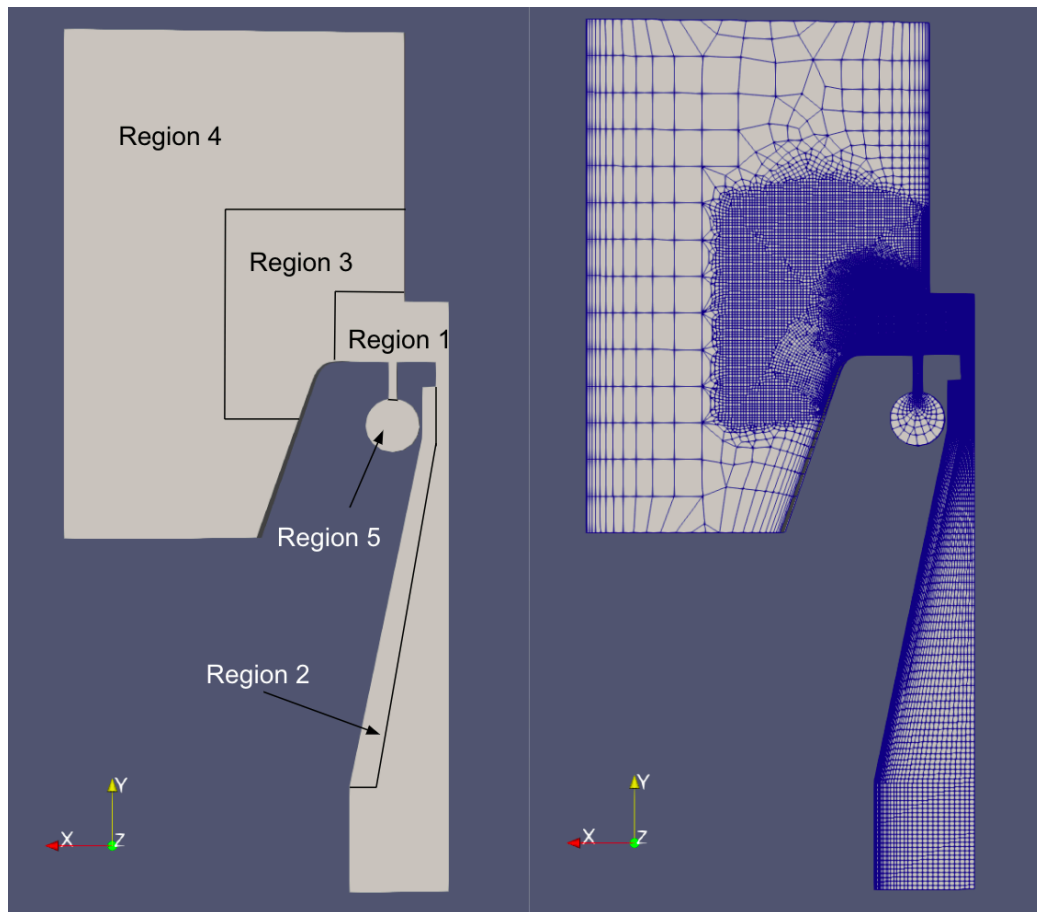


Figure 3.4: Meshing Regions used to Model the Nebulizer (Left) and Final Mesh Created by the Meshing Macro (Right)

Each region of the domain was generated sequentially from region 1 through 5, then the whole fluid domain was rotationally extruded by 5° about the axis of symmetry. At this point, the boundary conditions could be applied by hand, reducing the overall user input to under 5 minutes per mesh.

Generating the quadrilateral grid in region 1 was the most challenging to automate, since Pointwise requires each quadrilateral mesh to have four sides, with each opposing side having an equal number of divisions. For many of the meshes generated, this required 18 distinct rectangular segments to be modelled (Figure 3.5) and each side

of a segment to be properly dimensioned. Points were created in the domain for the vertex of each rectangular segment that were connected by lines. These lines were created by connecting any two neighboring points in either the X or Y direction. An algorithm designed for the purposes of this project was used to ensure only the neighboring points would be connected with a line, and that a line would not be generated between every set of points along the same X or Y direction. This was completed as follows.

1. Observe a point n (starting from point 1), label it *current point a*
2. Loop through all subsequent points and check if they are along the same X or Y axis, label this point *observed point b*
3. Check if a and b are actually neighbors, loop through each point again to check if any point lays between a and b , label it *check point c*. The check can be conducted using, $0 < \frac{a_i - c_i}{a_i - b_i} < 1$, where the subscript i indicates the axis X or Y.
4. If a and b are neighbors, connect them with a line
5. Return to step 1, observing the next point, $n+1$

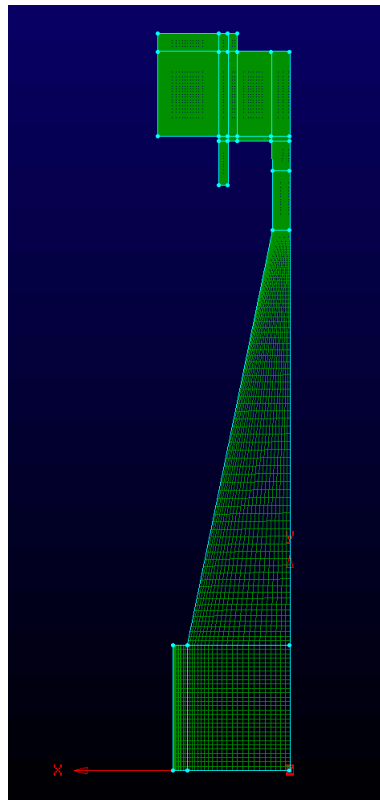


Figure 3.5: Region 1 Meshed using the Automated Pointwise Macro

Several lines in the domain are special cases since they connect two points that are not along the same X or Y direction, these lines are hardcoded into the macro. Using this process, the domain shown in Figure 3.5, and any structured domain that can be subdivided into orthogonal regions can be generated. The subsequent regions use the hybrid mesh, which can be generated without the need to divide the region into rectangular segments with matching opposing walls. The lines around the perimeter of the region are connected and the enclosed area is meshed. With regions 1 through 5 generated the domain will appear as shown in Figure 3.6. The macro can tune the value of the geometric parameters of interest and the grid density applied.

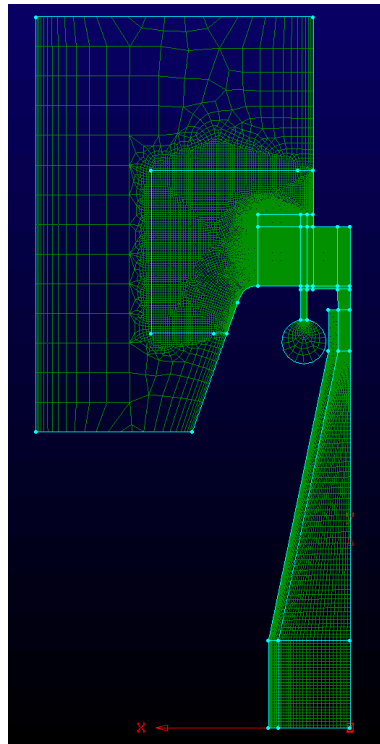


Figure 3.6: All Regions Meshed using the Automated Pointwise Macro

Local refinement in the domain was done primarily in region 1 and along the walls, where the density of the grid needed to be more refined. Within region 1, locally refining only the wall boundaries, without reducing the grid quality in the remainder of the region by skewing and stretching of elements was very challenging. Thus, a simpler computationally efficient method of local refinement was used. This method reduced the grid size to 60% of the average element size near any location along a wall or where

two segments met. This technique ensured the skewness and non-orthogonality of every element in region 1 was as low as possible, while the aspect ratio was held below 3.0 (Figure 3.8). The minimal level of refinement along the wall was chosen to ensure the grid density in the core of any rectangular segment was still sufficiently refined.

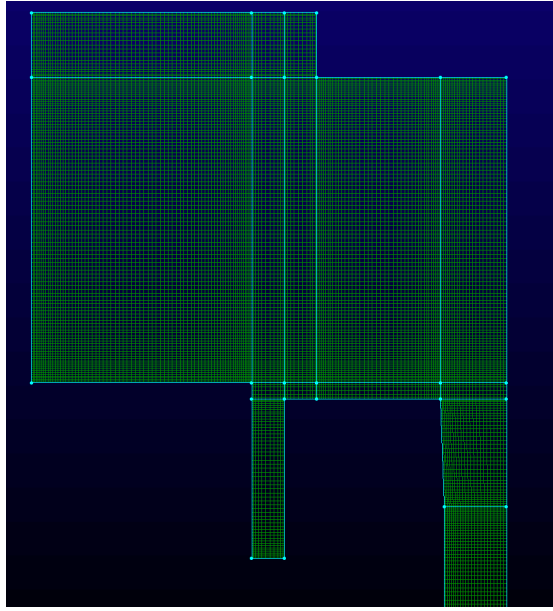


Figure 3.7: Densely Refined Portion of Region 1, used to Capture the Under-Expanded Impinging Jet, Toroidal Vortex, and Liquid Channel Features

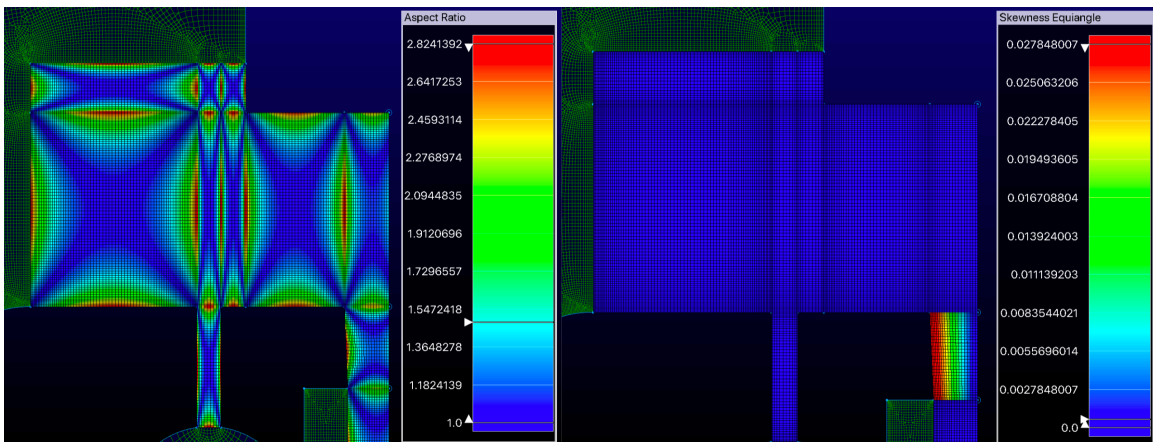


Figure 3.8: Mesh Aspect Ratio (Left) and Mesh Skewness (Right), in the Region of Interest for Case LLLH

Table 3.2: Mesh Regions used to make the Nebulizer Fluid Domain

Region	Element Type	Refinement Level
Region 1	Quadrilateral	Refined
Region 2	Adv. Front Orthogonal	Refined
Region 3	Adv. Front Orthogonal	Refined
Region 4	Adv. Front Orthogonal	Coarse
Region 5	Adv. Front Orthogonal	Coarse

3.1.4 Experimental Validation

Since the parameter of interest for the nebulizer, the vacuum pressure that extends into the liquid channel, was not explored in the previous chapter, the numerical results of the nebulizer should be validated against some experimental data. Given the model used is specific to the nebulizer, an in house experimental setup was developed to measure the liquid channel vacuum pressure directly.

Air was supplied to the nebulizer from a high-pressure reservoir and controlled by a flow control needle valve (Figure 3.9). The supply reservoir must be at a high enough pressure that it is able to provide the required flow rate to the device. Downstream of the control valve, air flowed through a volumetric flow meter that is upstream of the nebulizer, enabling the user to tune the desired flow rate using the needle valve. The liquid channel region was isolated from the ambient air during testing, such that a pressure tap could read the vacuum pressure in the liquid channel. A pressure gauge located between the volumetric flow meter and the nebulizer measured the supply static pressure for any given flow rate. The volumetric flow meter used was an Omega Mass Flow meter, with an accuracy of 1.5% full scale. The pressure manometer was a Meriam Instrument digital manometer, with rated maximum of 20in H_2O (~5,000 Pa) and an accuracy of 0.25% full scale. The pressure gauge used was a Fukuda glycerine bath analog gauge with an operating range of 0-60 psi (0-4 bar gauge), and has an accuracy of 1.5% full scale. The temperature of the air was taken from a separate test, where a k-type thermocouple replaced the pressure gauge, and found the air temperature to be 15.2°C \pm 2.2°C.

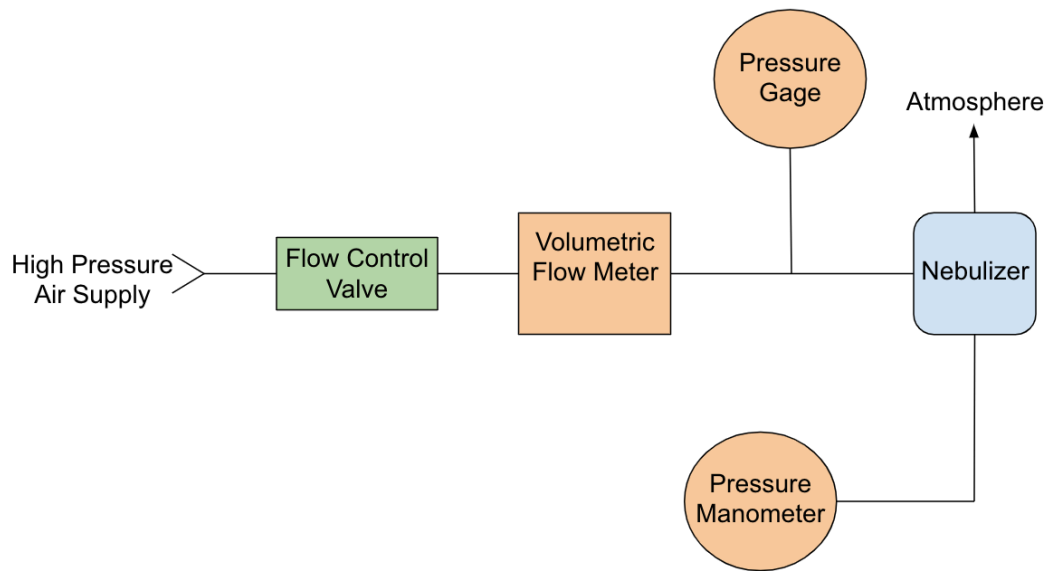


Figure 3.9: Schematic of the Experimental Setup used to Measure the Vacuum Pressure Generated inside the Liquid Channel

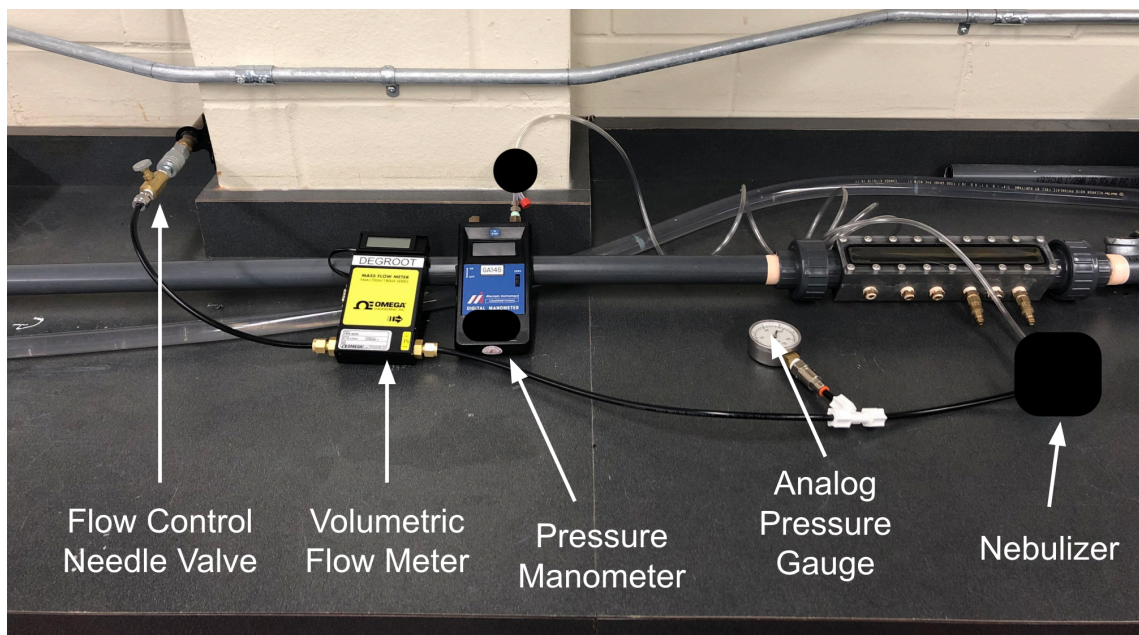


Figure 3.10: Image of the Experimental Setup, Device used is Hidden in the Figure

The region of the nebulizer being numerically modelled is manufactured from two distinct components: the nozzle, and the baffle (Figure 3.1). The radially distant wall of the liquid channel is the same component as the baffle, such that the distance between the top of the proudness and the baffle is fixed for a given part. In the experimental study, three distinct nozzle diameters of 0.432mm, 0.559mm, and 0.686mm were explored. The nozzles were constructed by 3D printing the full geometry and subsequently drilling the orifice, resulting in a 0° draft angle. The nozzle diameters were selected to represent the nominal diameter $\pm 20\%$ as closely as possible with the drill bits available. Two nozzles for each diameter were constructed, such that a total of six nozzles were available for testing. The constructed nozzles were measured by the industry sponsor and the diameter was found to be 0.402mm, 0.414mm, 0.527mm, 0.547mm, 0.659mm, and 0.659mm for devices 1 through 6 respectively. The remainder of the geometric features were built at the nominal dimension. For each nozzle, wall air and compressor air were supplied. A total of eight baffle parts were used for each nozzle, resulting in a total of 96 tests (2 flow rates \times 6 nozzles \times 8 baffles). The average vacuum pressure measured across the eight baffles was reported for each nozzle supplied by wall or compressor air. The geometry was created using the pointwise macro and the mass flow and temperature specified was applied at the inlet boundary. Each numerical geometry was run using both the wall and compressor air supplied condition. The experimental results were compared to the time-average vacuum pressure in the liquid channel to determine the accuracy of the numerical model.

3.1.5 Parametric Study

The purpose of the parametric study was to determine the impact of the proudness, the distance to the baffle, the radius, and the draft angle on the liquid channel vacuum pressure. A low or high value for each parameter was applied in a given case, such that every combination of the parameters was modelled (Table 3.3). Each of the 16 cases tested were identified by a four-character label that used L to indicate the low state, and H to indicate the high state for a given parameter. The characters were listed in the reverse order, DCBA (Table 3.6). For example, in the case where the nozzle diameter (B) and the proudness (D) were in the high state and the other parameters in the low state,

then it would be identified as HLHL. The magnitude of these states for each parameter is applied as follows.

Table 3.3: Parametric Study Parameters and Magnitude of Low and High State

State	Draft Angle (A)	Nozzle Diameter (B)	Distance to Baffle (C)	Proudness (D)
Low	0.5°	0.504mm	1.19mm	0.00mm
High	2.5°	0.616mm	1.59mm	0.25mm
Nominal	1.5°	0.560mm	1.39mm	0.25mm

The magnitude of the proudness was selected as a binary condition. In the low state, the proudness does not exist and it is flush with the nozzle exit, while in the high state the proudness is applied at the nominal designed height of 0.25mm. The low and high value for the distance to the baffle is specified as ± 0.20 mm of the nominal design distance. The nozzle diameter used a low and high value that deviated from the nominal diameter by 10% in either direction. Finally, the draft angle used varied from the nominal angle by 1° in either direction. A draft angle less than 0.5° was not used since this feature is required for manufacturing purposes. Since this parametric study is the first numerical study of its kind on the nebulizer, the variation from the nominal design value is kept small, as the impact they have on the output parameter is not well understood.

To gain as much information as possible a full parametric study was performed, meaning that for the four input parameters of interest, a total of 16 tests (4^2) are required. By doing this, all of the direct influences, two-way, three-way, and four-way interactions that each factor has on the output can be understood, and there is no aliasing of influences. The influence that each factor has over the vacuum pressure is estimated, and fitted to a polynomial curve. For a four-factor parametric study, this curve can be modelled using Eq. 3.1, where each factor A through D and each interaction between factors (such as A interacting with B), is accounted for in the model. Each factor in the model is normalized to range between -1 and +1, such that the low value for each factor is assigned to -1 and the high value is assigned to +1. Any value between the low and high value can be determined by linearly interpolating between the low and high value. The magnitude of each influencing factor was determined for the following study.

$$P_{vac} = P_{int} + I_A A + I_B B + I_C C + I_D D + I_{AB} AB + \dots \\ + I_{BCD} BCD + I_{ABCD} ABCD \quad 3.1$$

3.2 Results

3.2.1 Grid Refinement

Using the macro, each iterative grid refinement step was automated, such that the number of elements used would double for each subsequent case. Given the parameter of interest was the pressure vacuum inside the liquid channel, it was used at the output factor for the mesh independence study. A total of six grid refinement levels were used, ranging from 6,300 cells, to 137,500 cells (Table 3.4). A highly coarse mesh with only 3,700 cells was used to initialize the domain as rapidly as possible, then the results from each coarse mesh was used to initialize the subsequent domain. With each increase in the grid density, a brief initialization period occurred as the flow corrected to the new grid.

The percent change was calculated as: $\% = \frac{(P_{vac,Lvl(n)} - P_{vac,Lvl(n-1)})}{P_{vac,Lvl(n-1)}}$

Table 3.4: Mesh Characteristics for Nebulizer Grid Convergence Study

Refinement Level	Grid Elements	n/d	Wall Element Thickness	Vacuum Pressure (Pa)	Percent Change
Level 1	6,300	8	2.0 μm	1010	-
Level 2	11,300	11	1.4 μm	1574	55.8%
Level 3	20,600	16	1.0 μm	1948	23.8%
Level 4	38,100	23	0.70 μm	2199	12.8%
Level 5	72,300	33	0.50 μm	2189	-0.4%
Level 6	137,500	47	0.35 μm	2231	1.9%

In each case, the liquid channel vacuum was found to follow a low amplitude steady state oscillation that seemed to correlate to a subtle wobble in the position of the toroidal vortex (Figure 3.11). When the mesh was refined from level 4 to level 5, an instability, similar to a KH instability, formed in the flow downstream of the baffle. It caused high-amplitude, high-frequency pressure waves that resembled the acoustic feedback phenomenon that is characteristic of an impinging jet problem (Figure 3.13). As a result, the pressure readings in the liquid channel once the instability formed contained

the high amplitude oscillations along with the low amplitude oscillations found in the less refined cases (Figure 3.12).

Time-averaged pressure readings were taken between 0.6×10^{-3} seconds and 1.0×10^{-3} seconds in order to provide enough time for the flow to initialize to the increased mesh density. When the grid became refined enough to capture the high frequency oscillations, it seemed to have no impact on the time-averaged liquid channel vacuum. Therefore, the magnitude of the liquid channel vacuum was determined to not be impacted by the presence of the instability or the oscillations that accompany them. The absolute value of the vacuum pressure ($P_{vac} = P_{atm} - P_{liquidChannel}$) is reported in Figure 3.14, such that a larger value plotted corresponds to a stronger vacuum. Further, the vacuum pressure generated was considered independent when the level 4 mesh density was reached. All subsequent studies conducted on the nebulizer used a level 4 mesh density.

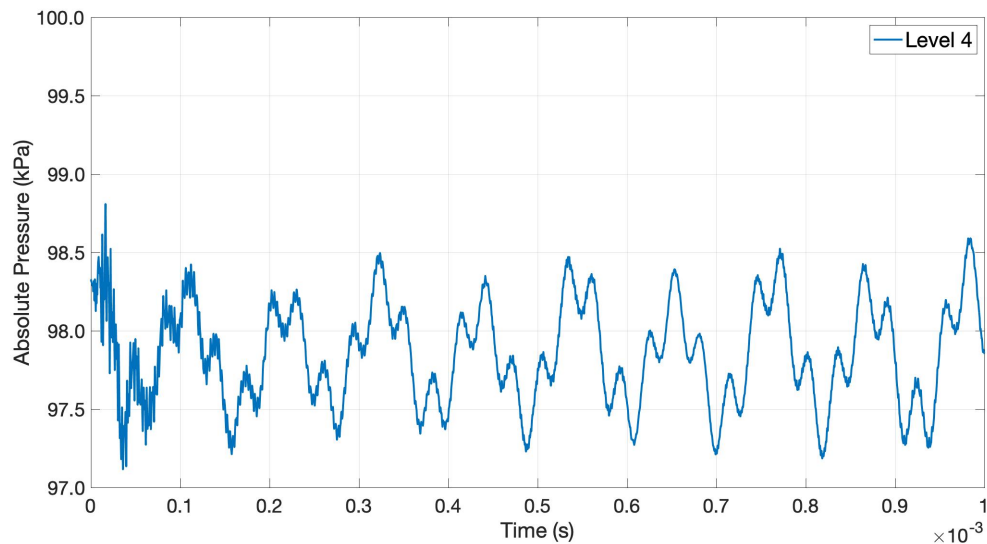


Figure 3.11: Pressure Signal in the Liquid Channel from the Level 4 Grid Density

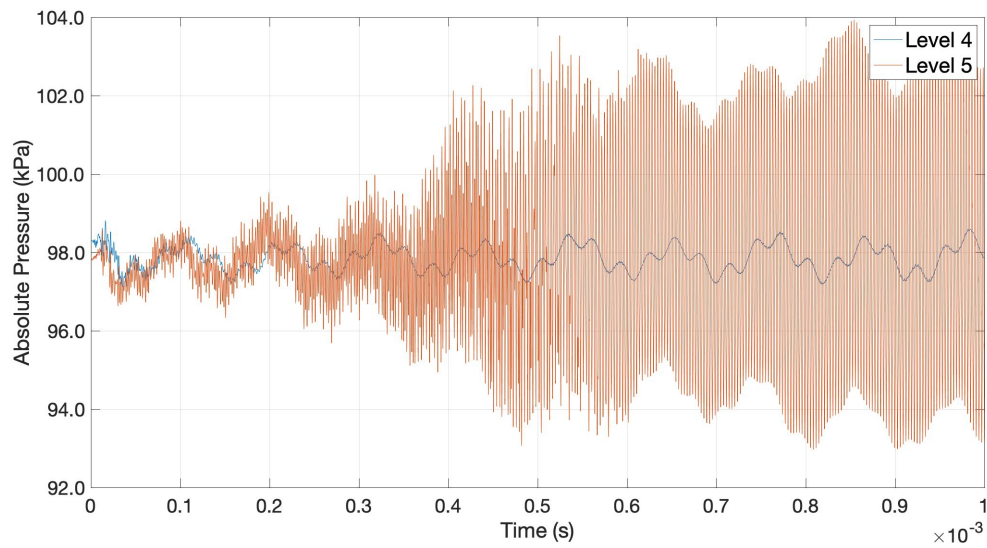


Figure 3.12: Pressure Signal in the Liquid Channel from the Level 4 and Level 5 Grid Density

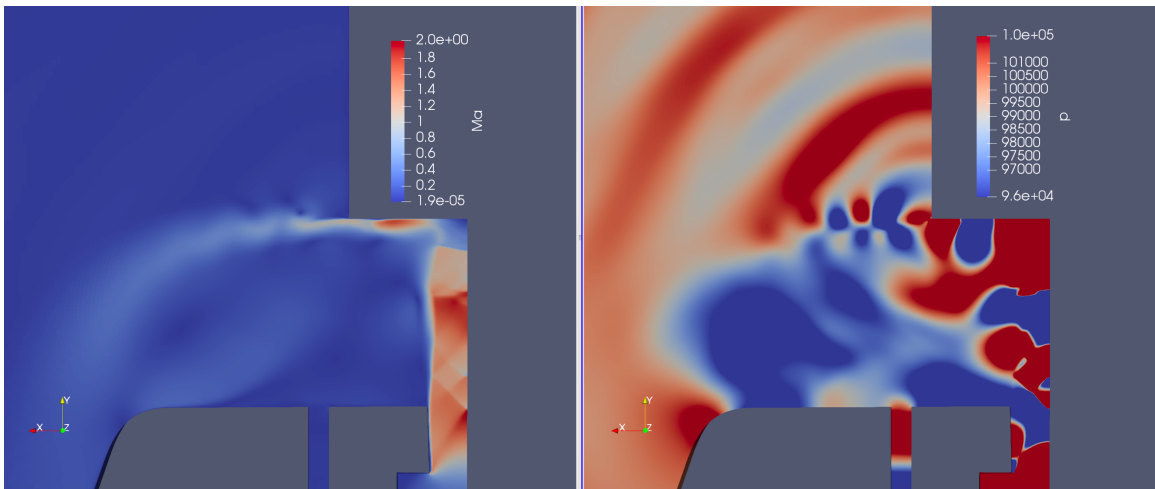


Figure 3.13: KH Style Instabilities found in the Mach Contour Plot (Left) and High Frequency Oscillations Shown in Pressure Contour Plot (Right) for the Level 6 Mesh, Pressure Scaled from 96kPa to 102kPa

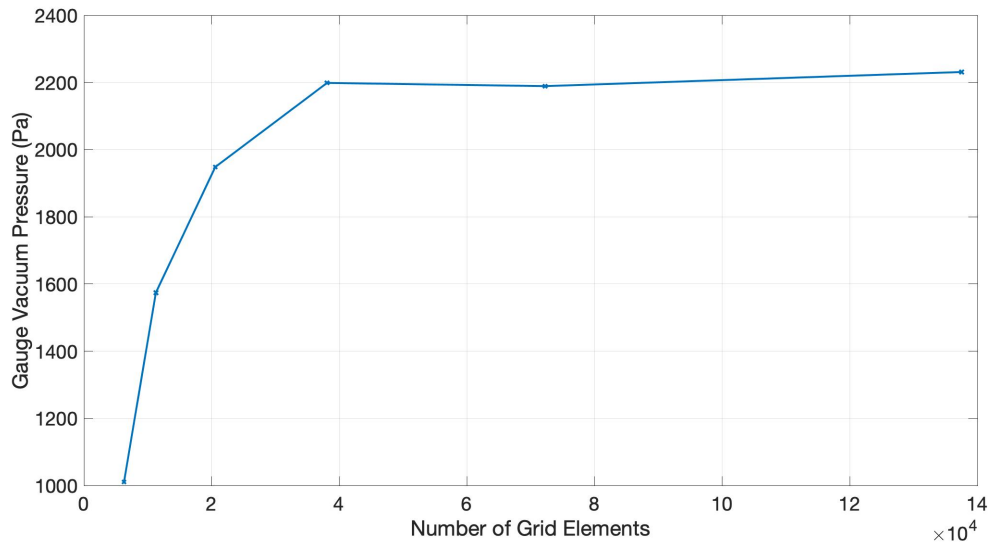


Figure 3.14: Time-Averaged Vacuum Pressure in the Liquid Channel vs. Number of Grid Elements

3.2.2 Experimental Validation

The experimental data from each of the different nozzle diameters was compared to the equivalent numerical case. Similar to the grid independence study, a coarse mesh was used to initialize the domain for each case, then the results of the coarse initialization were mapped to the refined mesh. The transient pressure results inside the liquid channel are shown in Figure 3.15. It can be seen from that plot, that the results for the large diameter nozzle supplied by the compressor contains high frequency, high amplitude oscillations. This implies that the level of grid refinement is not the only factor that influences whether the oscillations are resolved. However, since the previous grid refinement study did not indicate that the presence of oscillations impacted the time-averaged liquid channel pressure, the results are assumed to be valid regardless of their presence.

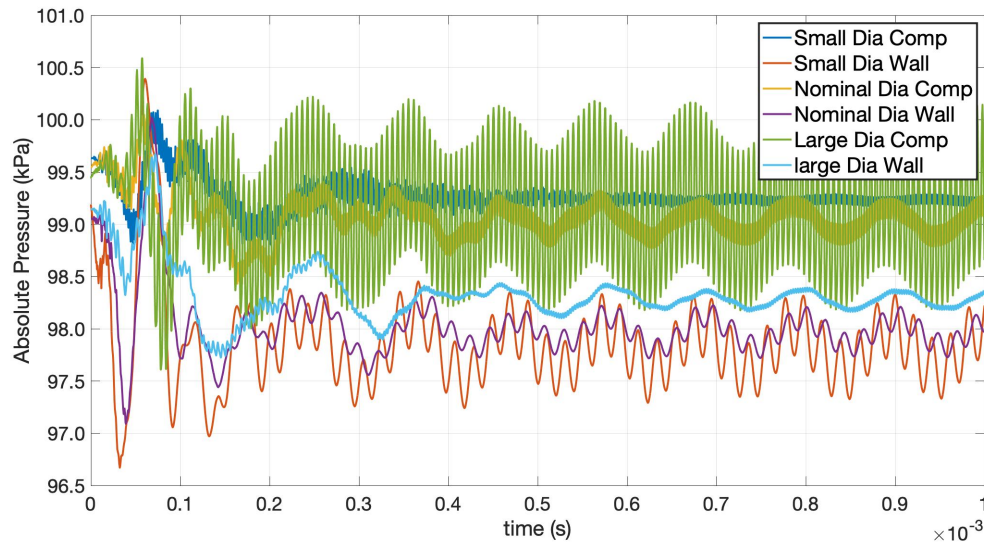


Figure 3.15: Transient Pressure in the Liquid Channel for each Nozzle Diameter Supplied by Wall and Compressor Air

For cases where the device is supplied by compressor air, the mass flow rate applied at the inlet was specified by the nozzle diameter as indicated by the industry partner. Shown in Figure 3.17 as the orange line is the volumetric flow rate vs. nozzle diameter that will be supplied when one of their production compressors is used. The pressure in the nozzle was measured for each experimental case and plotted with the numerical pressure measured at the inlet boundary. As the nozzle diameter increased, the supply pressure required decreased and the mass flow increased, for both the numerical and experimental studies. The supply pressure at the inlet was 6.9-13.8 kPa higher in each numerical case than in the experimental results. The slight offset in the experimental nozzle diameter makes it difficult to determine the exact pressure difference for each case. Thus, the nozzle coefficient of performance can be used to characterize each nozzle. The nozzle coefficient of performance is determined using $C_d = \dot{m}_{actual} / \dot{m}_{ideal}$, where:

$$\dot{m}_{ideal} = A_e C^* \frac{P_0}{\sqrt{RT_0}} [2] \quad 3.2$$

$$\text{where } C^* = \sqrt{\gamma \left(\frac{2}{\gamma+1} \right)^{\frac{\gamma+1}{\gamma-1}}}$$

As shown in Table 3.5, the nozzle coefficient for the numerical cases was consistently lower than the nozzle coefficients for the experimental results. This implies that there are additional losses present in the numerical case that are not in the experimental case. A likely explanation for the lower nozzle coefficient in the numerical study is the sharp corner found at the nozzle inlet. This features causes the *vena contracta* phenomenon, which lowers the effective nozzle diameter (Figure 3.16). Any rounded or tapered edges in the experimental case caused by manufacturing defects would reduce the vena contracta and thereby improve the nozzle coefficient.

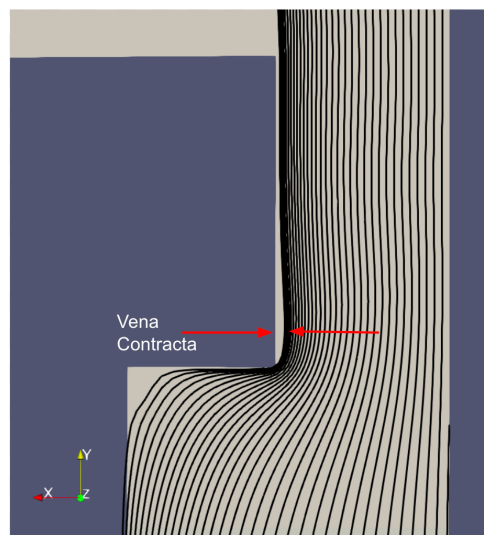


Figure 3.16: Flow Streamlines as the Air Navigates the Sharp Corner Entering the Nozzle, Showing the Vena Contracta Phenomenon

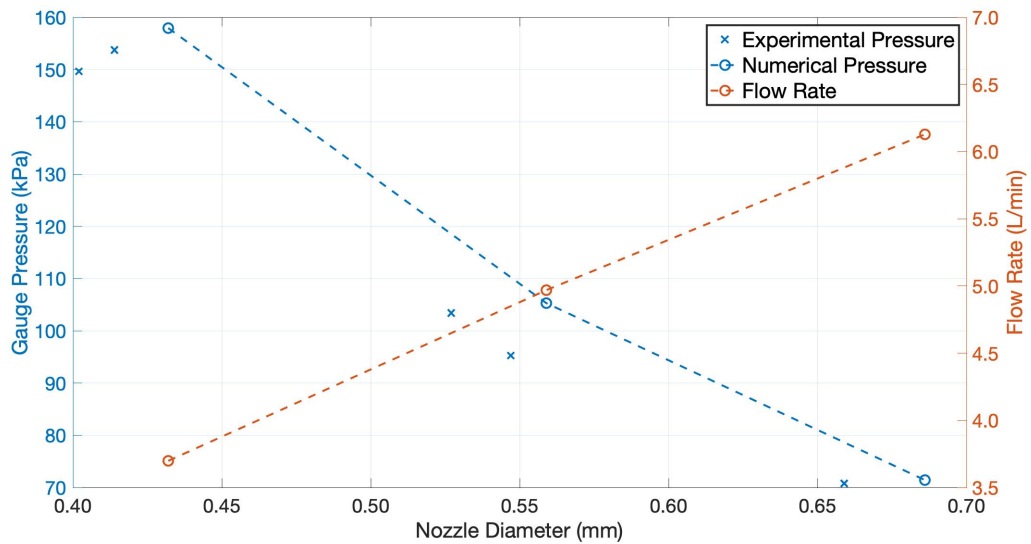


Figure 3.17: Flow Rate vs. Nozzle Diameter for the Compressor Supplier Air, Both Numerical and Experimental Results

For the wall supplied cases, the air flow at the inlet was fixed at 8.0 L/min. Thus, in Figure 3.18, only the supply pressure vs. nozzle diameter is shown. Similar to the compressor supplied cases, the supply pressure in the numerical results are higher than the experimental values. The nozzle coefficients provided in Table 3.5 are similar for both the compressor and wall supplied values, with the largest discrepancy being found in the large diameter studies. The difference here is likely due to the supply pressure provided by the compressor being too low for the nozzle flow to be choked. Thus, Eq. 3.2 is not valid for the largest nozzle diameters supplied by the compressor and shall not be considered. The average nozzle coefficient from the numerical results is 0.848, while the average experimental nozzle coefficient is 0.964. Thus, for a constant nozzle diameter and flow rate, the supply pressure predicted numerically will exceed the experimental results.

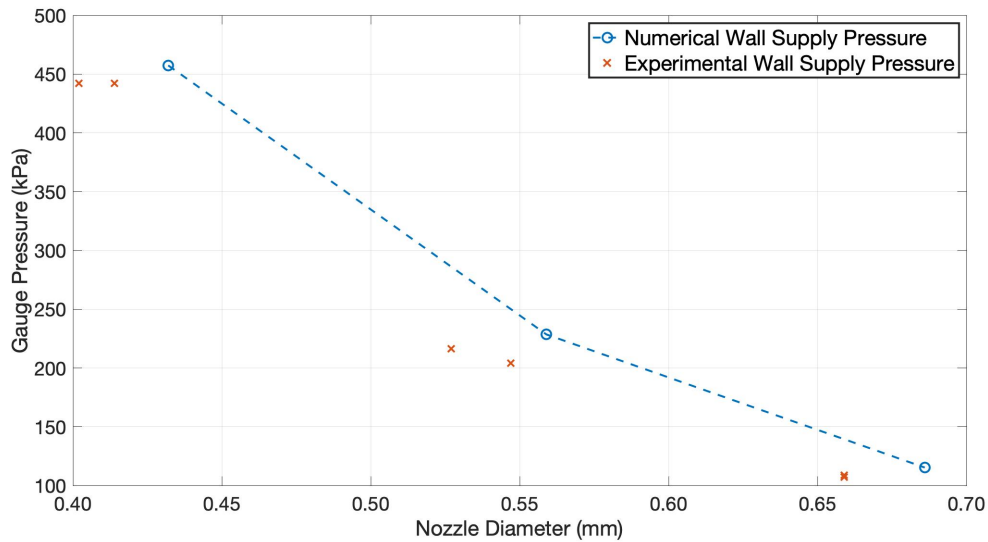


Figure 3.18: Supply Pressure vs. Nozzle Diameter for Wall Supplied Air, Both Numerical and Experimental Results

Table 3.5: Nozzle Coefficient of Performance for Numerical and Experimental Devices

Nozzle	Nozzle Diameter	Compressor NPR	Wall NPR	Compressor C_d	Wall C_d
Numerical 1	0.432mm	2.58	5.57	0.840	0.837
Numerical 2	0.559mm	2.05	3.29	0.846	0.848
Numerical 3	0.686mm	1.72	2.15	0.830	0.859
Experimental 1	0.402mm	2.50	5.42	0.989	0.991
Experimental 2	0.414mm	2.54	5.42	0.925	0.935
Experimental 3	0.527mm	2.03	3.16	0.958	0.988
Experimental 4	0.547mm	1.95	3.04	0.932	0.950
Experimental 5	0.659mm	1.71	2.07	0.899	0.962
Experimental 6	0.659mm	1.71	2.09	0.893	0.956

Measuring the time-averaged vacuum pressure from the numerical results, provides a vacuum pressure that can be compared to the experimental value. The sampling rate of the experimental apparatus is slower than the period of any oscillations, so it is assumed that the experimental measurements are time averaged values. The results are shown in Figure 3.19, where the numerical results are plotted along dashed lines, and the experimental results are placed as individual data points. For the wall supplied vacuum pressure, the numerical results slightly under-predicted the experimental

results. A negative trend in the vacuum pressure as the nozzle diameter increased was captured for both. The compressor-supplied nozzle under-predicted the experimental results more than the wall-supplied results, and most significantly over-predicted the result for the largest diameter nozzle. In the large nozzle diameter case, the experimental vacuum pressure increased, while the numerical vacuum pressure had a small negative trend. It is not known what caused this deviation between the vacuum pressure values, although it indicates that there are additional losses in the numerical cases that are not present in the experimental case. The accuracy of this validation study is enough to provide confidence in the ability for rCF to capture major trends in the nebulizers performance as geometric parameters are changed.

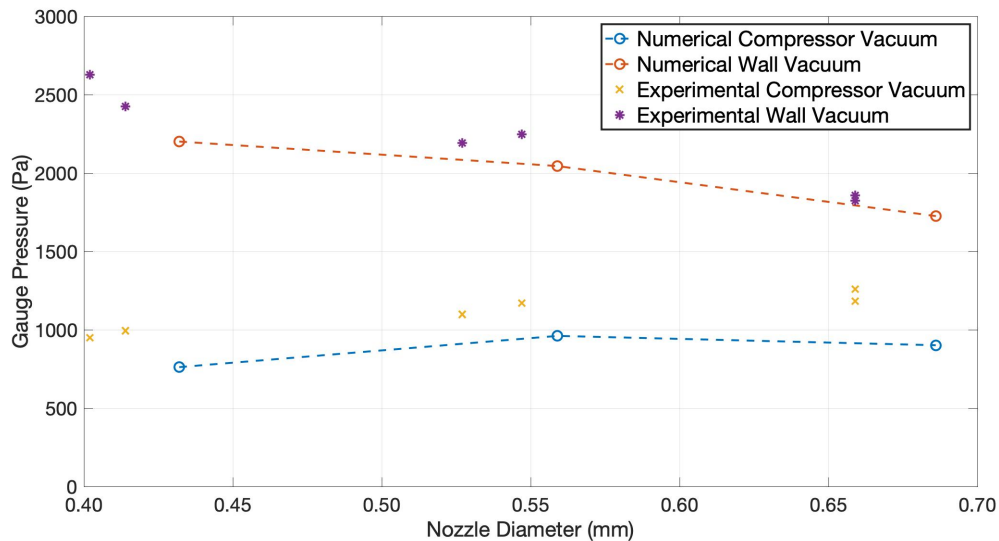


Figure 3.19: Vacuum Pressure Measured in the Liquid Channel for Wall and Compressor Air, Both the Numerical and Experimental Results

3.2.3 Parametric Study

For the full four-factor parametric study, the following cases in Table 3.6 were run. The time-averaged vacuum pressure of each test is shown in Figure 3.20, where the vacuum pressure minimum and maximum values are 1,718Pa and 2,427 Pa respectively. Thus, for the factors tested, supplied by wall air, the vacuum pressure ranges by 709 Pa. The influence of each parameter on the output, and their interactions with each other is

shown in Figure 3.21. These influences and the physical mechanisms driving them will be discussed in more detail in the following section.

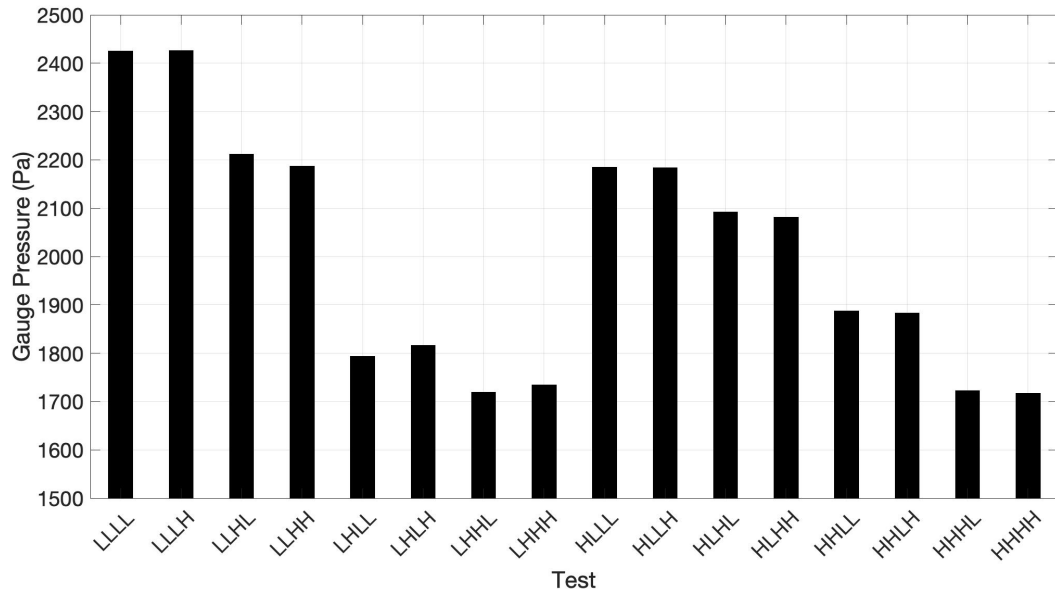


Figure 3.20: Vacuum Pressure Observed in the Liquid Channel for Each Geometry, When Supplied by Wall Air

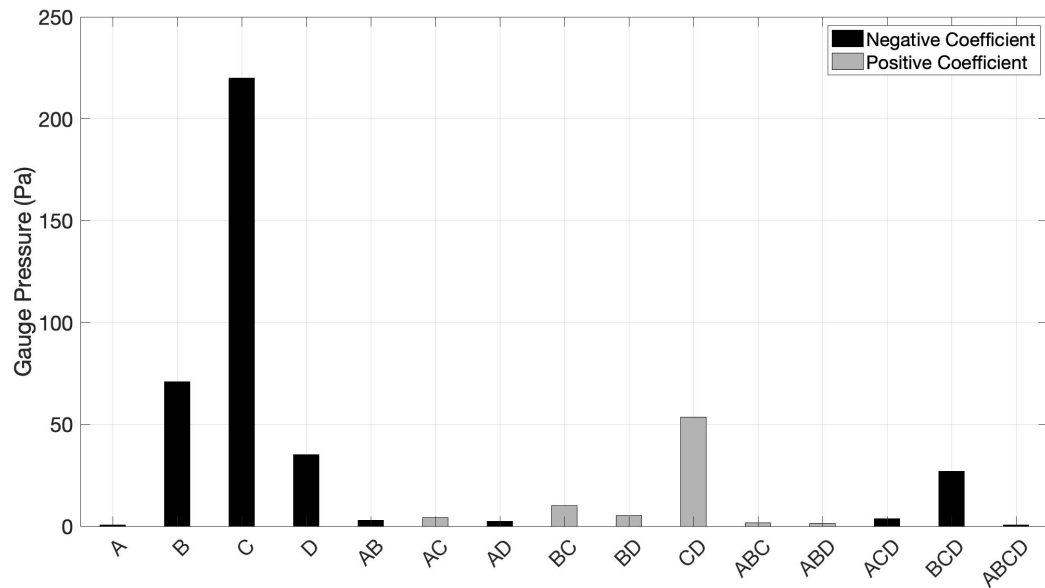


Figure 3.21: Influence and Interaction of Various Parameters on the Liquid Channel Vacuum Pressure

3.2.3.1 Factor A: Nozzle Draft Angle

As the air enters the nozzle and reaches Mach 1 in the throat, a subsequent expansion, based on the draft angle, will accelerate it above Mach 1 as it approaches the nozzle exit. Along with the acceleration beyond Mach 1, the pressure will continue to drop, reducing the pressure difference between the flow at the nozzle exit and ambient conditions. The vacuum pressure in the liquid channel does not seem to be impacted by the draft angle, however, the structure of the free jet is (Figure 3.22). In the low draft angle case, the maximum flow velocity is achieved downstream of the nozzle exit, whereas with the large draft angle, the maximum flow velocity is found inside nozzle (Figure 3.22). As the flow exits the high draft angle nozzle it is below ambient pressure, which is representative of an over-expanded nozzle. Since the choked flow condition is occurring with the same nozzle diameter, the NPR is equivalent in both cases (Table 3.6) and thus the stagnation enthalpy in each jet is not affected by the draft angle. Some differences in the losses would be caused by the different structure of oblique shocks, although these losses are minimal compared to the losses across the impingement shock. U_{Mean} in Figure 3.22, Figure 3.24, Figure 3.26, and Figure 3.28 in the velocity profile in the nozzle averaged over 4.0×10^{-4} seconds.

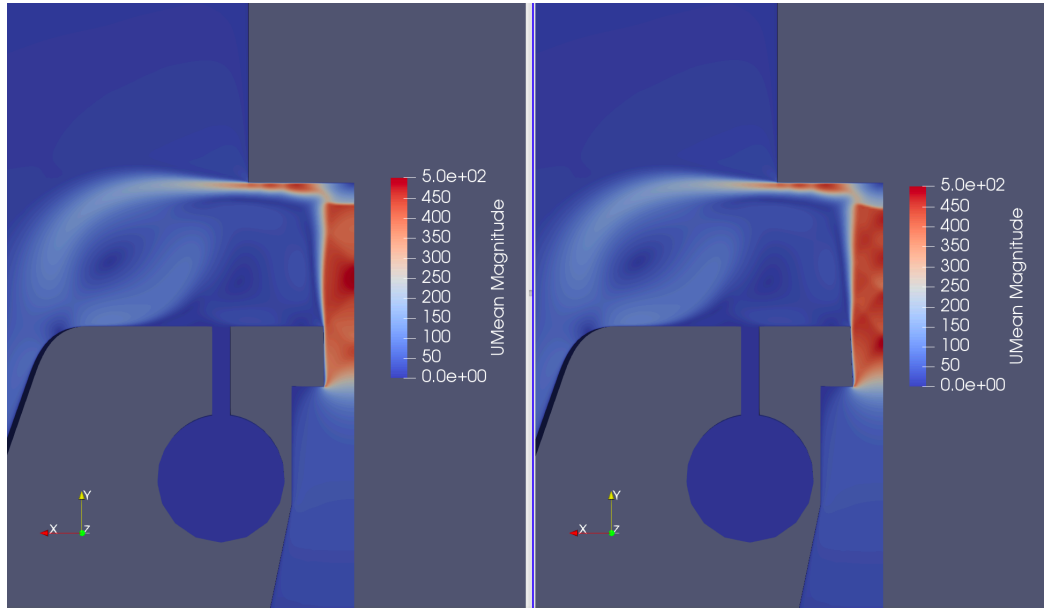


Figure 3.22: Time-Averaged Velocity Contour Plots, Draft Angle in Low State (LLLL - Left) and High State (LLLH - Right)

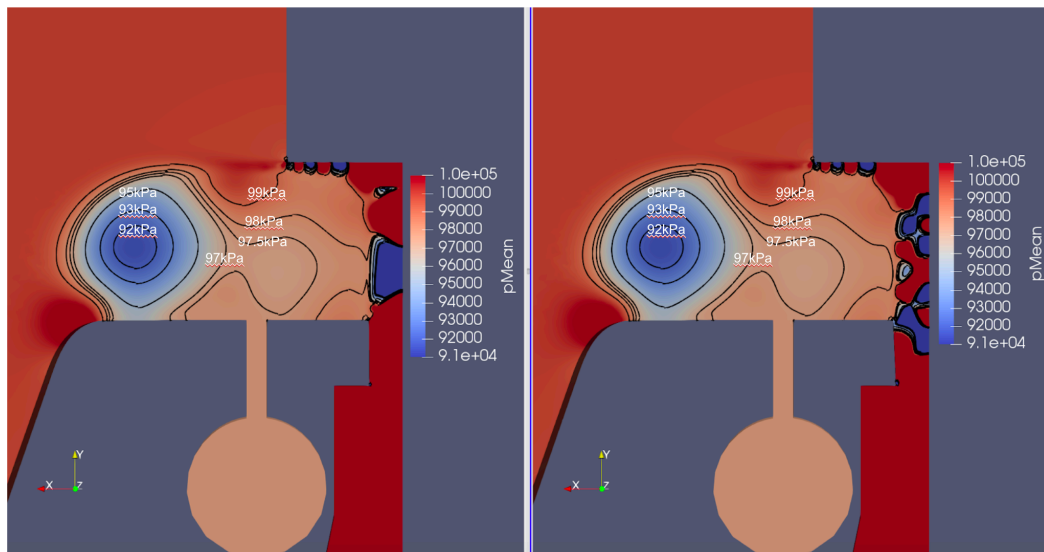


Figure 3.23: Time-Averaged Absolute Pressure Contour Plots, Draft Angle in Low State (LLLL - Left) and High State (LLLH - Right)

3.2.3.2 Factor B: Nozzle Diameter

The nozzle diameter has some influence over the vacuum pressure, with an influence measured at -70.98Pa over the tested range (Figure 3.21). This shows that a smaller nozzle diameter causes a stronger vacuum to be formed in the liquid channel, which is consistent with the negative trend found in the nebulizer validation study (Figure 3.19). The Mach number in the jet core is substantially lower in the large diameter case (LLHL) than in the small diameter case (LLLL). Since the volumetric flow through the nozzle is fixed at 8.0 l/min for wall air, the resistance in the nozzle decreases for an increasing nozzle diameter. Thus, the NPR is lower for a larger nozzle, which lowers the stagnation enthalpy available upstream of the nozzle, and subsequently the flow velocity downstream of the nozzle (Figure 3.24). It is reasonable to expect the lower enthalpy available is the primary factor that influences the impact of this parameter on the vacuum pressure. Further, it is important to note that the supply pressure required is proportional to the nozzle area, which is proportional to the nozzle diameter squared ($A_{nozzle} \propto D_{nozzle}^2$). In the parametric study, the influence of the nozzle diameter is assumed to be linear over the small range tested, which will introduce some error in the final polynomial model.

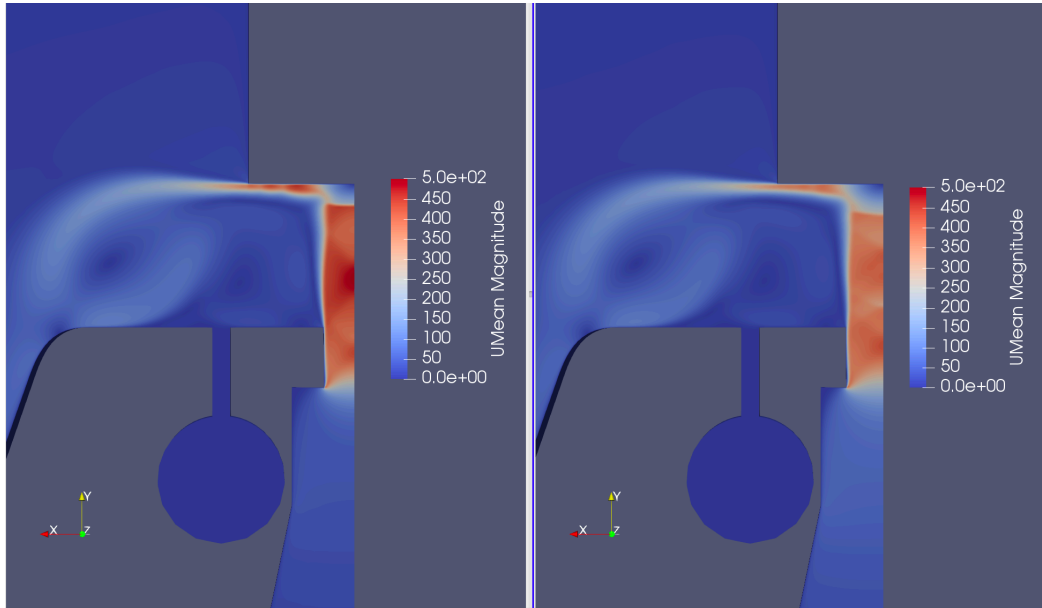


Figure 3.24: Time-Averaged Velocity Contour Plots, Nozzle Diameter in Low State (LLLL - Left) and High State (LLHL - Right)

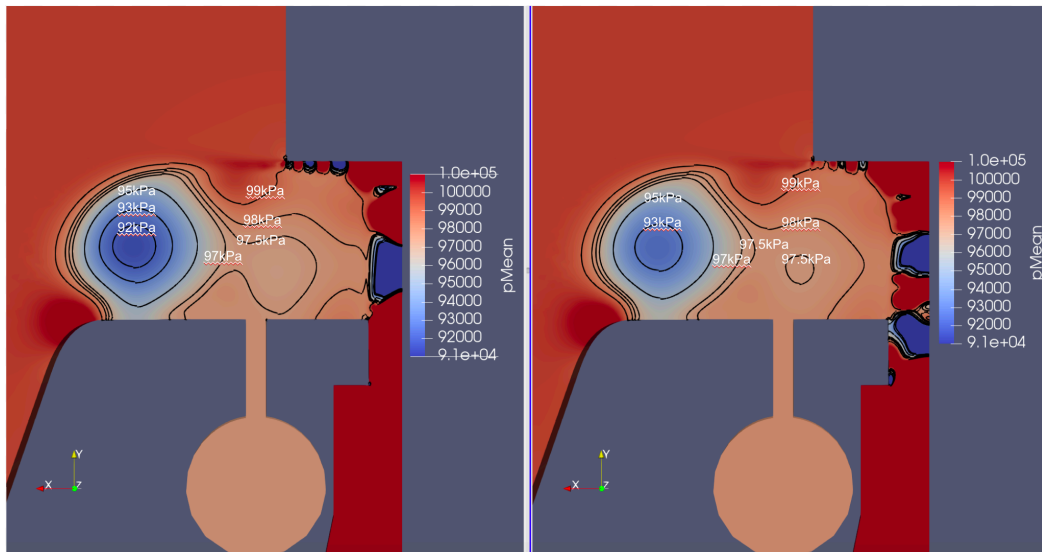


Figure 3.25: Time-Averaged Absolute Pressure Contour Plots, Nozzle Area in Low State (LLLL - Left) and High State (LLHL - Right)

3.2.3.3 Factor C: Distance to the Baffle

The next parameter explored is the distance between the nozzle exit and the impingement baffle. This design parameter seems to have the greatest influence on the vacuum pressure, measured at -219Pa over the explored range, is approximately 3-times greater than the next most influential parameter (Figure 3.21). Figure 3.26 shows how the position of the toroidal vortex appears to be shifted radially outward from the centre axis and subsequently away from the liquid channel. Further, the strength of the vacuum found between the under-expanded jet and the vortex is weakened as the distance to the baffle increases (Figure 3.27). Both the shift in position and weakening of the vacuum match the expected behaviour predicted in the literature [16]–[18]. As the vortex position shifts radially outward, the impingement point of the vortex moves beyond the portion of the proudness that is parallel to the baffle. Thus, the vortex impinges on sloping wall, which appears to stretch the vortex out of a circular geometry (Figure 3.26). The impact of this geometric feature on the liquid channel vacuum pressure is not understood.

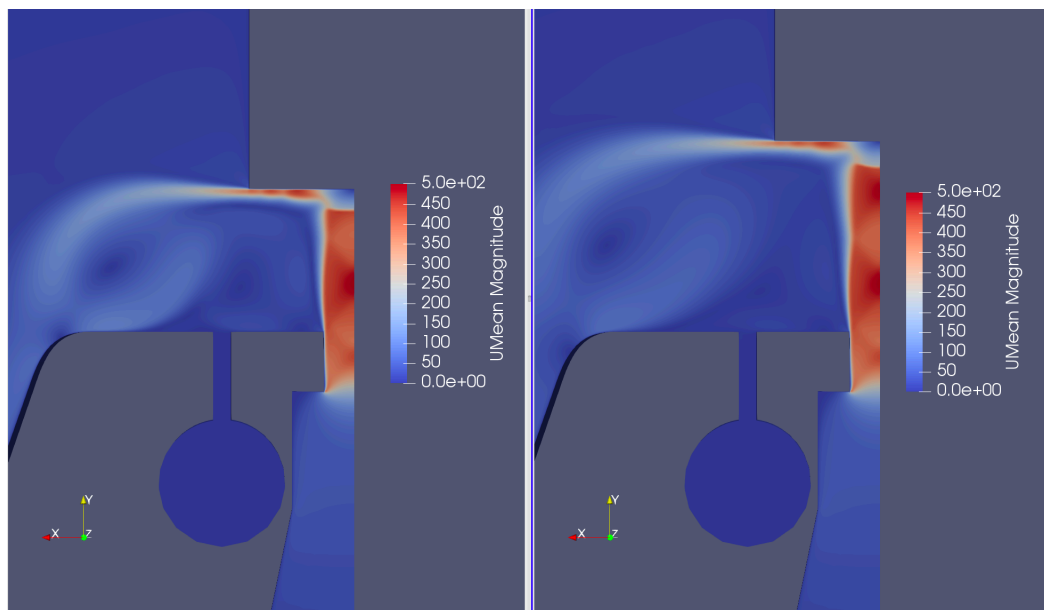


Figure 3.26: Time-Averaged Velocity Contour Plots, Distance to Baffle in Low State (LLLL - Left) and High State (LHLL - Right)

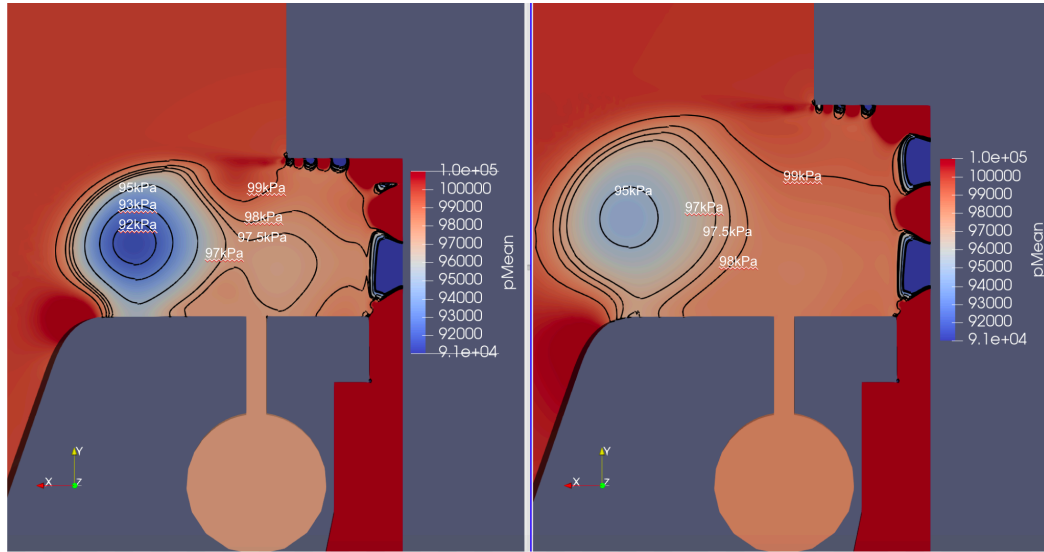


Figure 3.27: Time-Averaged Absolute Pressure Contour Plots, Distance to Baffle in Low State (LLLL - Left) and High State (LHLL - Right)

3.2.3.4 Factor D: Proudness

The final factor explored was the proudness of the liquid channel. As the toroidal vortex is bounded by the baffle and the proudness, the influence of the proudness over the vortex should be similar to decreasing the baffle distance. However, its influence over the vacuum pressure is negative, measured at -35.05Pa (Figure 3.21), indicating that a lower proudness will provide a stronger vacuum pressure. Thus, there must be some competing influences as the vortex is raised away from the liquid channel, that result in a negative influence from the proudness over the range explored.

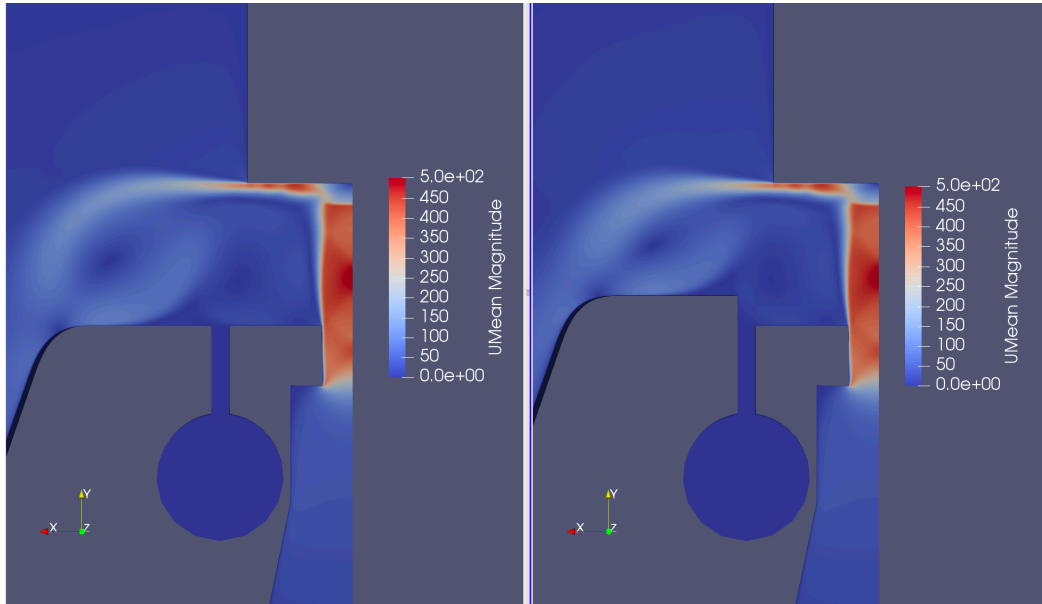


Figure 3.28: Time-Averaged Velocity Contour Plots, Proudness in Low State (LLLL - Left) and High State (HLLL - Right)

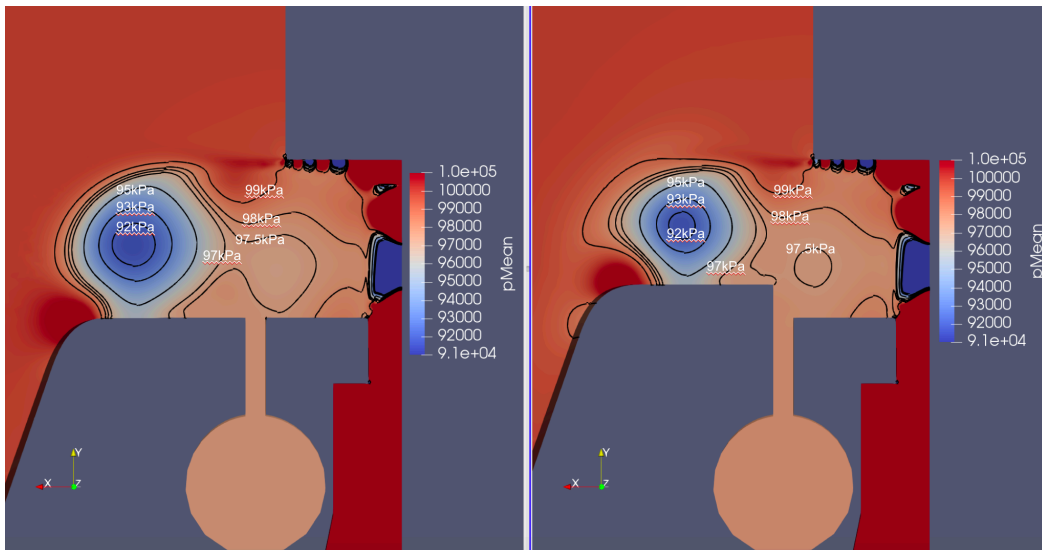


Figure 3.29: Time-Averaged Pressure Contour Plots, Proudness in Low State (LLLL - Left) and High State (HLLL - Right)

3.2.3.5 Interactions

The main interaction between parameters occurred between the distance to the baffle and the proudness. They had a positive coefficient of influence, measured at +53.53Pa, which is more influential than the proudness alone. The three-way interaction between the nozzle diameter, proudness, and distance to the baffle also seemed significant at 26.97Pa, although higher order interactions are more challenging to determine the underlying physical causes. All interactions that included the draft angle were near zero influence, and thus the draft angle likely plays no significant role in the devices performance.

Table 3.6: Parametric Study Cases

Case	NPR	L/d	Vacuum Pressure
1-LLLL	4.07	2.36	2,425 Pa
2-LLLH	4.05	2.36	2,427 Pa
3-LLHL	2.69	1.93	2,212 Pa
4-LLHH	2.68	1.93	2,187 Pa
5-LHLL	4.07	3.15	1,793 Pa
6-LHLH	4.05	3.15	1,817 Pa
7-LHHL	2.69	2.58	1,719 Pa
8-LHHH	2.68	2.58	1,734 Pa
9-HLLL	4.07	2.36	2,185 Pa
10-HLLH	4.05	2.36	2,183 Pa
11-HLHL	2.69	1.93	2,092 Pa
12-HLHH	2.68	1.93	2,081 Pa
13-HHLL	4.07	3.15	1,888 Pa
14-HHLH	4.05	3.15	1,883 Pa
15-HHHL	2.69	2.58	1,723 Pa
16-HHHH	2.68	2.58	1,718 Pa

3.3 Summary

Using the model developed in chapter 2 for modelling the flow of a nebulizer seemed to provide reasonable accuracy when predicting trends in the liquid chamber vacuum pressure. The grid independence study found that at a refined enough resolution, high frequency oscillations appeared in flow. These oscillations seemed to originate when the flow moved downstream of the baffle, causing instabilities that are similar to the KH

style. They appeared to not influence the time averaged pressure vacuum pressure inside the liquid channel, so whether or not they were resolved was determined to not influence the results.

A nebulizer validation study was performed to determine the accuracy of the numerical model for predicting the liquid chamber vacuum pressure. Using an experiment developed in-house, the nebulizer was supplied by both wall air and compressor air, while the supply pressure and liquid chamber vacuum were measured directly. The supply pressure was over-predicted by the numerical model, which is likely due to a lower nozzle coefficient of performance ($C_d = 0.848$, $C_d = 0.964$ for numerical and experiment nozzles respectively). The sharp edge in the sudden contraction found in the numerical model is the primary reason for the low nozzle coefficient, while physical devices may contain defects that help round this feature. The vacuum pressure for each nozzle was accurately predicted for the wall supplied cases, while the compressor supplied cases found a greater under-prediction that was most significant in the large diameter case.

Since the wall supplied air was more accurately predicted, compressor supplied air was omitted from the parametric study. The study concluded that of the four geometric parameters explored, nozzle draft angle, nozzle diameter, nozzle exit to baffle distance, and the liquid channel proudness, only the draft angle did not influence the liquid channel vacuum. The most significant parameter was the distance to the baffle, as it moves the toroidal vortex radially outward from the liquid channel and reduces the vacuum pressure generated. The proudness had an unexpected result, since it was anticipated to have a similar influence as the distance to the baffle by increasing the confinement of the vortex. However, it appears that lifting the vortex away from the nozzle exit has a negative influence over the vacuum pressure generated. The nozzle diameter seems to primarily influence the NPR, since the flow restriction is increased as the nozzle diameter decreases. This phenomenon would not apply when the nozzle is supplied by the compressor, since the flow rate and supply pressure are both functions of the nozzle diameter.

Chapter 4

4 Conclusions and Recommendations

4.1 Conclusions

A lower cost computational model for predicting the behavior of the confined under-expanded impinging jet problem found in a nebulizer device was explored in this thesis. Using an axisymmetric geometry, modelled with rCF from OF and a $k - \omega$ SST turbulence model, the major flow features found in an unconfined under-expanded impinging jet were validated by modelling a simplified geometry with available experimental data. Using these assumptions inherently suppressed any asymmetric flow features and coherent structures in the shear layer. This work found the shock structure within jet, shear layer, length of the super-sonic core, and stagnation properties across the impingement shock were all accurately estimated. The recirculation bubble found behind the impingement shock was likely suppressed by the axisymmetric assumption. The validation work conducted provides a thorough characterization of rCF with the $k - \omega$ SST turbulence model in an axisymmetric domain for under-expanded impinging jets.

Applying the same model to the confined under-expanded impinging jet geometry found in the nebulizer required a new validation study. Experimental results from an in-house study measured the vacuum pressure found in the liquid channel and compared it to equivalent numerically geometry. These results found the nozzle coefficient of performance was higher for the experimental nozzles, indicating the sharp-edged contraction in the numerical nozzle may not be physically representative of the actual geometry. The numerical vacuum pressure was found to have good agreement with the experimental results, where they slightly under-predicted the experimental results. In the mesh refinement study, high frequency pressure oscillations were found to occur at high levels of grid refinement. These oscillations were not found to have any impact on the time averaged vacuum pressure results. The final parametric study aimed to characterize the device based on four geometric parameters when supplied by wall air, the draft angle, nozzle diameter, nozzle to baffle distance, and the liquid channel proudness. The draft

angle appeared to have no impact on the vacuum pressure, although it did influence the shock structure of the under-expanded jet. The nozzle diameter had a negative influence over the vacuum pressure, such that a smaller nozzle increased the strength of the vacuum. This is expected to be caused by the increased NPR and subsequently higher stagnation enthalpy available to the jet in these cases. As suggested from the literature, the nozzle to baffle distance was the most influential parameter on the vacuum pressure. As the distance was increased the position of the vortex moved radially outward and the vacuum pressure was reduced. The proudness appears to have a more complex influence over the vacuum pressure, as it was expected to behave similarly to changing the distance to the baffle. Instead, increasing the proudness (or further confining the vortex) decreased the vacuum pressure measure. Indicating that elevating the vortex above the nozzle plane in the axial direction negatively influences the vacuum pressure. Thus, for wall supplied air a smaller nozzle diameter, shorter distance to the baffle, and low proudness will maximize the vacuum pressure obtained.

4.2 Recommendations

The following recommendations made are broken down in two categories, 1: Future recommendations on modelling the physics of confined impinging jets, and 2: recommendations for improving the prediction accuracy for the nebulizer device,

- 1) Recommendations for modelling flow physics
 - a) Determine what causes the impingement recirculation bubble to be suppressed in the model used for this study. This may be caused by the axisymmetric assumption, the convection scheme or the turbulence model. Each of these factors should be explored to determine which cause the suppression of the feature.
 - b) Study the behaviour of a confined under-expanded impinging free jet. This will study the impact of the NPR as well as the nozzle to plate spacing and the Reynolds number, on the vortex. This flow has not appeared to be explored at the time of writing the thesis.

- 2) Recommendations for improving the nebulizer model
 - a) Experimental flow visualization should be attempted for the nebulizer, to gain direct observations of the under-expanded jet and toroidal vortex in this specific geometry. This may include digital particle image velocimetry (DPIV) or Schlieren imaging.
 - b) Improve the numerical nebulizer geometry by including radii on any sharp edges that may impact the performance of the device. This should attempt to match the radii on manufactured devices, based on quantitative measurements.
 - c) Explore more of the geometric features that are tunable. This may include the radial position of the liquid channel, the diameter and shape of the impingement baffle, or the characteristic or edges where sharp flow separation occurs. This should help fully quantify the device for single phase compressible flow.
 - d) Study the multiphase behaviour of the device by introducing a second liquid phase in the liquid channel. This will require a particle breakup and coalescence model to be included. As of OF version 5, no density based multiphase solvers are available, so a custom solver will need to be developed to capture the liquid phase.

References

- [1] M. Saad, *Compressible Fluid Flow*. Prentice-Hall, 1985.
- [2] E. Franquet, V. Perrier, S. Gibout, and P. Bruel, “Free underexpanded jets in a quiescent medium : A review,” *Prog. Aerosp. Sci.*, vol. 77, pp. 25–53, 2015.
- [3] L. Prandtl, “Über die stationären wellen in einem gasstrahl,” *Phys. Z.*, pp. 599–601, 1904.
- [4] A. Powell, “The sound-producing oscillations of round underexpanded jets impinging on normal plates,” *J. Acoust. Soc. Am.*, vol. 83, no. 2, pp. 515–533, 1988.
- [5] J. L. Weightman, O. Amili, and D. Honnery, “Nozzle external geometry as a boundary condition for the azimuthal mode selection in an impinging underexpanded jet,” *J. Fluid Mech.*, vol. 862, pp. 421–448, 2019.
- [6] C. K. W. Tam and J. Jackson, “A multiple-scales model of the shock-cell structure of Imperfectly Expanded Supersonic Jets,” *J. Fluid Mech.*, vol. 153, pp. 123–149, 1985.
- [7] A. Dauplain, B. Cuenot, and L. Y. M. Gicquel, “Large eddy simulation of stable supersonic jet impinging on flat plate,” *AIAA J.*, vol. 48, no. 10, pp. 2325–2338, 2010.
- [8] B. Zang, V. US, H. D. Lim, X. Wei, and T. H. New, “An assessment of OpenFOAM solver on RANS simulations of round supersonic free jets,” *J. Comput. Sci.*, vol. 28, pp. 18–31, 2018.
- [9] K. A. Phalnikar, R. Kumar, and F. S. Alvi, “Experiments on free and impinging supersonic microjets,” *Exp. Fluids*, vol. 44, no. 5, pp. 819–830, 2008.
- [10] B. Henderson, J. Bridges, and M. Wernet, “An experimental study of the

- oscillatory flow structure of tone-producing supersonic impinging jets,” *J. Fluid Mech.*, vol. 542, pp. 115–137, 2005.
- [11] C. Donaldson and R. S. Snedeker, “A study of free jet impingement. Part 1. Mean properties of free and impinging jets,” *J. Fluid Mech.*, vol. 45, no. 2, pp. 281–319, 1971.
- [12] D. Kim and J. Lee, “Influence of shock structure on heat transfer characteristics in supersonic under-expanded impinging jets,” *Int. J. Therm. Sci.*, vol. 141, pp. 62–71, 2019.
- [13] A. Powell, “On the mechanism of choked jet noise,” *Proc. Phys. Soc. Sect. B*, vol. 66, no. 12, pp. 1039–1056, 1953.
- [14] V. Zapryagaev, N. Kiselev, and D. Gubanov, “Shock-wave structure of supersonic jet flows,” *Aerospace*, vol. 5, no. 2, p. 60, 2018.
- [15] S. I. Kim and S. O. Park, “Oscillatory behavior of supersonic impinging jet flows,” *Shock Waves*, vol. 14, no. 4, pp. 259–272, 2005.
- [16] E. Baydar and Y. Ozmen, “An experimental investigation on flow structures of confined and unconfined impinging air jets,” *Heat Mass Transf.*, vol. 42, no. 4, pp. 338–346, 2006.
- [17] J. Fitzgerald, “A study of the flowfield of a confined and submerged Impinging Jet,” *Int. J. Heat Mass Transf.*, vol. 41, pp. 1025–1034, 1998.
- [18] T. Guo, M. J. Rau, P. P. Vlachos, and S. V. Garimella, “Axisymmetric wall jet development in confined jet impingement,” *Phys. Fluids*, vol. 29, 2017.
- [19] G. K. Morris and S. V. Garimella, “Orifice and impingement flow fields in confined jet impingement,” *J. Electron. Packag. Trans. ASME*, vol. 120, no. 1, pp. 68–72, 1998.
- [20] M. A. Herrada, C. Del Pino, and J. Ortega-Casanova, “Confined swirling jet

- impingement on a flat plate at moderate Reynolds numbers,” *Phys. Fluids*, vol. 21, 2009.
- [21] M. Alam, T. Setoguchi, S. Matsuo, and H. D. Kim, “Nozzle geometry variations on the discharge coefficient,” *Propuls. Power Res.*, vol. 5, no. 1, pp. 22–33, 2016.
- [22] Dharavath M., “View of numerical simulation of supersonic jet impingement on inclined plate,” *Def. Sci. J.*, vol. 63, no. 4, pp. 355–362, 2013.
- [23] A. Hamzehloo and P. G. Aleiferis, “Gas dynamics and flow characteristics of highly turbulent under-expanded hydrogen and methane jets under various nozzle pressure ratios and ambient pressures,” *Int. J. Hydrogen Energy*, vol. 41, no. 15, pp. 6544–6566, 2016.
- [24] A. Rona and X. Zhang, “Time accurate numerical study of turbulent supersonic jets,” *J. Sound Vib.*, vol. 270, no. 1–2, pp. 297–321, 2004.
- [25] V. Vuorinen *et al.*, “Large-eddy simulation of highly underexpanded transient gas jets,” *Phys. Fluids*, vol. 25, 2013.
- [26] V. Vuorinen, A. Wehrfritz, C. Duwig, and B. J. Boersma, “Large-eddy simulation on the effect of injection pressure and density on fuel jet mixing in gas engines,” *Fuel*, vol. 130, pp. 241–250, 2014.
- [27] H. Kim and H. Kasitimura, “Effect of axisymmetric sonic nozzle geometry on characteristics of supersonic air jet,” *J. Therm. Sci.*, vol. 13, 2003.
- [28] B. Zang, U. S. Vevek, and T. H. New, “OpenFOAM based numerical simulation study of an underexpanded supersonic jet,” no. January, pp. 2017–747, 2017.
- [29] A. Hamzehloo and P. G. Aleiferis, “LES and RANS modelling of under-expanded jets with application to gaseous fuel direct injection for advanced propulsion systems,” *Int. J. Heat Fluid Flow*, vol. 76, pp. 309–334, 2019.
- [30] S. M. H. Karimian and G. E. Schneider, “Pressure-based control-volume finite

- element method for flow at all speeds,” *AIAA J.*, vol. 33, no. 9, pp. 1611–1618, 1995.
- [31] Z. J. Chen and A. J. Przekwas, “A coupled pressure-based computational method for incompressible/compressible flows,” *J. Comput. Phys.*, vol. 229, no. 24, pp. 9150–9165, 2010.
- [32] A. E. Kuvshinnikov and A. E. Bondarev, “Comparative study of the accuracy for OpenFOAM solvers,” in *2017 Ivannikov ISPRAS Open Conference (ISPRAS)*, 2017, pp. 132–136.
- [33] A. Kurganov and E. Tadmor, “New high-resolution central schemes for nonlinear conservation laws and convection-diffusion equations,” *J. Comput. Phys.*, vol. 160, no. 1, pp. 241–282, 2000.
- [34] ESI group, “rhoCentralFoam.C,” pp. 1–6, 2019.
- [35] A. Hamzehloo and P. G. Aleiferis, “Large eddy simulation of highly turbulent under-expanded hydrogen and methane jets for gaseous-fuelled internal combustion engines,” *Int. J. Hydrogen Energy*, vol. 39, no. 36, pp. 21275–21296, 2014.
- [36] D. C. Wilcox, *Turbulence Modeling for CFD 3rd Edition*. DCW Industries, 2006.
- [37] D. A. Lysenko, I. S. Ertesvåg, and K. E. Rian, “Modelling of turbulent separated flows using OpenFOAM,” *Comput. Fluids*, vol. 80, pp. 408–422, 2013.
- [38] C. J. Greenshields, H. G. Weller, L. Gasparini, and J. M. Reese, “Implementation of semi-discrete, non-staggered central schemes in a colocated, polyhedral, finite volume framework, for high-speed viscous flow,” *Int. J. Numer. Methods Fluids*, vol. 65, pp. 236–253, 2010.
- [39] M. K. F. R. Menter and R. Langtry, “Ten Years of Industrial Experience with the SST Turbulence Model,” *Heat Mass Transf.*, vol. 576, pp. 60–63, 2003.

- [40] X. Li, K. Wu, W. Yao, and X. Fan, “A comparative study of highly underexpanded nitrogen and hydrogen jets using large eddy simulation,” in *20th AIAA International Space Planes and Hypersonic Systems and Technologies Conference*, 2015, vol. 1.
- [41] S. Chun, S. Fengxian, and X. Xinlin, “Analysis on capabilities of density-based solvers within OpenFOAM to distinguish aerothermal variables in diffusion boundary layer,” *Chinese J. Aeronaut.*, vol. 26, no. 6, pp. 1370–1379, 2013.

Appendices

Appendix A: OF Case Setup for the Nebulizer Model

In OF, the files required to run any case are divided into three folders. 1) system: contains information required for the solver to run such as start and stop time, write intervals, maximum Courant number, numerical schemes, tolerances, etc. The main files held in this folder are *controlDict*, *fvSchemes*, and *fvSolution*. Additional files can be included to provide more capabilities, for this study the *decomposeParDict* was added to enable parallel processing. 2) constant: contains information on the fluid being modelled such as molar mass, Prandtl number, specific heat capacity and viscosity. It also defines the turbulence model that will be used for the case and the mesh information. The main files in the folder are *thermophysicalProperties*, *turbulenceProperties*, and a folder for the mesh files called *polyMesh*. 3) 0: contains all of the boundary and initial conditions of the case being modelled. In the current study, this folder contains *p* (pressure), *T* (temperature), *U* (velocity), *nut* (turbulent viscosity), *alphat* (turbulent thermal diffusion), *k* (turbulent kinetic energy), and *omega* (turbulent dissipation). The contents of each file is available at:

<https://bitbucket.org/pnielsen9/underexpandednozzlercf/src/master/underExpandedCaseSetup/>.

Appendix B: Code used for Nebulizer Mesh Generating Macro

The glyph macro code used to generate the nebulizer mesh geometry was written as a single monolithic file. The file starts by initializing each point that defines the domain of the device, then setting the average cell spacing, and boundary layer spacing for the structured orthogonal region 1. It then runs the algorithm described in chapter 3 to generate region 1, define the number of divisions on each line, set the local refinement of the elements, and finally generate the mesh. Region 2 is then generated, with the boundary layer spacing applied to any line specified as a wall. Walls in the unstructured advancing front orthogonal regions are hardcoded for simplicity. Regions 3-5 are all generated sequentially in the same fashion as region 2. Once each region is generated, the entire domain is extruded into a 5° wedge that can be used by OF. The domain is then rotated back by 2.5° , such that the x-y plane divides the domain in half. The name of each boundary in the domain is then assigned. At this point the macro is complete, providing a fully generated mesh and the required boundaries listed. Each face in the domain must be assigned to the correct boundary listed by the user before the mesh can be exported to the OF polyMesh format. The full code is available at:

<https://bitbucket.org/pnielsen9/structuredquadmeshgenerator/src>

Appendix C: Tabulated Results from the Experimental Validation Study

Table C.1: Experimental Results Tabulated for Compressor Supplied Air, with the 95% Confidence Interval Provided

Nozzle	Nozzle Diameter (mm)	Flow Rate (lpm)	Supply Pressure (kPa)	Vacuum Pressure (Pa)	Confidence Interval (Pa)
1	0.402	3.70	149.6	950.12	± 24.36
2	0.414	3.73	154.3	994.39	± 29.20
3	0.527	5.02	103.3	1098.19	± 21.20
4	0.547	5.05	95.6	1169.26	± 34.68
5	0.659	6.18	70.6	1260.60	± 77.59
6	0.659	6.14	70.6	1183.29	± 32.28

Table C.2: Experimental Results Tabulated for Wall Supplied Air, with the 95% Confidence Interval Provided

Nozzle	Nozzle Diameter (mm)	Flow Rate (lpm)	Supply Pressure (kPa)	Vacuum Pressure (Pa)	Confidence Interval (Pa)
1	0.402	8.05	442.2	2628.12	± 94.76
2	0.414	8.06	434.6	2425.19	± 98.54
3	0.527	8.05	216.4	2193.89	± 38.83
4	0.547	8.02	203.7	2246.88	± 36.91
5	0.659	8.03	107.1	1858.79	± 32.80
6	0.659	8.04	108.8	1823.57	± 48.25

Appendix D: Three-Dimensional Under-Expanded Impinging Jet Study

While the bulk of the research discussed in this thesis was on axisymmetric models, a proof-of-concept three-dimensional study was conducted. The proof-of-concept study utilized rCF and the $k - \omega$ SST turbulence model. Due to the computational cost associated with a three-dimensional model, the size of the domain was limited such that the results will likely be influenced by the inlet and outlet boundary conditions. However, this study was able to resolve a recirculation bubble between the impingement shock and the impingement plate (Figure D.1), implying that the axisymmetric assumption is the likely candidate for the suppression of the recirculation bubble.

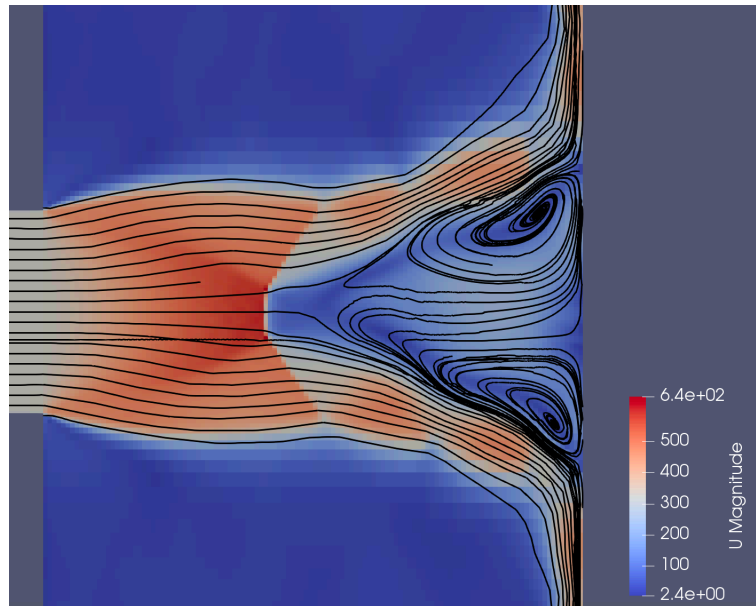


Figure D.1: Velocity Contour Plot with Streamlines, Showing the Recirculation Bubble being Resolved by a Three-Dimensional Model

Curriculum Vitae

Name: Peter Nielsen

Post-secondary Education and Degrees: The University of Western Ontario
London, Ontario, Canada
2012-2017 B.Eng.

The University of Western Ontario
London, Ontario, Canada
2017-2019 M.E.Sc

Honours and Awards: Dean's Honour List 2014,2016

Province of Ontario Graduate Scholarship
2018-2019

Related Work Experience Teaching Assistant
The University of Western Ontario
2017-2018